Graphene Mode-locked and Kerr-lens Mode-locked Operations of Cr^{3+}:LiSAF Lasers Near 850 nm and Tm^{3+}:YLF Lasers Near 2300 nm

by

Ferda Canbaz

A Dissertation Submitted to the
Graduate School of Sciences and Engineering
in Partial Fulfillment of the Requirements for
the Degree of

Doctor of Philosophy

in

Physics

KOÇ
UNIVERSITY

August 15, 2018

Graphene Mode-locked and Kerr-lens Mode-locked Operations of Cr^{3+}:LiSAF Lasers Near 850 nm and Tm^{3+}:YLF Lasers Near 2300 nm

Koç University

Graduate School of Sciences and Engineering

This is to certify that I have examined this copy of a doctoral dissertation by

Ferda Canbaz

and have found that it is complete and satisfactory in all respects,
and that any and all revisions required by the final
examining committee have been made.

Committee Members:

_____
Prof. Dr. Alphan Sennaroğlu (Advisor)

_____
Prof. Dr. Alper Kiraz

_____
Assoc. Prof. Sarper Özharar

_____
Assoc. Prof. Kaan Güven

_____
Assoc. Prof. Ümit Demirbaş

Date: _____

ABSTRACT

Femtosecond lasers operating in the near-infrared and mid-infrared regions can be used in many scientific and technological applications such as pumping of optical parametric oscillators to reach longer wavelengths, electronic/vibrational spectroscopy, and biomedical imaging. This thesis work particularly focuses on Cr^{3+}:LiSAF and Tm^{3+}:YLF lasers, which provide broadly tunable coherent emission near 850 nm and 2.3 μm. The broad tuning range of these lasers further makes it possible to generate femtosecond pulses. In addition, both gain media can be used to construct low-cost lasers by using low-power, widely available diode pump lasers. In recent years, graphene has attracted a great deal of attention as a passive mode locker for the generation of femtosecond pulses, due to its fast and broadband saturable absorption. In the experiments described below, both graphene as well as Kerr-lens mode locking were employed to produce ultrashort pulses with record performance from Cr^{3+}:LiSAF and Tm^{3+}:YLF lasers operating at 850 nm and 2.3 μm.

In the first part of the thesis, we report a femtosecond Cr^{3+}:LiSAF laser, mode locked by using a monolayer graphene saturable absorber (GSA) for the first time. The tight-focusing resonator architecture made it possible to operate the Cr^{3+}:LiSAF laser with only two 135-mW, 660-nm low-cost single-mode diode lasers. At a pump power of 270 mW, the laser produced nearly transform-limited 68-fs pulses at 850 nm with a pulse repetition rate of 135 MHz and an average output power of 11.5 mW. By carefully optimizing the resonator group delay dispersion, we further demonstrated the shortest pulses directly generated to date from a GSA mode-locked laser. In particular, with a pump power of 275 mW, the Cr^{3+}:LiSAF laser produced as short as 19-fs, nearly transform-limited pulses with a repetition rate of 107 MHz and average output power of 8.5 mW. Once mode locking was initiated with the GSA, stable femtosecond pulses could be obtained. In addition, the femtosecond output of the laser could be tuned from 836 nm to 897 nm with pulse durations in the range of 80-190 fs. We further performed detailed mode

locking initiation tests across the full cavity stability range of the laser to verify that pulse generation was indeed initiated by the GSA and not by Kerr lens mode locking.

In the next series of experiments, we developed a new source of mid-infrared femtosecond pulses, based on a Tm^{3+}:YLF laser at 2303 nm. Two different techniques were employed to generate femtosecond pulses with the Tm^{3+}:YLF laser. In the first experiment, an undoped ZnSe substrate was included in the resonator to provide enhanced nonlinear phase modulation during KLM operation. The Tm^{3+}:YLF laser was end-pumped with a continuous-wave Ti^{3+}:sapphire laser at 780 nm. With 880 mW of pump power, the KLM Tm^{3+}:YLF laser generated 514-fs pulses at a pulse repetition rate of 41.5 MHz with an average power of 14.4 mW. In the second experiment, we developed, for the first time to our knowledge, a GSA mode-locked Tm^{3+}:YLF laser operating near 2.3 μm. Since graphene introduces a constant loss of 2.3% per transit, the resonator was extended and double pumped to obtain sufficient intracavity pulse energy. GSA mode-locked Tm^{3+}:YLF laser produced 1-ps pulses at a repetition rate of 17.2 MHz with 42 mW of average output power at 2303 nm.

The major contributions of this thesis work may be summarized as follows. We demonstrated, for the first time to our knowledge, graphene mode-locked operation in a Cr^{3+}:LiSAF laser at 850 nm. We further generated the shortest pulses (19 fs) from a GSA mode-locked solid-state laser. A systematic method was proposed and demonstrated to clearly identify the initiation mechanism of mode locking. Finally, Kerr-lens mode locked and GSA mode locked operations of a mid-infrared Tm^{3+}:YLF laser were demonstrated for the first time. We foresee that the experiments described in this thesis can lead to the development of novel femtosecond laser sources in the near- and mid-infrared regions.

ÖZETÇE

Yakın kızılaltı ve orta kızılaltı bölgelerinde çalışan femtosaniye laserler, daha uzun dalgaboylarına ulaşmak için optik parametrik osilatorlerin pompalanması, elektronik/titreşim spektroskopisi ve biyomedikal görüntüleme gibi birçok bilimsel ve teknolojik uygulamada kullanılabilir. Bu tez çalışması, özellikle 850 nm ve 2.3 μm civarında geniş bir aralıkta ayarlanabilir eş evreli ışıma sağlayan, Cr^{3+}:LiSAF ve Tm^{3+}:YLF laserlerine odaklanmaktadır. Bu laserlerin çıkış dalgaboyunun geniş bir aralıkta ayarlanabilmesi, bu aralıkta femtosaniye darbe üretimini mümkün kılar. Ayrıca, her iki kazanç ortamı da düşük güce sahip ve yaygın bulunabilen diyot laserleri ile pompalanabilmeleri nedeniyle, düşük maliyetli laserlerin kurulumunda kullanılabilir. Son yıllarda, geniş bir aralıkta ve hızlı doyabilen soğurma özelliği nedeniyle, grafen pasif kip-kilitleyici olarak büyük ilgi görmüştür. Aşağıda tarif edilen deneylerde, sırasıyla 850 nm ve 2300 nm civarında çalışan Cr^{3+}:LiSAF ve Tm^{3+}:YLF laserlerinden, hem grafen ile kip-kilitleme hem de Kerr-odaklı kip-kilitleme deneylerinden rekor çalışma performansı ile ultra kısa darbeler elde edilmiştir.

Tezin ilk bölümünde, Cr^{3+}:LiSAF laserinden ilk defa grafen doyabilen soğurucu ile kip-kilitli rejimde çalıştırılması ve bu laserden femtosaniye darbeler üretilmesi anlatılmıştır. Kazanç ortamında iyi odaklanma sağlayan rezonatör tasarımı sayesinde, Cr^{3+}:LiSAF laserinin yalnızca iki adet 135 mW çıkış gücüne sahip ve 660 nm merkez dalgaboyunda çalışan tek-kipli diyotlarla uyarılabilmesi sağlamıştır. 270 mW pompa gücünde, 11.5 mW ortalama çıkış gücüne ve 132 MHz darbe tekrar frekansına sahip dönüşüm limitli 68 fs uzunluğunda darbeler, 850 nm merkez dalgaboyunda üretilmiştir. Rezonatörün içindeki grup gecikme dispersiyonu dikkatli bir şekilde ayarlanarak, grafen doyabilen soğurucu ile bir katıhal laserinden şimdiye kadar elde edilmiş en kısa darbe uzunluğu gösterilmiştir. Bu deneylerde, iki diyotla elde edilen 275 mW giriş gücünde, dönüşüm limitine yakın, 8.5 mW ortalama güce ve 107 MHz darbe tekrar frekansına sahip,

19 fs uzunluğunda darbeler üretilmiştir. Grafen doyabilen soğurucu ile kip-kilitli çalışma başlatıldığında istikrarlı ve kesintisiz femtosaniye darbe üretimi sağlanabilmiştir. Ek olarak, laser femtosaniye darbe üretirken, merkez dalgaboyunun 836 nm'den 897 nm'ye bir prizma yardımıyla sürekli olarak ayarlanabileceği gösterilmiştir. Ayrıca, laserin kararlılık aralığı boyunca yapılan bir test ile, kip-kilitleme rejiminin Kerr-odaklı kip-kilitleme degil grafenden kaynaklandığı deneysel olarak gösterilmiştir.

Bir sonraki deneylerde, merkez dalgaboyu 2303 nm olan ve Kerr-odaklamalı kip-kilitli rejimde (KLM) çalışan bir Tm^{3+}:YLF laseri, yeni bir femtosaniye darbe kaynağı olarak gösterilmiştir. Tm^{3+}:YLF laserinden ultrakısa darbe üretiminde Kerr-odaklı kip-kilitleme ve grafen ile kip-kilitleme olmak üzere iki farklı yöntem kullanılmıştır. İlk deneylerde, katkısız ZnSe alttaşı rezonatöre eklenmiş ve KLM çalışma sırasında doğrusal olmayan faz modülasyonu artırılmıştır. Tm^{3+}:YLF laseri, 780 nm merkez dalgaboyunda sürekli dalga rejiminde çalışan bir Ti^{3+}:safir laseri ile uyarılmıştır. 880 mW giriş gücünde, 14.4 mW ortalama çıkış gücüne ve 41.5 MHz darbe tekrar frekansına sahip, 514 fs uzunluğunda darbeler üretilmiştir. İkinci deneylerde, ilk defa grafen doyabilen soğurucu kullanılarak kip-kilitli rejimde çalıştırılan, merkez dalgaboyu 2.3 μm civarında olan bir Tm^{3+}:YLF laseri geliştirilmiştir. Grafen doyabilen soğurucu bir geçişte %2.3 oranında kayba neden olduğundan, yeterli rezonatör içi darbe enerjisine ulaşmak için, rezonatör boyu uzatılmış ve bir geri yansıtıcı ayna yardımı ile kristal iki tarafından pompalanmıştır. Grafen ile kip-kilitleme rejiminde çalıştırılan ve 42 mW ortalama güce sahip Tm^{3+}:YLF laseri, 1 pikosaniye uzunluğunda darbeleri 17.2 MHz darbe tekrar frekansında üretmistir.

Bu tez çalışmalarının en önemli katkıları şöyle sıralanabilir. 850 nm civarında çalışan bir Cr^{3+}:LiSAF laserinin ilk defa grafen ile kip-kilitli çalıştırılabilecegi gösterilmistir. Ayrıca, bir katıhal laserinden grafen doyabilen soğurucu kullanılarak şimdiye dek üretilmiş en kısa darbeler (19 fs) üretildi. Kip-kilitli rejimi başlatan mekanizmanın ne olduğunu gösteren sistematik bir yöntem önerildi ve deneysel olarak bu

mekanizmanın açık bir şekilde grafen olduğu gösterildi. Son olarak, ilk defa Kerr-odaklı kip-kilitleme ve grafen ile kip-kilitleme yöntemleri kullanılarak, 2.3 μm merkez dalgaboyunda çalışan Tm^{3+}:YLF laserinden ultrakısa darbeler üretildi. Bu tezde anlatılan deneylerin, yakın ve orta kızılaltı bölgelerinde yeni femtosaniye kaynaklar üretilmesinde faydalı bilgiler sağlayacağını öngörmekteyiz.

ACKNOWLEDGMENTS

I would like to thank my advisor Alphan Sennaroğlu for giving me the opportunity to work under his supervision at Laser Research Laboratory (LRL) during my MSc and PhD studies. I appreciate his endless patience, support, and guidance during the last seven years. I always admire his way of solving problems, his passion for research, and desire for teaching. Working with him improved both my technical skills as well as my personality as a researcher. I believe that his precious guidance will help me find my way throughout my academic life.

I would also want to thank Adnan Kurt because of his constant support and guidance during my PhD study. He is always willing to discuss any idea and his valuable comments always show a way out. I feel very lucky to have the opportunity of being friends with him.

I want to thank Ümit Demirbaş for his friendly collaboration and mentorship. I feel really lucky for meeting him and having the opportunity to work with him. I learned several valuable concepts from him during experimental studies. I am indebted to him for his consant support.

I feel lucky to have the chance to work with Sarper Özharar. I appreciate his friendly collaboration and desire for teaching.

I present my appreciation to my thesis committee members Alper Kiraz, Sarper Özharar, Kaan Güven and Ümit Demirbaş for their valuable comments and time.

I am grateful my dear friends Gülce Sarı, Tuğba Nur Öztürk, Dilruba Duygu Söylemez, Gülnihal Kavaklıoğlu, Işınsu Baylam, and Hilal Saraç for their support throughout my PhD study. They constantly listened to me and helped me to find my way. I am also grateful my home-mate Seçil Ünsal for her constant companionship. I also want to thank Yağız and Berna Morova for especially taking care of Mökkoş ☺.

I would like to thank my current and former lab-mates Natali Sözüdoğru, Ersen Beyatlı, Işınsu Baylam, İsmail Yorulmaz, Can Cihan, Abdullah Muti, Yağız Morova, and Gokhan Tanisali. Among all of my lab-mates, Natali Sözüdoğru deserves special thanks because of her help during experiments.

I am also grateful to TUBITAK for providing support for this thesis study under the projects 114F185, 112T967, and 110T810.

Last but not least, I present my deepest appreciation and love to my parents, Semiha and Halil İbrahim Canbaz for their endless support and love throughout my life. I also want to thank my sisters Funda Sevimli and Fulya Toprak who are very important for me. They always supported and guided me throughout my life. I am grateful for their existence. I want to thank my brothers in law Hakan Sevimli and Sinan Toprak for their constant support. I also want to present my deepest love to my niece and nephew Azra Sevimli and Alp Toprak. I am also excited to meet Ilke Toprak who will join our family in the beginning of September.

This thesis is dedicated to my dearest nieces and nephew: Azra Sevimli, Alp Toprak, and Ilke Toprak.

TABLE OF CONTENTS

LIST OF FIGURES AND TABLES

NOMENCLATURE

α:	fine structure constant
A:	area / absorption / element of the ray transformation matrix
$A_{eff.}$:	effective area
c:	speed of light in vacuum
C:	element of the ray transformation matrix
d:	distance
D:	group delay dispersion parameter / element of the ray transformation matrix
$\Delta\nu$:	bandwidth
E:	energy / energy level
E_F:	Fermi energy
E_p:	photon energy / pulse energy
f:	focal length
$f_{rep:}$	repetition rate of the pulses
$g_{0:}$	small-signal differential gain
γ:	Kerr nonlinearity (self-phase modulation) constant
γ_0:	small-signal gain coefficient
$\hbar$:	Planck's constant
I:	light intensity
I_L:	laser intensity
I_p:	pump intensity
I_{sat}:	saturation intensity
J:	fluence
J_{sat}:	saturation fluence
k:	wave vector

k_B: Boltzman constant

K: time-bandwidth product

L: total loss of the resonator / cavity length

l_m: length of the gain medium

M: M-square parameter / mirror

n: refractive index / carrier density

n_0: low intensity refractive index

n_2: nonlinear refractive index

η: slope efficiency

η_a: fractional pump absorption

θ_B: Brewster angle

λ_L: laser wavelength

λ_p: pump wavelength

ν_L laser frequency

ν_p: pump frequency

ν_F: Fermi velocity

ν_{FSR}: free spectral range

q: q-paramater of the beam

P: power

R: reflectivity

σ_a: absorption cross section

σ_e: emission cross section

τ: recombination time

τ_f: fluorescence lifetime

τ_p: pulse width / cavity photon lifetime

T: transmission / temperature

T_R:	cavity round-trip time
ϕ:	phase
ω:	angular frequency
$w(z)$:	spotsize function
w_0:	beam waist
z_0:	Rayleigh range

Chapter 1

1 INTRODUCTION

Chapter 1 presents a general overview of lasers, their potential applications, and provides specific information about the spectroscopic characteristics of Cr^{3+}:LiSAF and Tm^{3+}:YLF gain media. Furthermore, an account of previous studies and a general overview of the optical properties of graphene is provided. In both lasers studied in this thesis, graphene was used as a saturable absorber to obtain ultrashort pulses.

1.1 Motivation

Development of lasers has attracted a great deal of interest for more than 50 years because of their significant applications in science and technology [1-4]. Laser operation can be achieved from gaseous [5], solid [6], and liquid [7] media. Solid-state lasers, in particular, have important advantages such as durability and long operational lifetimes. Pulsed operation of lasers is of interest because it is possible to reach considerably high peak powers with low average output power levels and to perform time-dependent experiments [8]. To date, different techniques have been applied to obtain pulsed operation from solid-state lasers, such as Q-switching [9, 10], active mode locking [11], and passive mode locking [12, 13]. Microsecond (μs), nanosecond (ns), picosecond (ps) and femtosecond (fs) pulses can be generated by using these techniques. Femtosecond pulses, in particular, have been used in the measurement of ultrafast process dynamics [8], material processing [14], biomedical imaging [15-17], metrology [18, 19], military applications [20], and tissue

cutting and welding [21-23]. The most common passive mode-locking methods to achieve femtosecond pulse durations from solid-state lasers can be listed as follows: Kerr-lens mode locking [24], mode locking with semiconductor saturable absorber mirror (SESAMs) [25], and mode locking with nanostructured carbon-based saturable absorber [26-29].

In this thesis, we first focused on femtosecond pulse generation experiments by using graphene as a saturable absorber. Graphene has recently emerged as a fast-saturable absorber. Graphene is a 2-D material with several attractive optical properties: nearly constant saturable absorption over a broad wavelength range [30, 31]. Optical properties, production steps, and characterization methods of graphene saturable absorbers are presented in Part 1.3 in detail. Since it has a relatively easy production procedure compared to other alternative semiconductor based saturable absorbers [25, 32, 33], in recent years, graphene has been utilized to generate ultrashort pulses from solid-state lasers [28, 34-38]. Kerr-lens mode locking (KLM) is the second approach, in this thesis work, to generate femtosecond pulses. To obtain KLM operation from a solid-state laser, critical cavity alignment is required. A qualitative description of Kerr lensing and Kerr-lens mode locking will be presented in Chapter 2.

Near-infrared, tunable, and femtosecond laser sources are particularly important in biomedical imaging applications [15-17]. The most common and known member of this class is the Ti^{3+}:sapphire laser with a tuning range of ~400 nm centered near 800 nm. Cr^{3+}:LiSAF lasers had been developed as an alternative to Ti^{3+}:sapphire lasers due to their wide tuning range (>300 nm) around 850 nm. In addition, Cr^{3+}:LiSAF lasers have an easy pumping architecture. Because of possible applications, this thesis work focuses on Cr^{3+}:LiSAF lasers aiming low-cost femtosecond laser sources. Since the absorption of the Cr^{3+}:LiSAF crystals are near 650 nm, commercially available low-cost laser diodes can be used as pump sources [39]. The first part of this thesis work involved a highly stable, low-cost, and femtosecond Cr^{3+}:LiSAF laser by using graphene saturable absorbers [34, 40].

Femtosecond lasers operating near 2.3 μm can be used in many applications such as pumping of ZGP optical parametric oscillators [41], high harmonic generation in the x-ray region [42], and vibrational spectroscopy [43]. Since one of the absorption bands of the Tm^{3+} ion is around 800 nm, widely available cw Ti^{3+}:sapphire lasers or low-cost 800-nm diodes can be used as pump sources. Tm^{3+}:YLF lasers are of interest due to this relatively simple pumping scheme, attractive applications in the mid infrared, and wide tuning range (2.2-2.46 μm) [44]. The availability of this wide tuning range has the potential to generate pulses as short as 50 fs. This thesis further presents, ultrashort pulse generation experiments based on two different techniques with a Tm^{3+}:YLF laser at 2.3 μm. In particular, femtosecond and picosecond pulses were generated from Kerr-lens mode-locked [45] and graphene mode-locked Tm^{3+}:YLF lasers at 2.3 μm, respectively.

1.2 Cr^{3+}:LiSAF Lasers

Trivalent chromium ion (Cr^{3+}) has been employed in many laser host crystals, such as emerald ($Be_3Al_2(SiO_3)_6$) [46], LiCAF ($LiCaAlF_6$) [47], LiSAF ($LiSrAlF_6$) [48], LiSGaF ($LiSrGaF_6$) [49], and Alexandrite ($BeAl_2O_4$) [50] to investigate laser operation. Cr^{3+} ion mostly resulted in promising lasing characteristics mainly because non-radiative decay processes do not occur in the lowest excited state of the trivalent Cr^{3+} ion. The detailed electronic transitions between energy levels of the trivalent Cr^{3+} ion are shown in Fig. 1-1.

At room temperature, transitions from $^4A_2 \rightarrow {}^4T_2$, $^4A_2 \rightarrow {}^4T_1a$, and $^4A_2 \rightarrow {}^4T_1b$ correspond to the photon energies near 1.90 eV, 2.75 eV, and 4.15 eV, respectively. Typically, Cr^{3+} ions are excited to the $^4T_2$ level by optical pumping (red or blue region of the visible spectrum) and laser transition occurs down to the upper vibrational state of the ground level ($^4A_2$). The photon energy of this laser transition is near 1.46 eV. The 4-level transitions described in the operation of the laser occur as follows: excitation ($^4A_2 \rightarrow {}^4T_2$), relaxation from top of the $^4T_2$ to bottom via ^2E, laser transition ($^4T_2 \rightarrow$vibrational level), and

non-radiative transition (vibrational level→$^4A_2$). This is schematically shown in Fig. 1-1. Because the bottom of the $^4T_2$ state is lower than the ^2E state, these crystals are known as "low-field" hosts for Cr^{3+} [48].

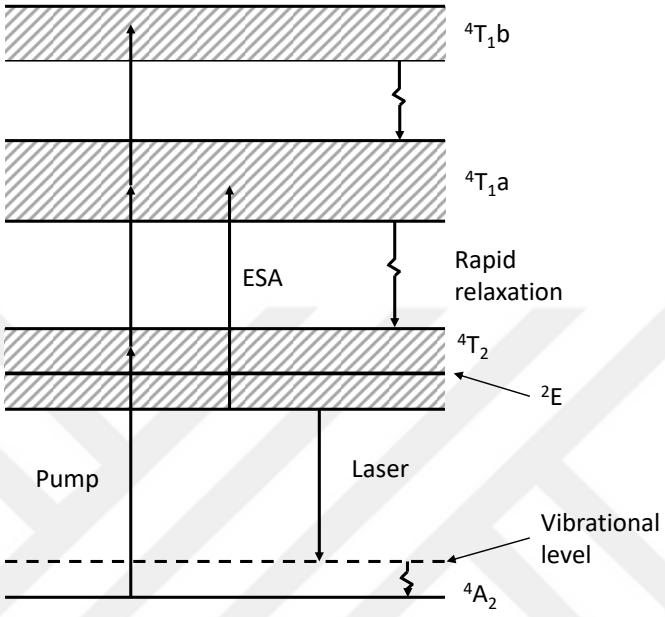

Figure 1-1: The Energy level diagram of a low-field Cr^{3+} ion including optical transitions of the pump, laser, and excited-state absorption [adopted from [51]].

Figure 1-2 shows the measured absorption and emission spectra of a Cr^{3+}:LiSAF medium. The absorption peaks of 650, 450, and 300 nm correspond to the transitions of $^4A_2\rightarrow{}^4T_2$, $^4A_2\rightarrow{}^4T_1a$, and $^4A_2\rightarrow{}^4T_1b$. The features which appear near 650 nm are caused by the ^2E and $^2T_1$ levels which overlap with the $^4T_2$ level [48]. Since Cr^{3+}:LiSAF has no absorption around 520 nm, the crystal looks greenish in color, as shown in Fig. 1-3. The emission spectra shown in Fig. 1-2 correspond to the laser transition from the $^4T_2$ to the $^4A_2$ which is centered near 850 nm [48]. Because of the anisotropy of the crystal structure, absorption and emission spectra are measured slightly different for different polarizations of the electric field as shown in Fig. 1-2.

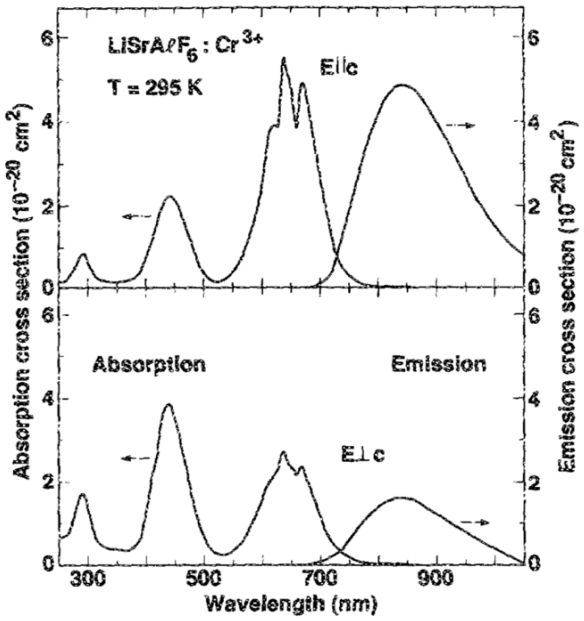

Figure 1-2: Absorption and emission spectra of a Cr^{3+}:LiSAF crystal for the cases of E//c and E⊥c [copied from [48]].

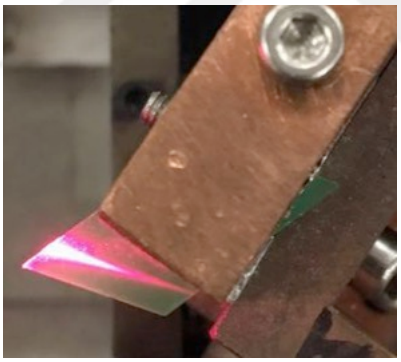

Figure 1-3: The photograph of the Cr^{3+}:LiSAF crystal that we used in our experiments.

Ti^{3+}:sapphire and Cr^{3+}:Colquiriite lasers have long been studied [34, 52-59]. Ti^{3+}:sapphire lasers cover a broad wavelength range from 660 nm to 1100 nm [60]. Cr^{3+}-doped Colquiriite gain media had emerged in late 1980s as an alternative to the Ti^{3+}:sapphire lasers due to their similar operation wavelength [48]. Since Ti^{3+}:sapphire

lasers are widely used to obtain coherent emission around 800 nm, general characteristics of Ti^{3+}:sapphire medium will be discussed. Ti^{3+}:sapphire lasers were further used to generate tunable higher harmonics covering UV [61, 62] and x-ray [63, 64] region with ultrashort pulse widths. Before the invention of green diodes, one major drawback in using Ti^{3+}:sapphire was the pumping scheme, which included the use of frequency-doubled Nd^{3+}-based lasers. These lasers are advantageous due to their beam quality and power however, these systems are bulky and costly. After the development of green diodes, diode-pumped Ti^{3+}:sapphire lasers have attracted a great deal of interest to become compact, stable, and portable cw and pulsed laser sources especially for the biomedical applications [65, 66]. Due to lower value of the product of emission cross-section and lifetime ($\sigma_e \tau = 131$ μs cm^2), Ti^{3+}:sapphire lasers have higher laser thresholds pump powers. This is because, in a 4-level laser system, the threshold pump power for lasing varies inversely as the cross-section lifetime product according to [67]

$$P_{th} = \frac{\pi h \upsilon \left(w_L^2 + w_P^2 \right) \left(L + T \right)}{4 \eta_a \sigma_e \tau_f} . \tag{1.2.1}$$

Above h is the Planck's constant, w_L and w_P are laser and pump beam spotsize, L and T are the loss and transmission of the output coupler of the laser resonator, and η_a is the small-signal absorption of the gain medium. High operation thresholds limit the output power of the diode pumped Ti^{3+}:sapphire lasers.

Furthermore, to obtain stable laser operation at high pumping levels, one important factor is the thermal stability, which is related to the thermal conductivity and the thermos-optic properties(dn/dt) of the medium. In the case of Ti^{3+}:sapphire, thermal conductivity is quite high (28W/K.m), which makes it possible to obtain high-power operation from Ti^{3+}:sapphire lasers [68, 69].

In this thesis, we mainly focus on femtosecond pulse generation experiments from the Cr^{3+}:LiSAF lasers operating near 850 nm. A comparison between Cr^{3+}:LiSAF gain medium and other Colquiriite gain media and Ti^{3+}:sapphire is given in Table 1-1. As can be seen from Table 1-1, Cr^{3+}:LiSAF has many favorable characteristics. As mentioned before, the operation wavelength and tuning bandwidth of the Cr^{3+}:LiSAF lasers (λ_c=850 nm, 780-1110 nm [70]) nearly overlap with Ti^{3+}:sapphire lasers (λ_c=808 nm, 660-1180 nm [71]). The tuning range of the Cr^{3+}:LiSAF laser is possibly limited by the absorption at the shorter edge and excited state absorption at long wavelengths [72]. As an alternative to Ti^{3+}:sapphire lasers, Cr^{3+}:LiSAF lasers have attracted a great deal of interest because their absorption band overlaps with the low-cost, low-power red diodes (used in DVD drivers) are widely available [70, 73]. Since the threshold for laser operation for Cr^{3+}:LiSAF is lower than that for Ti^{3+}:sapphire, due to the higher emission cross section and lifetime product (Table 1-1) [70]. Compared to other Colquiriites (Cr^{3+}:LiCAF and Cr^{3+}:LiSGaF), Cr^{3+}:LiSAF has the highest value of $\sigma_{em}\tau_f$. Hence, even with low pumping powers, Cr^{3+}:LiSAF can provide sufficient output power. Additionally, the quantum efficiency of the Cr^{3+}:LiSAF gain medium (λ_p/λ_L =78%) is higher than that for the Ti^{3+}:sapphire (67%), resulting in higher power slope efficiencies. In particular of a 4-level laser is given by the formula

$$\eta = \eta_a \frac{\lambda_p}{\lambda_L} \frac{T}{T+L} \quad . \tag{1.2.2}$$

Above, η is the slope efficiency, η_a is the absorption at the pump wavelength, λ_p and λ_L are the pump and laser wavelengths, T is the transmission of the output coupler, and L is the loss of the resonator.

One disadvantage of the Cr^{3+}:LiSAF gain medium is the fact that, it is more challenging to obtain Kerr-lens mode-locked operation due to its low nonlinear refractive index (Table 1-1).

Table 1-1: A detailed comparison of Cr^{3+}:LiSAF, Cr^{3+}:LiCAF, Cr^{3+}:LiSGaF and Ti^{3+}:sapphire.

Gain medium	Cr^{3+}:LiSAF	Cr^{3+}:LiCAF	Cr^{3+}:LiSGaF	Ti^{3+}:sapphire
Tuning range (nm)	782-1042 [74]	754-871 [74]	777-977 [74]	660-1180 [75]
Demonstrated shortest pulse width (τ_p)	10 [53]	9 [76]	14 [77]	~5 [71]
Nonlinear refractive index (n_2) [$\times 10^{-16}$ cm^2/W]	0.8 [78]	0.4 [78]	1.2 [78]	3.2 [78]
Peak emission-cross section (σ_{em}) [$\times 10^{-20}$ cm^2]	4.8 [79]	1.3 [79]	3.3 [80]	41 [79]
Room-temperature fluorescence lifetime (τ_f) [μs]	67 [79]	175 [79]	88 [80]	3.2 [79]
$\sigma_{em}\tau_f$ [μs$\times 10^{-20}$ cm^2]	322 [79]	228 [79]	290 [79]	131 [79]
Thermal conductivity [W/K.m]	3.1 [68]	5.1 [68]	3.6 [78]	28 [68]
Intrinsic slope efficiecncy [%]	54 [74]	69 [74]	60 [74]	64 [81]

To obtain efficient and stable laser operation from a Cr^{3+}:LiSAF laser, thermal and mechanical properties of the gain medium must be considered [82-86]. In Cr^{3+}:LiSAF lasers, as in all colquiriites, four processes could be responsible for thermal loading in the crystal: 1) quantum defect, 2) thermal quenching of the upper laser level, 3) excited state absorption, and 4) Auger upconversion. The quantum defect has a contribution in thermal loading due to nonradiative transitions inside crystals. Since the quantum efficiency of Cr^{3+}:LiSAF lasers is high (λ_p / λ_L=0.78) the quantum defect is not the main mechanism behind thermal loading in the Cr^{3+}:LiSAF lasers. The other mechanism is thermal quenching of the upper laser level [82]. Beyond a critical temperature ($T_{1/2}$), at which the upper state lifetime decreases to its half-value of the radiative lifetime, thermal quenching starts to decrease the upper-state population via non-radiative decay processes. As a result, when the temperature of the crystal increases, the gain of the crystal decreases. Since the critical temperature of LiSAF ($T_{1/2}$=69°C) is the lowest among colquiriites, it creates a barrier to power scaling of the Cr^{3+}:LiSAF laser. The third process is excited state absorption (ESA), where an electron in the excited state is transferred to an upper level by pump absorption. This process is nearly negligible in Colquiriites [87]. The relaxation is generally non-radiative which generates heat in the crystal. The last thermal loading mechanism is Auger upconversion [87, 88]. In Auger upconversion, excited ions at the state of $^4T_2$ interact with each other leading to nonradiative energy transitions and generation of additional heat in the lattice.

To date, Cr^{3+}:LiSAF lasers have long been studied due to their lower scattering losses, higher emission cross-section and lifetime product, and broader tunability compared to other members of Colquiriites. The first laser operation was demonstrated by Payne et al. in 1989 [48]. After three years, Scheps et al. showed that efficient laser operation could be obtained by using a diode pump source [39]. Mode-locked operation of Cr^{3+}:LiSAF lasers

was demonstrated in 1992 by Miller et al. [89], generating 150-fs pulses using the Kerr-lens mode-locking technique. To obtain Kerr-lens mode locking from a Cr^{3+}:LiSAF laser, Miller et al. used an acousto-optic mode locker to initiate and sustain pulsed operation [89]. First ultrashort pulse demonstration without acousto optic initiation based on Kerr-lens mode-locking was obtained by Evans et al. in 1993 [90], producing 50-fs pulses. Again in 1993, multi-mode diodes were used as pump sources and picosecond pulses were generated by Balembois and French et al. [90-92]. By using a 15-W diode array, Kopf et al. demonstrated 1.42 W cw and 500 mW of mode locked output power from a Cr^{3+}:LiSAF laser [54]. In 1997, low-cost, low-power, and narrow-stripe diodes were used as pump sources by Valentine et al. [93], leading to the development of compact, battery-powered, and efficient Cr^{3+}:LiSAF lasers [74, 94-99]. Later, again using multi-mode diode pumping scheme, as-short-as 10-fs (12-fs) pulses were generated from a Cr^{3+}:LiSAF laser in 2000 (in 1999) [53, 100]. In 2001, pulses at GHz repetition frequencies were demonstrated by Kempf et al. for the first time [101]. After the development of single-mode, low-power, and battery-powered diodes which are generally used in DVD writing technology, ultrabroad femtosecond tuning range of 105 nm was demonstrated by using a semiconductor saturable absorber mirror (SESAM) [102]. Later, >100 nJ of energy could be extracted from a diode-pumped Cr^{3+}:LiSAF laser cavity by using cavity dumping technique [103, 104]. In 2014 and 2015, to investigate Kerr-lens mode-locking characteristics with a gain matched output coupler (GMOC) technology in Cr^{3+}:LiSAF lasers, which matches the gain and loss profile inside the resonator so as to produce ultrabroad bandwidths, a GMOC was used to initiate and sustain Kerr-lens mode locking operation with 13-fs and 14.5-fs pulses by our group [105, 106].

In this thesis work, we employed a monolayer graphene as a saturable absorber to generate ultrashort pulses from a diode-pumped Cr^{3+}:LiSAF laser. Low-cost and low-power red-diodes were used as pump sources in the mode locking experiments. We first set

up a compact and low-threshold laser resonator including a graphene saturable absorber. We generated 68-fs pulses with 11.5 mW of output power at 850 nm [34]. We then included a pair of prisms to fine tune the group delay dispersion inside the resonator. This led to the generation to obtain pulses that ever generated by using graphene as a saturable absorber. With the graphene saturable absorber, we generated 19-fs pulses from the diode-pumped Cr^{3+}:LiSAF laser with an average output power of 8.5 mW. We further performed femtosecond tuning experiments by inserting an adjustable slit. Finally, we performed a detailed mode locking initiation test across the full stability range of the laser to verify that mode locking was indeed started by the graphene saturable absorber and not by Kerr lens mode locking [40].

1.3 Tm^{3+} Lasers

Radiative laser transitions of trivalent thulium ion (Tm^{3+}) doped gain crystals ($Y_3Al_5O_{12}$ [107, 108], $YAlO_3$ [108, 109], $YLiF_4$ [110, 111], $LuLiF_4$ [112], YSGG [107], Y_2O_3 [113], Sc_2O_3 [113], BaY_2O_3 [114]) are centered near 2 μm and 2.3 μm. In addition, laser operation near 2 μm can be obtained from Tm^{3+} doped ceramic [115] and glass [116] hosts. Another laser operation wavelength of the Tm^{3+} ion was recently demonstrated from a cryogenically cooled Tm^{3+}:YLF laser around 800 nm [117].

One important favorable characteristic of the Tm^{3+}-doped gain media is that it is possible to obtain femtosecond pulses [118-120]. The electronic configuration of a Tm^{3+} ion is given as

$$Tm^{3+}: [Xe]\ 4f^{12}.$$

Here [Xe] shows the electronic configuration of the inert xenon atom:

$$[Xe]: 1s^2\ 2s^2\ 2p^6\ 3s^2\ 3p^6\ 3d^{10}\ 4s^2\ 4p^6\ 4d^{10}\ 5s^2\ 5p^6.$$

The electronic configuration of the Tm^{3+} ion ends with 4f shell, which is shielded by 5s and 5p shells. Due to this shielding effect, the operation wavelength of a Tm^{3+}-doped gain medium is nearly independent of the host crystal. The last shell (4f) of the Tm^{3+} ion which includes 12 electrons is not fully filled. The 4f shell corresponds to F (L=3) orbitals with orbital angular quantum numbers of l=0,1,2,3. For the F orbitals, the corresponding magnetic quantum numbers will be between $-3 < m_l < 3$. At each principal quantum number (n), the corresponding orbital angular quantum numbers are in the range of $0 \le l \le n-1$. The corresponding magnetic quantum numbers ($-l \le m_l \le l$) result in degenerate angular momentum states with the same energy. Additionally, the spin projection quantum number ($-s \le m_s \le s, m_s = \pm\frac{1}{2}$ for electron spin) has two possibilities. As a result of this degeneracy in the angular momentum, the Tm^{3+}-doped gain media have the tuning capability due to transitions between different angular momentum states. Hence, femtosecond pulse generation can be achieved with broad spectral bandwidths.

The energy level diagram of the Tm^{3+} ion is shown in Fig. 1-4. The Tm^{3+} ions can be pumped near 800 nm, 1200 nm, or 1600 nm (in-band pumping) to obtain 2 μm oscillation (Fig. 1-4). The most common operation wavelength of the Tm^{3+} ion is 2 μm. In the case of in-band pumping [Fig. 1-4 (a)], the quantum efficiency (λ_p / λ_L) is nearly ~90%. Another efficient pumping wavelength is 1200 nm (λ_p / λ_L=~60%) to obtain 2 μm lasing [Fig. 1-4 (b)]. Near the pumping wavelength of 800 nm, ions are excited to the $^3H_4$ state. At this pumping wavelength, it is possible to obtain either 2 μm ($^3F_4 \rightarrow {}^3H_6$) or 2.3 μm laser oscillation [Fig. 1-4 (c)]. In the case of 2 μm transition, since the energy difference of the $^3H_4 \rightarrow {}^3F_4$ transition nearly matches the energy of the $^3F_4 \rightarrow {}^3H_6$ transition, an energy transfer occurs between the excited and ground state electrons of two neighbor ions at high Tm^{3+} ion concentrations. This process is known as cross-relaxation (CR) which increases

the quantum efficiency (~40%) by up to a factor of 2. Lasers operating near 2 µm, in particular, can be used in the following applications: tissue cutting [121] and welding [122, 123], remote sensing [124], and laser radar (LIDAR) [125]. Both ESA and UC can be observed in Tm^{3+} ions at high pump intensities as shown in Fig. 1-4. These processes do not depend on the doping concentration.

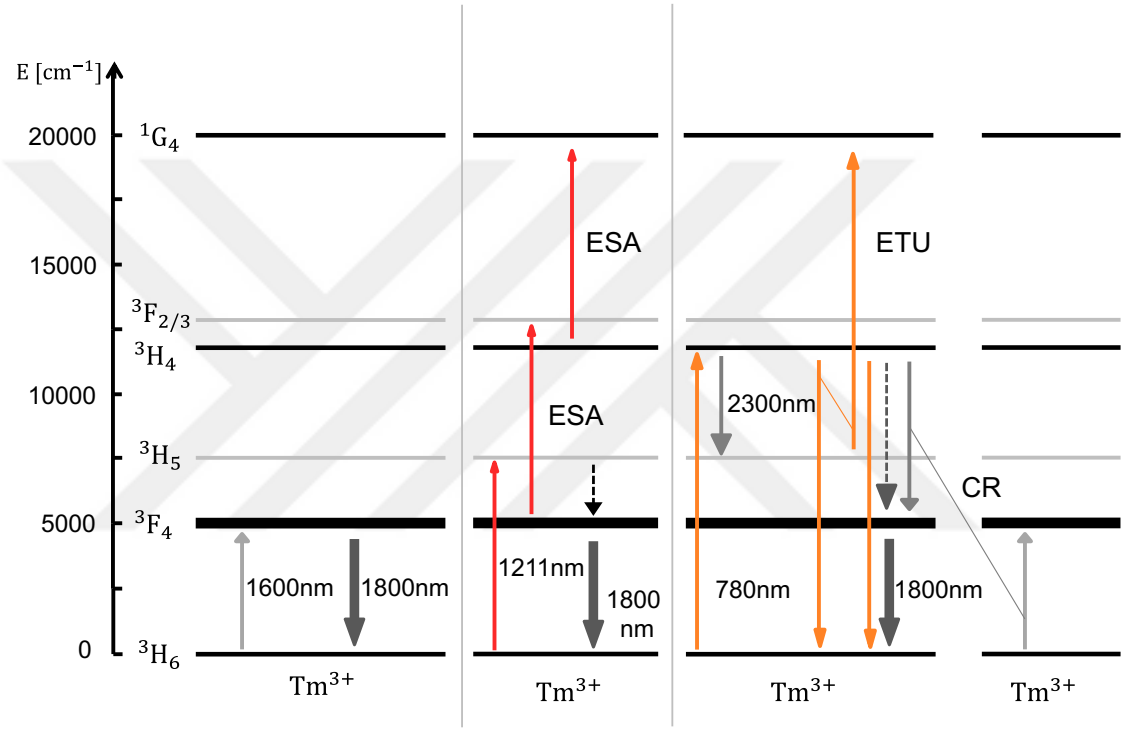

Figure 1-4: The energy level diagram of a trivalent thulium ion, including cross-relaxation (CR), excited state absorption (ESA), and energy transfer upconversion processes (ETU) [Adopted from [126]].

The following parts of this thesis focus on the 2.3 µm transition of the Tm^{3+} ion. To obtain 2.3 µm transition ($^3H_4 \rightarrow {}^3H_5$), ions need to be excited up to $^3H_4$ state. As shown in Fig. 1-4, this is possible by optical pumping near 800 nm. The laser transition ($^3H_4 \rightarrow {}^3H_5$) occurs from the first excited state. The following transitions ($^3H_5 \rightarrow {}^3F_4$, $^3F_4 \rightarrow {}^3H_6$) have no contribution to the laser output. As is mentioned before, the high value of the cross-section-

lifetime product needs to have a low value to otain low threshold lasing. To obtain population inversion at the excited state, it is important to have longer upper-state lifetime. In YLF host crystals and similar fluoride hosts, due to lower multi-phonon relaxation rates, upper-state lifetimes ($^3H_4$) are longer than that from oxide hosts (930 μs in YLF and 340 μs in YAG) [111]. Another important reason of shortening the upper-state lifetime is the doping concentration level. In the literature, the optimum doping level of Tm^{3+} ions for 2.3 μm lasing was determined to be near 1.5 at.%, to eliminate concentration quenching effects [108].

Since 1972, 2.3 μm transition of the Tm^{3+} ion has been studied with different resonator schemes and in different operating regimes. The first laser operation at 2.35 μm was obtained from a Tm^{3+} and Cr^{3+} codoped gain medium by Hobrock and DeShazer [127]. This was the first demonstration of a 4-level laser transition from a gain medium codoped with Tm^{3+} and Cr^{3+} ions, where Cr^{3+} ion is responsible for pump absorption. Pulsed output was obtained from the Tm^{3+} and Cr^{3+} codoped gain medium by using a flaslamp pump source. In 1975, Caird et al. [128] demonstrated laser operation at 2.3 μm from Tm^{3+}:Cr^{3+}:YAG and Tm^{3+}:Cr^{3+}:$YAlO_3$ gain media. In addition to solid-state lasers, 2.3 μm operation was demonstrated from a flash-lamp pumped Tm^{3+} doped-fluorozirconate fiber in 1988 [129]. After a while, in 1994, a wide tuning range was demonstrated by Pinto et al. from a cw Tm^{3+}:YLF laser operating near 2.3 μm [44]. Later, diode pumped and cw operation of Yb^{3+} and Tm^{3+} codoped YLF laser was demonstrated by Diening et al. [130] and De Matos et al. [131]. As can be seen from the list of previous studies to date, either gain-switched or cw operation of the Tm^{3+} doped gain media was demonstrated. Our group later demonstrated the first passively-Q-switched operation of a Tm^{3+}:YLF laser at 2.3 μm [132]. The first mode-locked operation of a Tm^{3+}:YLF laser operating near 2.3 μm was demonstrated with picosecond pulse durations in 2017 [133]. Our group also investigated the l ow-threshold cw operation of a diode-pumped Tm^{3+}:YLF laser [134].

In this thesis work, we first focused on femtosecond pulse generation from a Kerr-lens mode-locked Tm^{3+}:YLF laser operating near 2.3 μm. We increased the intracavity nonlinearities by inserting a pollycrystalline ZnSe substrate. A YAG substrate was also included to balance the nonlinearities with negative dispersion. After a critical alignment procedure, ultrashort pulses with 500-fs pulse width were generated from the Kerr-lens mode locked Tm^{3+}:YLF laser. We later employed a graphene saturable absorber to generate stable and uninterrupted ultrashort pulses from the Tm^{3+}:YLF laser operating near 2.3 μm. Since the inclusion of graphene decreased the output power of the laser mainly due to unsaturable losses of the sample, we extended the laser resonator with a mirror arrangement to increase the intracavity pulse energy with the available pump power. We achieved 1-ps pulses from the graphene mode-locked Tm^{3+}:YLF laser near 2.3 μm.

1.4 Graphene as a Saturable Absorber

Graphene is the first stable 2-D material discovered in 2004 [135]. Geim and Novoselov experimentally isolated graphene with a novel and simple technique from graphite [135] and won 2010 Nobel Prize in Physics. Graphene has been used in many applications [31, 40, 136-140] due to its superior electrical, optical, thermal, and mechanical properties [30, 135, 141-143]. Typically high-quality samples are need to obtain the best performance of graphene [135].

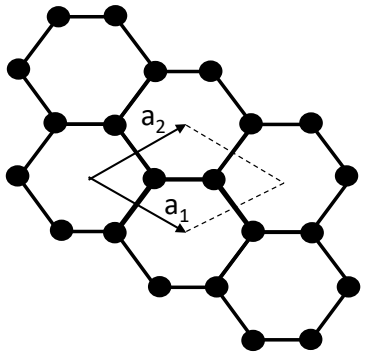

Figure 1-5: Hexagonal honey-comb lattice structure of a monolayer graphene. Lattice vectors a_1 and a_2 are also shown.

Graphene consists of carbon atoms with a hexagonal honey-comb lattice structure as shown in Fig. 1-5 [31]. A unit cell of graphene is described by two lattice vectors ($\vec{a_1}$ and $\vec{a_2}$ as shown in Fig. 1-5) and contains two atoms. A monolayer graphene behaves as a semiconductor. Since the band diagram has contact points at each corner of a hexagonal structure, graphene has gapless band structure. Most of the important properties of a monolayer graphene such as high electrical conductivity, nearly wavelength independent absorption, and high thermal conductivity stem from the unusual energy band diagram which is shown in Fig. 1-6 [30]. The Fermi level of a monolayer graphene at 0 K lies at the Dirac point where charge carriers behave as massless and obey a linear dispersion relation of the form

$$E = h\upsilon_F \vec{k} \ , \tag{1.4.1}$$

where, h is the Planck's constant, υ_F is the Fermi velocity (1.1×10^6 m/s) and $\vec{k}$ is the wavevector.

As was stated above, graphene has various applications. This thesis work mainly focuses on the applications in the field of ultrafast optics [34, 35, 40, 136, 144-148]. In the following paragraphs, optical properties, optical characterization techniques, and production details of a monolayer graphene will be discussed.

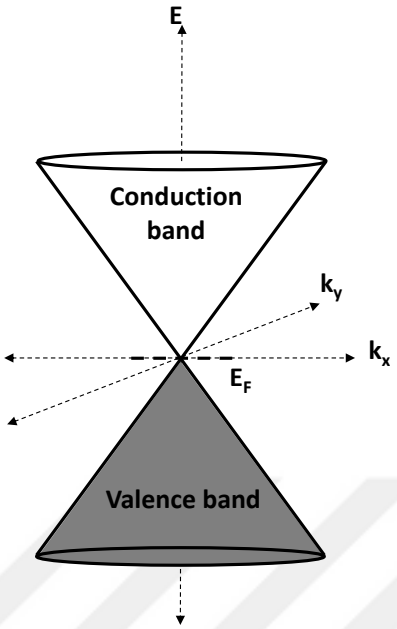

Figure 1-6: The gapless band structure of a monolayer graphene. The Fermi level lies on the Dirac point which is the contact point of valence and conduction bands.

The monolayer graphene has nearly constant absorption of 2.3% as a function of wavelength due to its zero-bandgap structure, meaning that transition from the valence band to the conduction band is possible at each wavelength. The single pass absorption (A) of graphene can be expressed in terms of the fine structure constant ($\alpha = e^2 / \hbar c \approx 1/137$) as

$$A = 1 - T \approx \pi\alpha = 2.3\% \ . \qquad (1.4.2)$$

Absorption of graphene is directly related with the number of graphene layers [142, 149]. Since even a monolayer of graphene has an absorption of 2.3%, it is possible to recognize a monolayer graphene transferred to a substrate by naked eye (Fig. 1-7).

Therefore, one of the important characterization methods is the use of spectrophotometers. Spectrophotometers measure the absorption or transmission of a material by measuring the difference between incident and transmitted light. The intensity of the light source is low and hence, small-signal absorption of a sample can be measured.

Figure 1-8 shows the experimentally measured transmission of the graphene on infrasil sample that we used in our mode locking experiments conducted with Cr^{3+}:LiSAF.

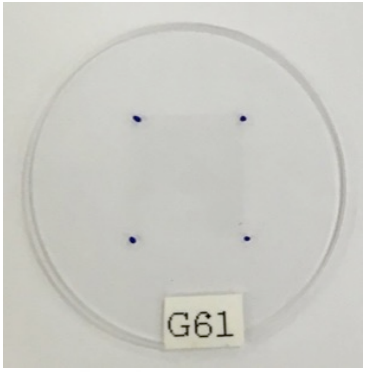

Figure 1-7: Photograph of the atomic thick graphene layer placed onto an infrasil substrate. This sample was produced by our collaborators at Korea Advanced Institute of Science and Technology in Korea and used in mode locking experiments with the Tm^{3+}:YLF laser.

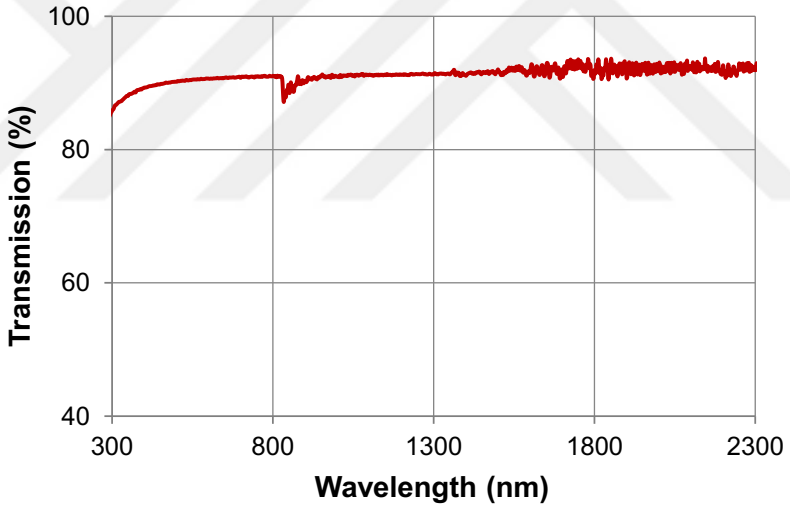

Figure 1-8: The optical transmission of the monolayer graphene on infrasil substrate which was produced by our collaborators at Bilkent University.

One of the important characterization methods investigates the Raman spectrum of graphene [150, 151]. The Raman spectrum can be related to the structural properties of graphene sample in a non-destructive way. Four characteristic Raman bands (designated as

G, G`, D, and 2D) of graphene are normally seen in the Raman spectrum. As has been shown in previous studies [150-152], relative intensities and widths of the Raman bands give information about the number of layers as well as the quality of the graphene sheet. The G band centered around 1580 cm^{-1} is one of the dominant features in the Raman spectrum [151], denoting the symmetry-allowed graphite band. The D band further related with the defect characteristics of the graphene sheet. In particular, the D band is centered around 1350 cm^{-1} and the intensity ratio of D and G bands should be in the range of $0.05< I_D / I_G <0.3$ for a monolayer graphene sheet [153]. Measuring a high-intensity D band implies the existence of subdomain boundaries. The Bandwidth of the 2D peak is related to the number of layers. [154]. Linewidth of $\Delta\upsilon_{2D} \approx$30-40 cm^{-1} indicates that the graphene sample is monolayer. Up to 5 layers of graphene, the Raman spectrum is distinguishable from the spectrum of graphite.

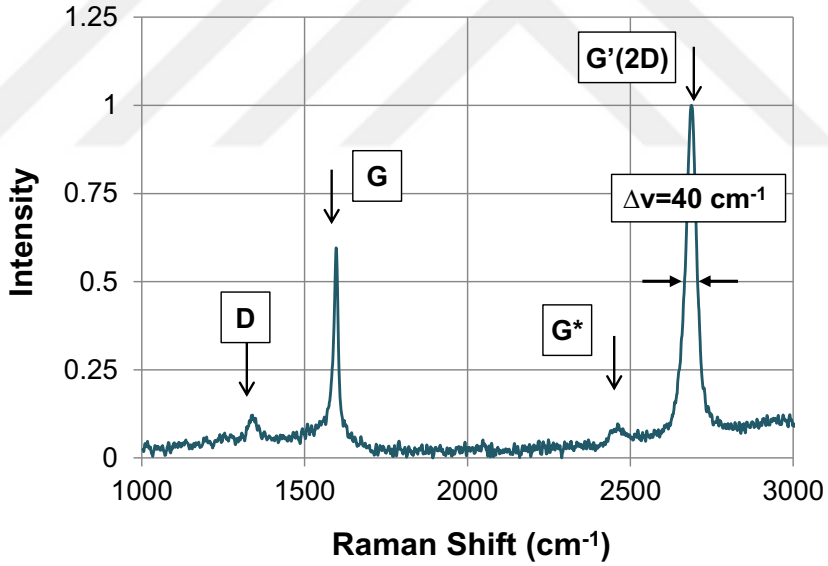

Figure 1-9: Experimentally measured Raman spectrum of the graphene on infrasil sample which was produced by our collaborators at Bilkent University (Adapted with permission from [34], The Optical Society).

Figure 1-9 shows the experimentally measured Raman spectrum of graphene-on-infrasil sample that was used in our experiments with the Cr^{3+}:LiSAF laser. In the spectroscopic characterization of the graphene sample, the Raman spectrum was first measured with a Renishaw inVia Raman microscope. The pump wavelength was 532 nm. For the graphene-on-infrasil sample, all of the four characteristic bands could be clearly identified, as can be seen in Fig. 1-9. Moreover, the intensity ratio of the D and G bands (I_D / I_G) and the full width at half maximum (FWHM, $\Delta\upsilon$) of the 2D band were measured to be 0.18 cm^{-1} and 40 cm^{-1}, respectively, indicating that the graphene sample used in our experiments was monolayer and nearly free of structural defects. The measured values of I_D / I_G and $\Delta\upsilon$ are in good agreement with previously reported values [153].

Since the monolayer graphene sample is used as a saturable absorber in the mode locking experiments, it is also important to investigate its ultrafast dynamics [155] and the absorption saturation behavior. A commercial time-resolved pump-probe spectrometer (HELIOS, Ultrafast systems) was used to perform the experiments. Two-color pump-probe measurement was performed by using two tunable optical parametric oscillators (TOPAS; Newport Spectra Physics), each seeded with a commercial Ti^{3+}:sapphire chirped-pulse amplifier (Spitfire ACE, Newport Spectra Physics), to provide the pump (850 nm) and probe (950 nm) beams. Figure 1-10 shows the variation of the fractional transmission ($\Delta T / T$) of the probe as a function of delay. The fast and slow decay times of the GSA were determined to be 128 fs and 1.630 ps, respectively, in good agreement with previously reported values in the literature [156].

At the delay that gives the maximum fractional transmission change, the probe transmission was further measured as a function of the pump fluence [Fig. 1-10 (b)]. From the analysis of the saturation data, based on a two-level rate equation model similar to what is described in Ref. [157], the best-fit values of the saturation fluence and modulation depth

(difference between the small-signal absorption and the saturated transmission) were determined to be 28 μJ/cm^2 and 0.62%, respectively. The small-signal transmission of the sample was determined to be 97.5% from absorbance measurements. The reason for the deviation of the modulation depth from the theoretical value of 2.3% requires further investigation and may be due to crystal imperfections that form during synthesis.

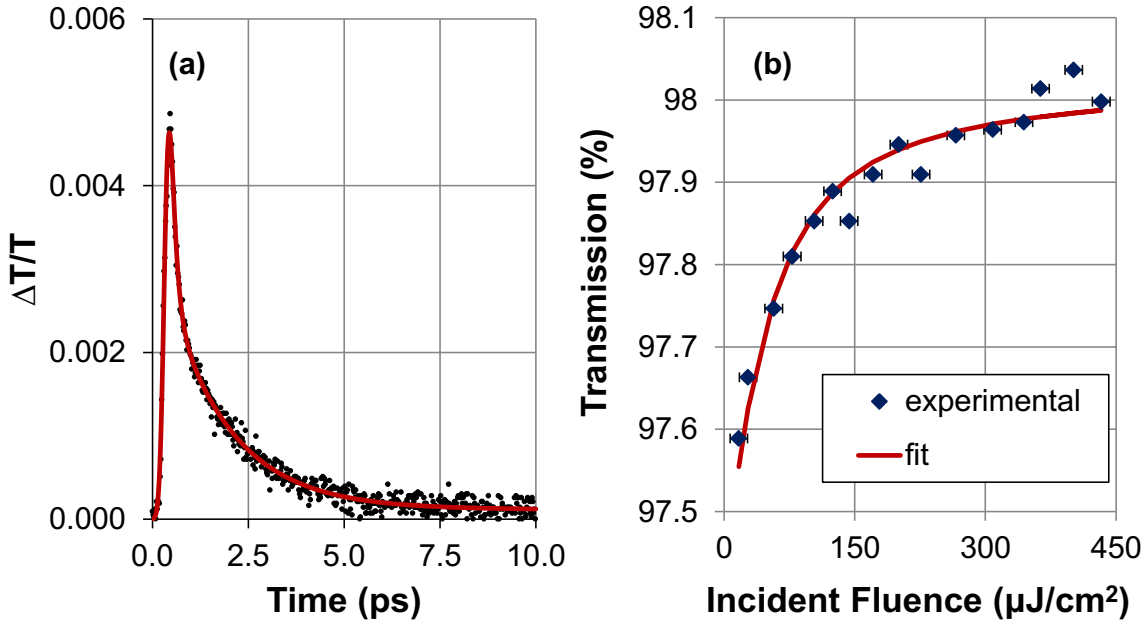

Figure 1-10: (a) Measured fast and slow decay times **(b)** saturation characteristics of the graphene sample that we used in our experiments (Adapted with permission from [34], The Optical Society).

In the case of graphene synthesis many processes can be used, such as exfoliation [135, 158-160], chemical vapor deposition [161-165], Langmuir-Blodgett method [166], carbon-dioxide reduction [167], intercalation [168] and so on. These methods give either monolayer or multilayer graphene sheets. We used a monolayer graphene-on-infrasil sample in our femtosecond Cr^{3+}:LiSAF experiments which was produced by our collaborators (the research group of Prof. Coskun Kocabas) at Bilkent University (Ankara) by using chemical vapor deposition (CVD) method. The other graphene-on-infrasil sample

that we used in the Tm^{3+}:YLF experiments was also produced by CVD technique at Korea Advanced Institute of Science and Technology by our collaborators.

The graphene sample from Bilkent University was synthesized by CVD on ultra-smooth copper foils (B1-SBS, Mitsui mining and smelting company, Ltd.). The copper foils were heated to 1035°C under hydrogen (H_2) flow to reduce the oxide layer of the copper foils. During the growth, the partial pressure of methane (CH_4) and H_2 gases were 1.5 and 3 Torr, with corresponding flow rates of 40 and 80 sccm, respectively. After 30 min, the growth was terminated by stopping the flow of methane, and then the samples were cooled down to room temperature under H_2 flow. In order to transfer the graphene layer onto an Infrasil window, our collaborators at Bilkent University coated the samples with thick photoresist film (Shipley 1813) and etched the copper in ferric chloride ($FeCl_3$) solution. The photoresist film was then placed on the infrasil window and heated to 120°C to initiate uniform coating on the surface. Cleaning the photoresist layer with acetone yielded large-area and high-quality graphene film on the infrasil window. Schematic of the fabrication process is shown in Fig. 1-11.

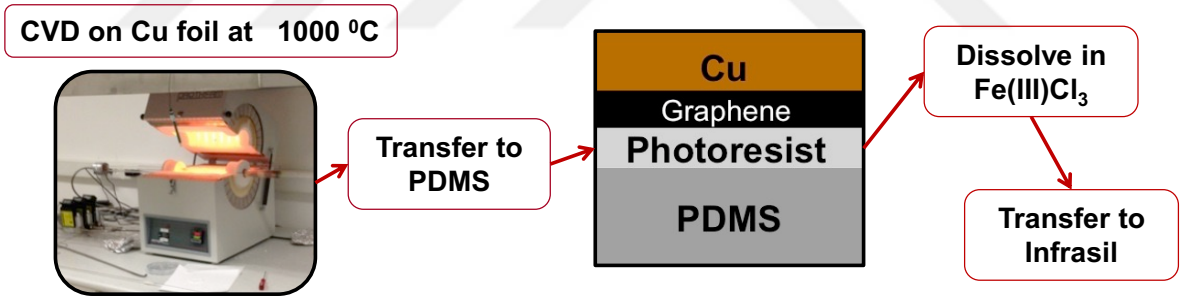

Figure 1-11: Schematic of the fabrication process of graphene sheet on the infrasil substrate.

The use of these graphene samples for femtosecond pulse generation from Cr^{3+}:LiSAF and Tm^{3+}:YLF lasers will be described in Chapters 3-4, and 6.

Chapter 2

2 BASICS of LASER RESONATOR DESIGN and PULSE MEASUREMENT METHODS

In Chapter 2, we describe the basic principles of laser resonator design, pulse generation techniques, mechanisms that cause pulse distortion and pulse width measurement techniques of femtosecond pulses.

2.1 ABCD Matrix Formalism

The ABCD matrix formalism is used for the design of an optical resonator. The ABCD matrix anaylsis is a 2-by-2 transfer matrix that is used to investigate how an optical element (e.g. lenses, reflective surfaces) or an optical system affects the characteristics of a light ray or a Gaussian beam. It is essential to work in the paraxial regime ($\sin\theta \approx \tan\theta \approx \theta$) to implement the ABCD matrix analysis. In the case of ray optics, the light ray is described by a vector, which includes the information of the offset (r) and offset angle (θ) with respect to an optical axis:

$$\vec{r} = \begin{bmatrix} r \\ \theta \end{bmatrix}. \tag{2.1.1}$$

In general, after a light ray (with r_i and θ_i) encounters an optical system, its height or offset angle are modified [169]. Assume that, the output ray has a different offset (r_f) and offset angle (θ_f). The parameters of the output depend on the initial parameters of the ray and can be determined by using the following relation:

$$\vec{r_f} = \begin{bmatrix} A & B \\ C & D \end{bmatrix} \vec{r_i}. \tag{2.1.2}$$

As is well known, to obtain light oscillation, optical amplification must be combined with positive feedback which is provided by the highly reflecting mirrors in a resonator.

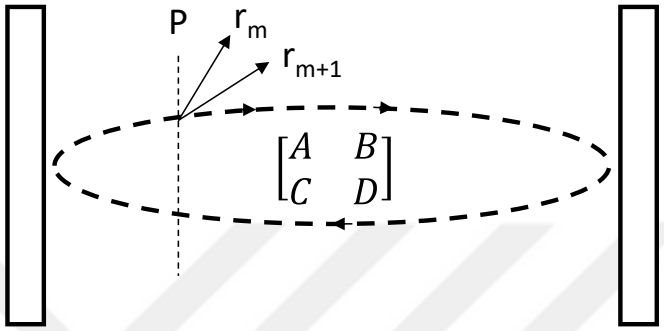

Figure 2-1: A generalized resonator showing the travelling ray after m and m+1 roundtrips at the same incident plane (P) [Adopted from [169]] .

Each optical element has its own transfer matrix. Multiplication of these matrices gives the resulting resonator transfer (ABCD) matrix. By using the ABCD matrix of a resonator, it is possible to investigate whether or not the optical resonator is stable. The stability analysis shows whether or not the beam is confined to the resonator after m ($m \gg 1$) round trips. For an optical resonator as shown in Fig. 2-1, the ray parameters after the m^{th} and $(m+1)^{th}$ roundtrips can be calculated from

$$\overrightarrow{r_{m+1}} = \begin{bmatrix} A & B \\ C & D \end{bmatrix} \overrightarrow{r_m}. \tag{2.1.3}$$

In a roundtrip, since the starting and ending point are the same (at a point on the plane of P) with the same refractive index, we have the condition that AD-BC=1. This leads to the stability condition [169]

$$\left| \frac{A+D}{2} \right| \leq 1. \tag{2.1.4}$$

The ABCD matrix method summarized above can also be used in the determination of the beam parameters of a Gaussian beam supported inside a laser resonator. The properties of the gaussian beam are summarized by the q-parameter which is given by

$$\frac{1}{q(z)} = \frac{1}{R(z)} - i\frac{\lambda}{n_0 \pi w^2(z)} \ . \tag{2.1.5}$$

Here, $w(z)$ and $R(z)$ are the spotsize and the radius of curvature functions of the Gaussian beam. The spot-size function gives the variation of the electric field in the radial direction. The radius of curvature function further describes a spherical wavefront of the Gaussian beam at a z position. Both $w(z)$ and $R(z)$ are functions of the Rayleigh range ($z_0 = \frac{kw_0^2}{2} = \frac{n_0 \pi w_0^2}{\lambda}$) which gives the distance over which the beam remains nearly collimated.

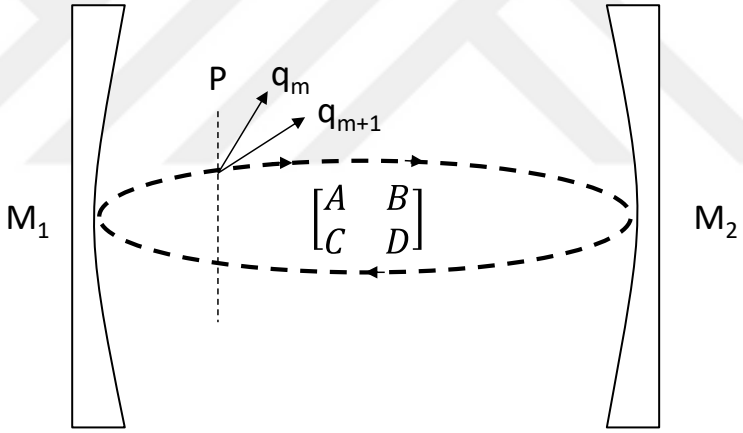

Figure 2-2: A general two-mirror resonator showing the q-parameter of the Gaussian beam after m and m+1 roundtrip [Adopted from [169]].

The q-parameters after $(m+1)^{th}$ and m^{th} rountrips are related through

$$q_{m+1} = \frac{Aq_m + B}{Cq_m + D}. \tag{2.1.6}$$

For the self-consistent Gaussian beam solution of the resonator, the q-parameter remains the same at each plane after one roundtrip (Fig. 2-2) and obeys the following relation:

$$q = \frac{Aq + B}{Cq + D} \ . \tag{2.1.7}$$

Solving Eq. (2.1.7), the relation between the q-parameter and ABCD matrix elements can be found as

$$\frac{1}{q} = \frac{D - A}{2B} \pm i \frac{\sqrt{1 - \left(\frac{A + D}{2}\right)^2}}{B}. \tag{2.1.8}$$

Comparing Eqs. (2.1.5) and (2.1.8), radius of curvature and spotsize functions are determined to be [169]

$$\frac{1}{R} = \frac{D - A}{2B} \tag{2.1.9}$$

and

$$\frac{\lambda}{n_0 \pi w^2} = \frac{\sqrt{1 - \left(\frac{A + D}{2}\right)^2}}{B} \tag{2.1.10}$$

in terms of matrix elements of the resonator.

2.2 Mode Locking

Mode locking is one of the important techniques to obtain femtosecond pulses from lasers. The first mode-locked laser was reported by Hargrove et al. in 1964 [170]. Typically, mode-locked lasers generate pulses in the range of picoseconds (10^{-12}) and femtoseconds (10^{-15}). The duration of the generated pulses is typically much shorter than the cavity round-trip delay time.

In a general optical resonator, infinitely many longitudinal modes oscillate with different phases. Assume that, the oscillating modes are at discrete resonant frequencies (υ_q) of the resonator. In particular, the frequency difference between two consecutive modes ($\upsilon_{FSR} = \upsilon_{q+1} - \upsilon_q = \frac{c}{2d}$, q: integer, c: the speed of light, d: the effective length of the resonator) is defined as the free-spectral range of the resonator. Typically, amplification bandwidth of solid-state gain media is broad enough to support many longitudinal modes in the resonator. Supposing that the resonator supports M oscillating discrete modes, the resulting electric field will be

$$E(t) = \sum_{q=0}^{M-1} E_q \exp\left(i\left(\omega_0 + q\omega_F\right)t + i\phi_q(t)\right) \tag{2.2.1}$$

with an amplitude (E_q) and phase ($\phi_q(t)$) of the q[th] mode. Here, ω_0 and ω_F show the reference angular frequency and the difference between angular frequency of two consecutive longitudinal modes [$\omega_F = \omega_{q+1} - \omega_q = 2\pi\upsilon_{FSR} = \frac{\pi c}{d}$]. If $\phi_q(t)$ varies randomly over time, the total electric field in Eq. (2.2.1) yields a nearly constant output power with small fluctuations over time. In the case of mode locking, the phase of each oscillating mode will be the same. At a constant phase factor ($\phi_q(t) = 0$) and a constant amplitude value of E_0, the total electric field can be determined to be

$$E(t) = E_0 \exp\left(i\omega_0 t\right) \frac{\sin\left(\frac{M\omega_F t}{2}\right)}{\sin\left(\frac{\omega_F t}{2}\right)} . \tag{2.2.2}$$

At $t=0$, the electric field has a local maximum $M \times E_0$. Another maximum could be obtained after one cavity round-trip time ($T_R = \frac{2\pi}{\omega_F} = \frac{2d}{c}$). The output power, in particular, changes as a function of time and is proportional to $M \times |E(t)|^2$ (the larger the number of locked modes, the larger the peak power of the generated pulses). The generated pulse width is related with the cavity round trip time, number of locked modes, and amplification bandwidth of the medium as follows:

$$\tau_p = \frac{1}{M}\left(\frac{2\pi}{\omega_F}\right) = \frac{T_R}{M} \approx \frac{1}{\Delta\upsilon}. \tag{2.2.3}$$

Since the number of locked modes is quite large in mode-locked solid-state lasers, the summation defined in Eq. (2.2.1) can be replaced with an integral. In practice, several phase distortion mechanisms must be considered in the mode-locking experiments. Following parts will present the pulse distortion mechanisms qualitatively. When all unwanted distortions are balanced inside the resonator, the shortest obtainable pulse duration for a particular spectral bandwidth can be generated. The spectral width and pulse duration are related through

$$\Delta\upsilon\tau_p = K \tag{2.2.4}$$

for a transform-limited pulse. Here, K is known as the time-bandwidth product. The value of K depends on the pulse profile (0.441 for Gaussian, 0.315 for secant-squared (sech^2)). To achieve mode-locked operation from a solid-state laser, active or passive mode locking schemes can be used. In active mode locking, a periodic loss mechanism is introduced into the resonator. The modulator is driven externally to obtain a periodic pulse train at the repetition frequency of the laser resonator. In passive mode locking, a saturable absorber is placed inside the resonator to modulate the intracavity losses so as to produce a periodic

train of pulses. In this thesis, we focus on the use of passive mode locking techniques in solid-state lasers.

2.2.1 Saturable absorber mode locking

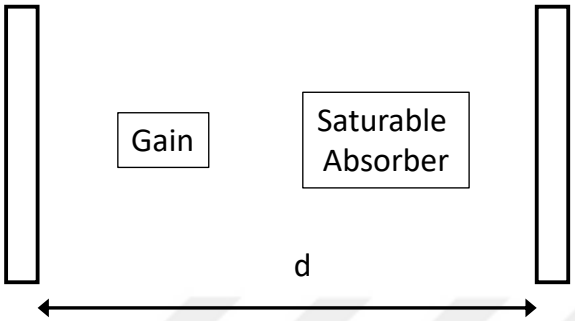

Figure 2-3: A typical two-mirror laser resonator including a gain medium and a saturable absorber [Adopted from [169]].

Generation of ultrashort pulses by using an intracavity saturable absorber, whose transmission increases with increasing intensity, is called passive mode locking. A generalized passively mode-locked laser resonator is shown in Fig. 2-3. To analyze the change in saturable absorption as a function of time, we model the loss modulation of the saturable absorber as

$$s(t) = \frac{s_0}{1 + \frac{I(t)}{I_{sat}}}, \tag{2.2.5}$$

where s_0(<1) is the unsaturated loss, $I(t)$ is the intensity of the laser beam as a function of time, and I_{sat} is the saturation intensity of the saturable absorber. If the recovery time of the saturable absorber is much shorter than the cavity round trip time, it is known as a fast-saturable absorber. In general, solid-state lasers are highly sensitive to intracavity losses, hence the loss of the saturable absorber is much lower than 1. Under this approximation, $s(t)$ becomes

$$s(t) = s_0 - s_0 \frac{I(t)}{I_{sat}} = s_0 - s_0 \frac{|a(t)|^2}{I_{sat} A_{eff}} \equiv s_0 - \gamma |a(t)|^2 . \tag{2.2.6}$$

Above, A_{eff} is the effective beam area on the saturable absorber, $|a(t)|^2$ is the instantaneous power of the beam, and γ is the self-amplitude modulation (SAM) coefficient. The master equation for the case of passive mode locking can be written as follows:

$$\frac{1}{T_R}\frac{\partial}{\partial T} a = (g - l) a + \frac{g}{\Omega_g^2}\frac{\partial^2}{\partial t^2} a + \gamma |a|^2 a \tag{2.2.7}$$

where a is the normalized amplitude, Ω_g is the modulation bandwidth, g and l are the gain and loss mechanisms in the resonator. The master equation describes how a pluse evolves in a mode-locked laser resonator. Hyperbolic secant function can be found as a solution

$$a_0(t) = A_0 \text{sech}\left(\frac{t}{\tau}\right) \tag{2.2.8}$$

where

$$\frac{1}{\tau^2} = \frac{\gamma A_0^2 \Omega_g^2}{2g} \tag{2.2.9}$$

and

$$l - g = \frac{g}{\Omega_g^2 \tau^2} . \tag{2.2.10}$$

Note that as the pulse width gets shorter, the intensity increases and the modulation depth also increases, which is typical in passive mode locking.

2.2.2 Kerr-lens mode locking

Kerr-effect is a third-order nonlinear optical effect, which occurs as a result of the interaction between high intensity light with matter. In general, the high intensity electric field induces higher order polarization components inside a medium. Sufficiently high intensity electric fields can induce an intensity dependent refractive index contribution to the ordinary refractive index of a medium. The refractive index of the medium becomes

$$n = n_0 + n_2 I \ . \tag{2.2.11}$$

Here, n_0 is the ordinary refractive index, n_2 is the nonlinear refractive index, and I is the intensity of the light beam. The Kerr-effect leads to a variation in both temporal and spatial profile of a high intensity beam. In the spatial domain, for a positive nonlinear refractive index, the propagating laser beam undergoes a self focusing inside the gain medium which is called Kerr-lensing.

A typical laser beam has a Gaussian intensity distribution, which has higher intensity at the center. Since higher intensity experiences higher change in refractive index, the Gaussian beam distribution undergoes a higher change in refractive index at the center. This resembles a converging lens and causes self-focusing as shown in Fig. 2-4. In general, this self-focusing mechanism occurs inside the laser gain medium and acts as a fast-saturable absorber. This mechanism is called Kerr-lens mode locking and has been used to generate ultrashort pulses since 1991 [24].

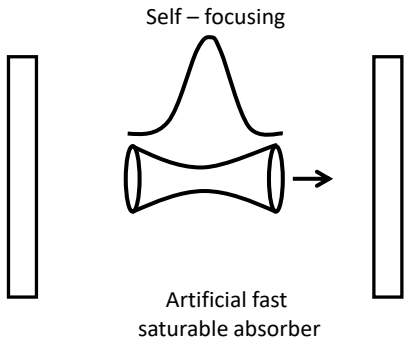

Figure 2-4: The Kerr-effect and self-focusing inside a Kerr medium for a Gaussian intensity distribution [Adopted from [171]].

In addition to the effect on the spatial profile of the beam, intensity dependent refractive index change induces a time varying phase across the pulse also. This phenomenon is known as self-phase modulation. The effect on the phase is similar to positive group delay dispersion which will be described in the following section.

2.3 Group Delay Dispersion (GDD)

While an ultrashort pulse propagates in a nonlinear dispersive medium, nonlinear effects can distort the spatio-temporal profile of the electric field. Since the refractive index is wavelength dependent, different wavelengths will propagate with different velocities, resulting in a time delay between different wavelength components. Second order dispersion is defined as

$$D = \frac{d^2\Phi}{d\omega^2} = l\frac{d^2\mathrm{k}}{d\omega^2} = l\frac{\lambda^3}{2\pi c^2}\frac{d^2\mathrm{n}}{d\lambda^2} \tag{2.3.1}$$

in ultrafast optics. Here, Φ is the phase of the electric field of the propagating pulse, k is the wave vector, n is the refractive index of the medium, ω and λ are the angular frequency and the wavelength. The sign of the dispersion can be negative or positive in

relation with the effect on the phase of the propagating pulse. Whether the group delay dispersion is positive or negative pulse broadening occurs. In the case of negative group delay dispersion (D<0), the low frequency components travel faster than the high frequency components, leading to a pulse broadening in the temporal domain. The effect of self-phase modulation (SPM) and positive dispersion is similar and in both cases, the dynamic frequency of the leading edge is downshifted [169]. The effect of SPM which is induced by the Kerr-effect must be balanced with negative group delay dispersion (GDD) in order to produce solitary optical pulses.

Solitary optical pulses propagate with minimum distortion and maintain their shape. If the third-order nonlinearities inside a passively-mode-locked laser resonator are balanced, solitary optical pulses can be generated. Solitary optical pulses obey the soliton area theorem, which gives the relation between the intracavity energy and pulse width. The soliton area theorem [171] is given by

$$W = \frac{7.04 \times |D|}{\delta \tau_p} , \tag{2.3.2}$$

where W, D, and τ_p are intracavity energy, second order group delay dispersion, and pulse width. Physically, W corresponds to the intracavity energy at which solitary pulses propagate with minimum distortion in the medium. δ is defined as the Kerr nonlinearity and given by

$$\delta = \frac{4}{\lambda} \frac{n_2 L}{w_{rms}^{\ 2}} . \tag{2.3.3}$$

Here, n_2 and L is the nonlinear refractive index and length of the medium, w_{rms} is the root-mean-squared spot size inside the medium.

2.4 Characterization of Femtosecond Pulses

State of the art electronic methods are not fast enough to measure femtosecond pulse durations. To characterize femtosecond pulses, optical interferometric techniques are used. In particular, Michelson interferometers can be used to measure ultrashort optical pulses by using second harmonic generation (SHG) or two-photon absorption (TPA) processes. The first diagnostic of an ultrashort pulse using an autocorrelator was reported in 1966 [172, 173]. The autocorrelation is the special case of a cross-correlation function. For the case of cross-correlation, one can use n different sources with different delay times to calculate the SHG signal. The mathematical expression of the cross-correlation function for n different sources of normalized electric fields is

$$g_B^n\left(\tau_1,\tau_2,\ldots,\tau_{n-1}\right)=\frac{\int_{-\infty}^{\infty}\left\{E_1(t)+E_2\left(t+\tau_1\right)+\ldots+E_n\left(t+\tau_{n-1}\right)\right\}^{2n}dt}{\int_{-\infty}^{\infty}\left\{E_1^{2n}(t)+E_2^{2n}(t)+\ldots+E_n^{2n}(t)\right\}dt}\ . \qquad (2.4.1)$$

τ_n defines the delay of the nth electric field. In the case of the autocorrelation, there is only one source of electric field, meaning that a light source is aligned to the entrance of an interferometer (input beam in Fig. 2-5). As in Fig. 2-5, the input beam is sent into an interferometer (M1) and split into two arms by using a beam splitter (BS). The separated beams are reflected back from the corner cubes 1 and 2 (Fig. 2-5) so as to overlap on the second beam splitter. While one is reflected back from a corner cube mirror the other one is delayed with a special driving function (e.g. ramp or sine function). Next, the beam is focused into a second-harmonic crystal (SHG x-tal) by using an off-axis parabolic mirror. After the pump beam is filtered out by using a short-pass filter, the obtained pattern is measured with a detector (Fig. 2-5) and an oscilloscope.

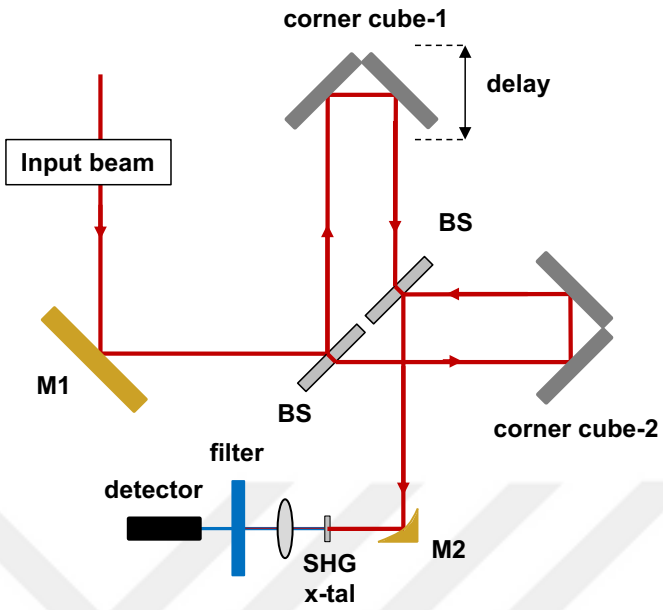

Figure 2-5: The autocorrelation setup that we used to measure the durations of the generated pulses from the Cr^{3+}:LiSAF laser.

Depending on the bandwidth limit of the detector, the generated autocorrelation signal has different forms, giving the same pulse width information. Mathematical expressions for the generated SHG signal from an intensity and interferometric autocorrelation will be investigated.

In the case of the autocorrelation, two beams ($n = 2$) overlap so as to produce the SHG signal. While one pulse crossing over the other inside the SHG crystal, the resulting autocorrelation signal [174] is given by

$$g_B^2(\tau) = \frac{\int_{-\infty}^{\infty} \{E(t) + E(t+\tau)\}^{2\times 2}\, dt}{2\int_{-\infty}^{\infty} E^{2\times 2}(t)\, dt} \,. \qquad (2.4.2)$$

Hence, the resulting autocorrelation signal $[g_B^2(\tau)]$ becomes

$$g_B^2(\tau)=\frac{\int_{-\infty}^{\infty}\left\{E^4(t)+E^4(t+\tau)\right\}dt+4\int_{-\infty}^{\infty}E^3(t)E(t+\tau)dt+4\int_{-\infty}^{\infty}E(t)E^3(t+\tau)dt+6\int_{-\infty}^{\infty}E^2(t)E^2(t+\tau)dt}{2\int_{-\infty}^{\infty}E^4(t)dt}.$$

(2.4.3)

If the data are recorded with a much faster detector than the driving frequency of the adjustable delay mirror, electric field of the autocorrelation signal will be calculated from Eq. (2.4.3). For the case of fast detection, the autocorrelation is known as interferometric autocorrelation. At zero delay $[g_B^2(\tau=0)]$ [1], the maximum overlap between two pulses gives

$$g_B^2(\tau=0)=\frac{16\int_{-\infty}^{\infty}E^4dt}{2\int_{-\infty}^{\infty}E^4(t)dt}=8. \tag{2.4.4}$$

For large delays $[g_B^2(\tau=\infty)]$, the minimum overlap between two pulses, gives the background signal to be

$$g_B^2(\tau=\infty)=\frac{2\int_{-\infty}^{\infty}E^4dt}{2\int_{-\infty}^{\infty}E^4(t)dt}=1, \tag{2.4.5}$$

resulting in a contrast ratio of 8:1. An example of an interferometric autocorrelation signal is given in Fig. 2-6 for the case of 13-fs pulses which were generated from a Kerr-lens mode locked Cr^{3+}:LiSAF laser at the center wavelength of 850 nm.

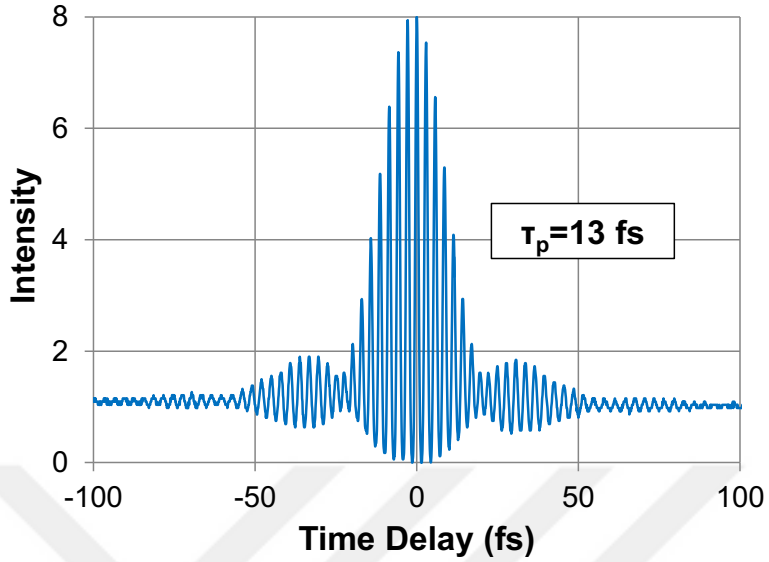

Figure 2-6: An example of an interferometric autocorrelation trace. Data were recorded from a Kerr-lens mode locked Cr^{3+}:LiSAF laser generating 13-fs pulses (Adapted with permission from [106], The Optical Society).

In the case of slow detection, the form of the autocorrelation signal is called intensity autocorrelation. Depending on the alignment of the autocorrelator, the background of the SHG signal could be eliminated. In this thesis study, intensity autocorrelation was not used in the measurements. Hence, I will only give a brief introduction of the electric field for the intensity autocorrelation with background and show an example of it. If the detection is slow, then the resulting electric field will be the optical time averaged electric field ($G_B^2(\tau)$) and hence can be calculated from

$$G_B^2(\tau) = 1 + 2\frac{\int_{-\infty}^{\infty}\left\{E^2(t)E^2(t+\tau)\right\}dt}{\int_{-\infty}^{\infty}E^4(t)dt}. \qquad (2.4.6)$$

Again, to find the contrast ratio, $G_B^2(\tau=0)$ and $G_B^2(\tau=\infty)$ will be calculated as follows

$$G_B^2(\tau=0)=1+2\frac{\int_{-\infty}^{\infty}E^4(t)\,dt}{\int_{-\infty}^{\infty}E^4(t)\,dt}=3, \tag{2.4.7}$$

and

$$G_B^2(\tau=\infty)=1+2\frac{0}{\int_{-\infty}^{\infty}E^4(t)\,dt}=1. \tag{2.4.8}$$

This results in a contrast ratio of 3:1. An example of an intensity autocorrelation signal is given in Fig. 2-7.

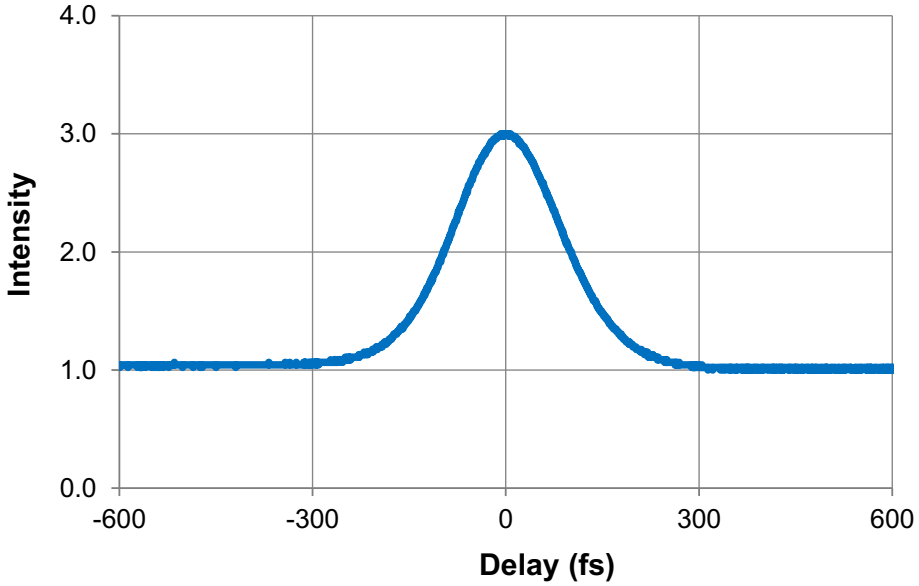

Figure 2-7: An example of an intensity autocorrelation.

As can be seen from Eq. (2.4.3) and Eq. (2.4.6), some information is lost in the intensity autocorrelation. These additional parts in the electric field of the interferometric autocorrelation function give phase chirp information of the generated pulses. To measure the pulse width with an interferometric autocorrelator, the period of the center wavelength of the pulses needs to be calculated from

$$T = \frac{\lambda}{c} \ . \tag{2.4.9}$$

Once the period is found for a wavelength, number of measured cycles (above FWHM of the SHG signal) needs to be counted. The multiplication of the number of cycles and period gives the pulse width ($\tau = 1.55\tau_p$, for sech^2 pulse shape). The contrast ratio of each case shows that the optical alignment of the autocorrelator is good enough to measure a pulse width. The ratio further gives an idea about the quality of mode-locked operation.

Chapter 3

3 GRAPHENE MODE-LOCKED Cr^{3+}:LiSAF LASER at 850 nm

In this chapter, a mode-locked femtosecond Cr^{3+}:LiSAF laser initiated with a high-quality monolayer graphene saturable absorber will be presented. To the best of our knowledge, this was the first graphene-based mode-locked operation of the Cr^{3+}:LiSAF laser. In the first part of Chapter 3, experimental setup of the continuous wave Cr^{3+}:LiSAF laser will be introduced. This will be followed by the mode locking results that is obtained from graphene included Cr^{3+}:LiSAF laser. In the last part of Chapter 3, soliton area theorem analysis and a brief discussion will be presented.

3.1 Experimental Setup and Continuous-wave Results

To investigate fast saturable action in graphene, we used a diode-pumped, compact, and low-cost Cr^{3+}:LiSAF laser operating near 850 nm. Before mode-locking experiments, we first start with an astigmatically compensated x-cavity Cr^{3+}:LiSAF laser as shown in Fig. 3-1(a). Two single-mode diodes (SMD-1 and SMD-2), which can be powered by two AA-type batteries, were used to excite the Cr^{3+}:LiSAF gain medium. The output beam of each diode was collimated with an aspheric lens (L1 and L2, f=4.5 cm). The output polarizations of SMD-1 and SMD-2 were adjusted to be orthogonal so that the two pump beams could be polarization coupled with a polarizing beam splitter (PBS). The combined pump beam was focused by using a convex lens (L3, f=60 mm) inside the Brewster-cut, 7-mm-long, and 1.5% Cr^{3+}-doped LiSAF gain medium which absorbs 98% of the pump at 660 nm. The x-

cavity Cr^{3+}:LiSAF laser resonator contained two curved high reflectors (M1 and M2, ROC=75 mm), a flat high reflector (M3), and a partially reflective output coupler (OC). Based on ABCD matrix formalism, laser waist inside the gain medium was estimated to be 16 µm. Before mode-locking experiments, as shown in Fig. 3-1(b) M3 was replaced with additional curved mirrors (M4-M5), each with 75 mm of radius of curvature (M4 and M5), were added to obtain an additional waist on the graphene saturable absorber. Additionally, the cavity was completed by using a high reftector mirror(M6).

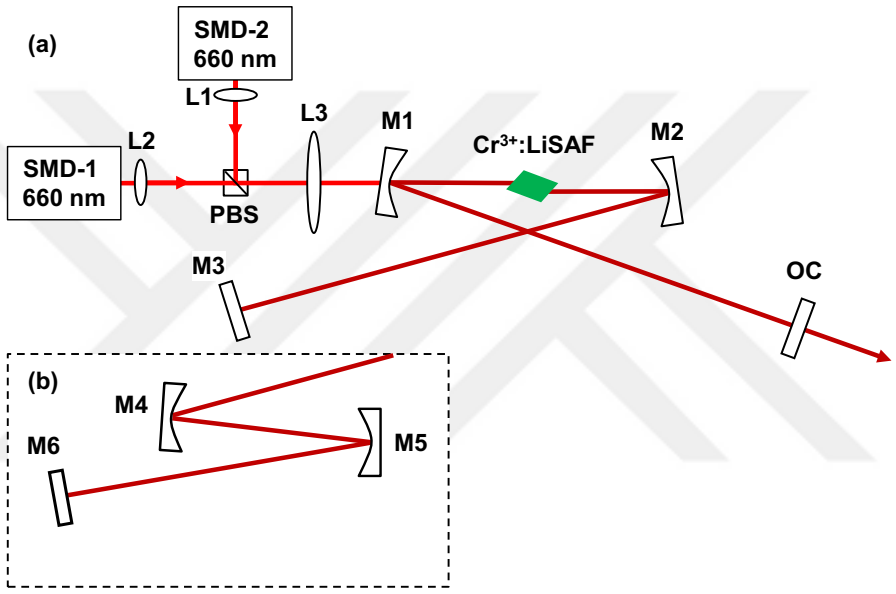

Figure 3-1: (a) Experimental arrangement of the cw Cr^{3+}:LiSAF laser operating near 850 nm. (b) The Cr^{3+}:LiSAF experimental setup after the addition of curved mirrors and an high reflector.

To investigate passive losses of the resonator, we measured the threshold pump power with different output couplers for the experimental setup shown in Fig. 3-1(b). Figure 3-2 shows the measured threshold pump power variation of the cw Cr^{3+}:LiSAF laser as a function of output coupling. Based on Findlay-Clay analysis [175], the small-signal loss of the crystal was estimated to be 0.55%. This loss included all the cavity and crystal losses, showing that mirrors and the crystal have low parasitic losses.

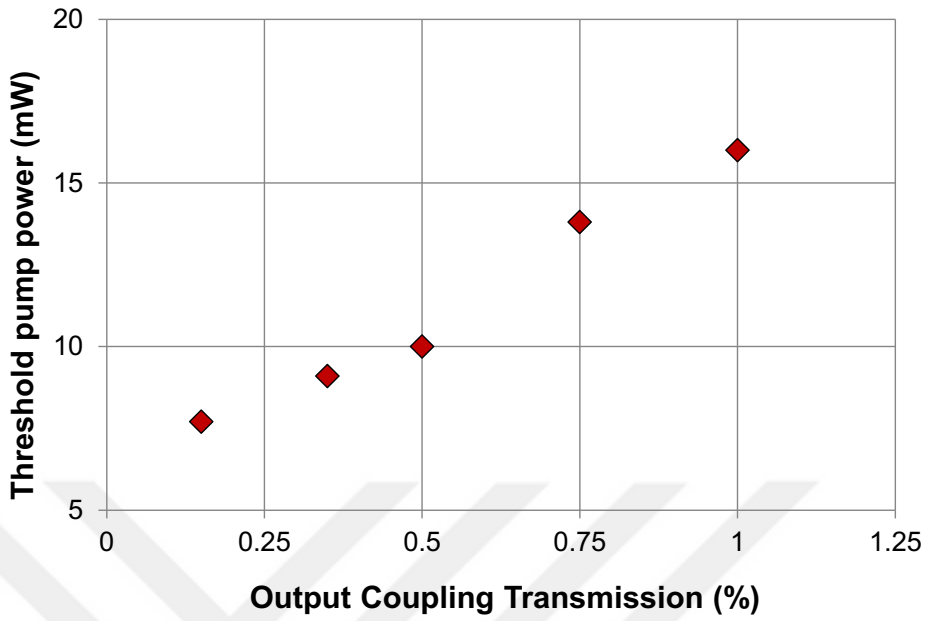

Figure 3-2: Measured threshold pump power levels as a function of output coupling (Adapted with permission from [34], The Optical Society).

Figure 3-4 further shows the variation of the cw output power as a function of the pump power for different output coupling levels. With a total pump power of 270 mW, output power of 101 mW was obtained by using the 1% transmitting output coupler. With 1% output coupler, as high as 40% of slope efficiency could be obtained. In the case of 1% output coupling, optical-to-optical conversion efficiency was 37%, which was quite higher than that for diode-pumped Ti^{3+}:sapphire lasers [176]. Measuring output power variation of the cw Cr^{3+}:LiSAF laser as a function of output coupling, the optimum output coupler of the resonator could be diagnosed. As shown in Fig. 3-3, 0.5%, 0.75%, and 1% have higher output powers at the pump power of 270 mW. Since the inclusion of the GSA provides additional losses of about 2.3% per transit, mode-locking experiments were conducted by using the 0.5% transmitting output coupler to provide higher intracavity pulse energy. Additionally, slope efficiencies of each output coupler were measured by changing the

input power. As can be seen from Fig. 3-4, slope efficiency increases with increasing output coupling level.

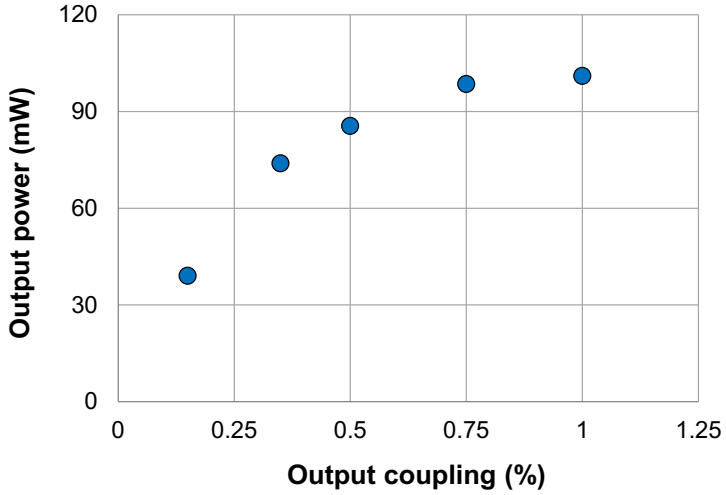

Figure 3-3: Output power variation as a function of output coupling at the pump power of 270 mW.

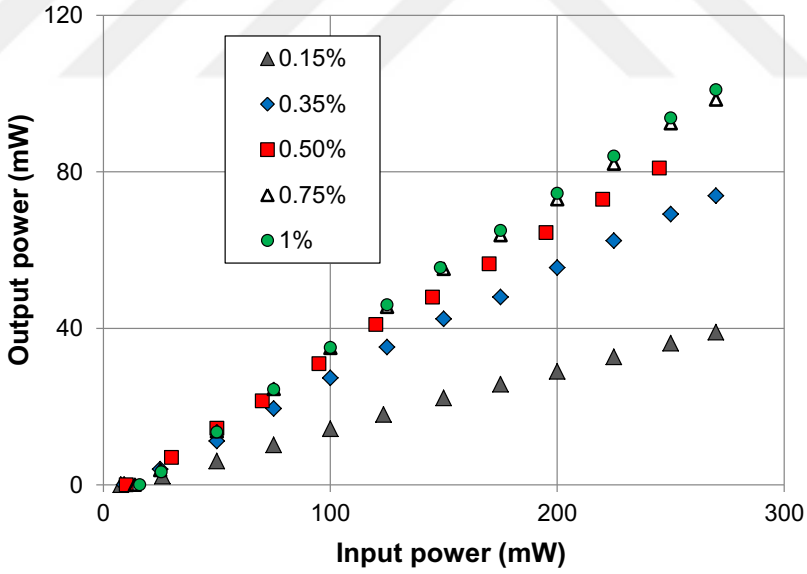

Figure 3-4: Output power variation of the Cr^{3+}:LiSAF laser using different output couplings as a function of incident power (Adapted with permission from [34], The Optical Society).

Furthermore, the GSA was positioned at Brewster incidence in between two additional concave high reflectors [M3 and M4, radius of curvature 75 mm, in Fig. 3-1(b)]. Photograph of the experimental setup including the GSA is shown in Fig. 3-5. The high reflector and output coupler arm lengths were 62 and 41 cm, respectively, giving an estimated beam waist of 30 μm on the GSA sample. The total cavity length was 1.12 m, corresponding to a repetition rate of 132 MHz.

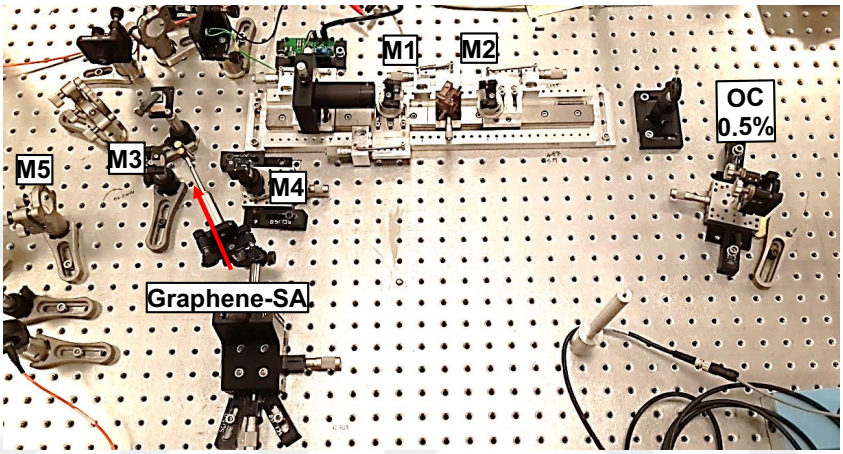

Figure 3-5: A photograph of the GSA mode-locked experimental setup

3.2 Mode Locking Results

Once the GSA was inserted into the cavity, cw mode-locked operation could be readily obtained by translating the output coupler. Inclusion of the GSA reduced the maximum cw output power of the laser from 86 to 10 mW, as shown in Fig. 3-6.

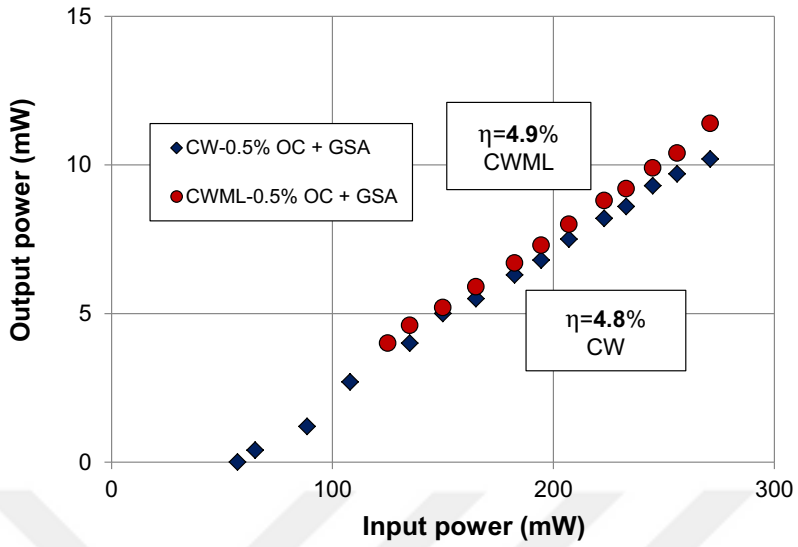

Figure 3-6: Measured output power variation of GSA included cavity for the cases of cw and cw-mode locked (Adapted with permission from [34], The Optical Society).

$$\frac{P_{th-cw}}{P_{th-graphene}} = \frac{T + L_{cavity}}{T + L_{cavity} + L_{graphene}} \tag{3.2.1}$$

By comparing the threshold pump powers ($P_{th\text{-}cw}$ and $P_{th\text{-}graphene}$) of the laser with and without the GSA as in Eq. (3.2.1), the round-trip insertion loss of the GSA was estimated to be 4.9%, in good agreement with twice the measured small-signal absorption of 5%. In Eq. (3.2.1), T is the transmission of the output coupler (0.5%), L_{cavity} is the loss of the resonator without the GSA (0.55%), and $L_{graphene}$ is the loss of the GSA. Once mode locking was initiated, the output power of the Cr^{3+}:LiSAF laser including GSA slightly increased as shown in Fig. 3-6. Since the saturated absorption of the GSA at higher intracavity peak powers leads to lower overall resonator loss during mode-locked operation, somewhat higher output powers were obtained during mode-locked operation in comparison with the cw case. The corresponding maximum fluence on the GSA was determined to be 606 $\mu J/cm^2$, suggesting that based on our saturation measurements, the

GSA was fully saturated. Pure and stable mode-locking operation could be initiated at any pump power level above 130 mW (corresponding output power 4 mW). As the input power was decreased, initiation of mode locking became more difficult. Below 130 mW of pump power, pulsed operation could not be initiated. In this regime, although a Q-switching tendency was observed by translating the output coupler mirror, stable Q-switching operation could not be obtained.

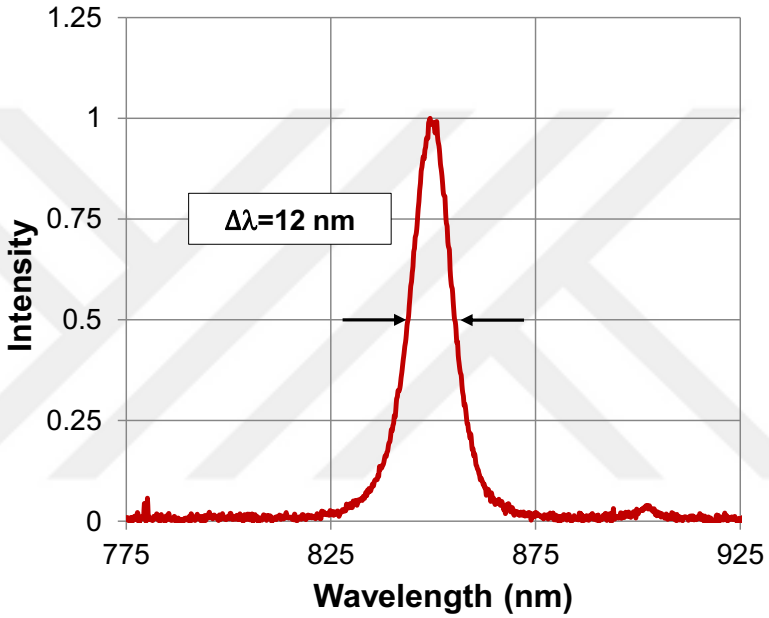

Figure 3-7: Measured optical spectrum of the generated pulses from the GSA mode-locked Cr^{3+}:LiSAF laser (Adapted with permission from [34], The Optical Society).

Figure 3-7 shows the measured optical spectrum of the femtosecond pulses generated with the GSA mode-locked Cr^{3+}:LiSAF laser [34]. The optical spectrum was centered at 850 nm with a spectral width of 12 nm. The bandwidth suggests 63-fs pulse width, assuming $sech^2$ pulse shape. Figure 3-8(a) shows interferometric autocorrelation trace of the femtosecond pulses generated from the Cr^{3+}:LiSAF laser. The measured pulse

width was 68 femtoseconds. At the center wavelength of 850 nm, the pulse duration and spectral bandwidth measurements yielded 68 fs (assuming a $sech^2$ intensity profile) and 12 nm, respectively, with a corresponding time–bandwidth product of 0.338, indicating that the pulses were nearly transform limited. Furthermore, in the RF spectrum measurements shown in Fig. 3-8(b), the sideband noise level was determined to be 70 dB below the fundamental tone at 132 MHz (resolution bandwidth 1 kHz). The mode-locking data shown in Figs. 3-7, 3-8(a), and 3-8(b) were taken at an input power of 270 mW with a 0.5% output coupler. The maximum mode-locked output power was 11.5 mW.

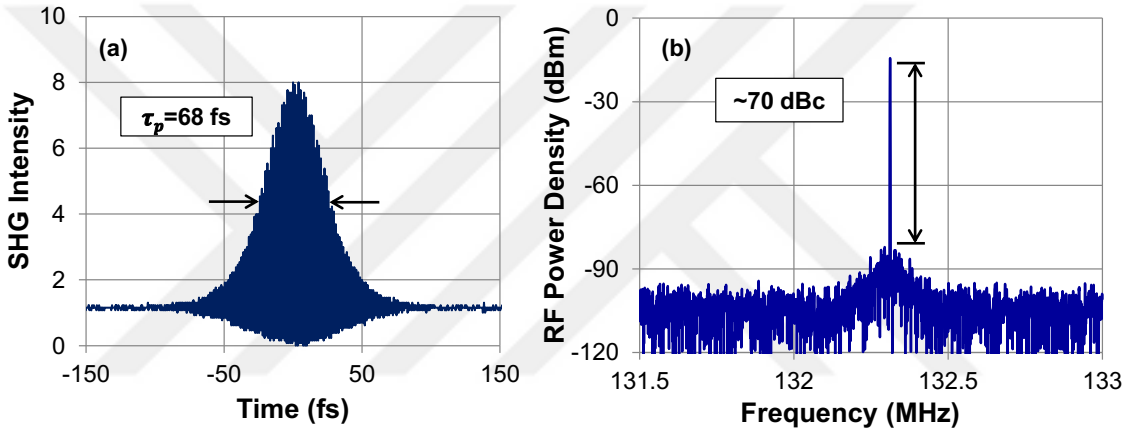

Figure 3-8: The measured interferometric autocorrelation and radio frequency spectrum of the generated pulses from the graphene-mode locked Cr^{3+}:LiSAF laser (Adapted with permission from [34], The Optical Society).

3.3 Soliton Area Theorem Analysis

To obtain solitary pulses, dispersion management was employed by using commercial and custom-made dispersion-control optics [M1 and M2, each with −80±10 fs^2 of group delay dispersion (GDD) per bounce; M5, with −40±10 fs^2 of GDD per bounce]. The material dispersion contributions of the gain crystal and infrasil substrate were estimated based on their Sellmeier equations given as follows:

$$n_{Cr:LiSAF} = \sqrt{1.98448 + \frac{0.00235}{\lambda^2 - 0.10936} - 0.01057\lambda^2} \quad (3.3.1)$$

$$n_{Infrasil} = \sqrt{1 + \frac{0.476523070\lambda^2}{\lambda^2 - 0.00284888095} - \frac{0.627786368\lambda^2}{\lambda^2 - 0.0118369052} - \frac{0.872274404\lambda^2}{\lambda^2 - 956856012}}. \quad (3.3.2)$$

The dispersion contribution of Cr^{3+}:LiSAF and infrasil media were 24 and 40 fs^2 per mm, respectively. Because the net GDD of the cavity was close to zero, it was not possible to determine the overall dispersion from the nominal GDD values given above, since the actual GDD values of the mirror coatings are uncertain due to the dependence on the angle of incidence. Instead, based on the soliton area theorem [Eq.(2.3.2)], operation parameters of the Cr^{3+}:LiSAF laser, and the nonlinear refractive index of Cr^{3+}:LiSAF (0.8×10^{-20} m^2/W) [177], the net round-trip cavity GDD was estimated to be -75 fs^2.

The tight-focusing resonator architecture made it possible to operate the Cr^{3+}:LiSAF laser with only two 135 mW, 660 nm low-cost single-mode diode lasers. At the pump power of 270 mW, the Cr^{3+}:LiSAF laser produced nearly transform-limited 68 fs pulses with an average power of 11.5 mW at 850 nm. The repetition rate was around 132 MHz, corresponding to a pulse energy and peak power of 86 pJ and 1.26 kW, respectively. Once mode locking was initiated with the GSA, stable, uninterrupted femtosecond pulse generation could be sustained for hours.

Chapter 4

4 GENERATION of SUB-20-FS PULSES FROM A GRAPHENE MODE-LOCKED LASER

In Chapter 3, the shortest pulse generation experiments in a graphene mode-locked solid-state laser will be presented. We demonstrate, what is to our knowledge, the shortest pulses directly generated from a graphene mode-locked laser. In the first part of Chapter 3, experimental setup of the mode-locked laser was shortly described. Next, mode locking results were introduced. These will be followed by femtosecond tuning experiments. In the final part of Chapter 3, a detailed mode locking initiation test is described.

4.1 Experimental Setup

The ultrabroad saturable absorption of graphene saturable absorbers (GSAs) in principle impose no bandwidth limitation during mode locking, leading to pulse durations only limited by the amplification bandwidth of the gain medium and dispersion of the cavity. Before our study, the shortest pulses obtained from a GSA mode-locked laser had a duration of 30-fs (Yb^{3+}:$CaYAlO_4$ laser) [144]. To reach the limits of graphene, we used a Cr^{3+}:LiSAF laser, whose dispersion and gain characteristics were well-defined in the literature. GSA mode locked Cr^{3+}:LiSAF laser was set up similar to the one defined in Chapter 1. We added a pair of prisms to fine tune the dispersion in the resonator. Additionally, the gain medium was replaced with a 6-mm, 1.5%, Brewster cut Cr^{3+}:LiSAF crystal. Total absorption of the crystal was near 98% at the pump wavelength of 660 nm. A

schematic of the sub-20-fs, GSA mode-locked Cr^{3+}:LiSAF laser is shown in Fig. 4-1. The laser resonator consisted of two concave focusing mirrors, each with a radius of curvature (ROC) of 75 mm (M1 and M2), a pair of fused silica prisms (FSP1 and FSP2), a highly reflecting end mirror (M5), and an output coupler with 0.5% transmission (OC). A second intracavity beam waist was formed by using two additional curved high reflectors (M3 and M4, ROC=75 mm). The monolayer GSA was placed between M3 and M4 mirrors to increase the beam fulence on the saturable absorber. The GSA used in our experiments was prepared by our collaborators at Bilkent University as described in Chapter 1. To reduce reflection losses, the GSA was further placed at Brewster incidence. The prism pair (FSP1 and FSP2) with a tip-to-tip separation of 29 cm was placed in the high reflector (HR) arm for dispersion control. HR and OC arm lengths were 88 cm and 41 cm, respectively, whereas the total cavity length was 138 cm (pulse repetition rate=107 MHz).

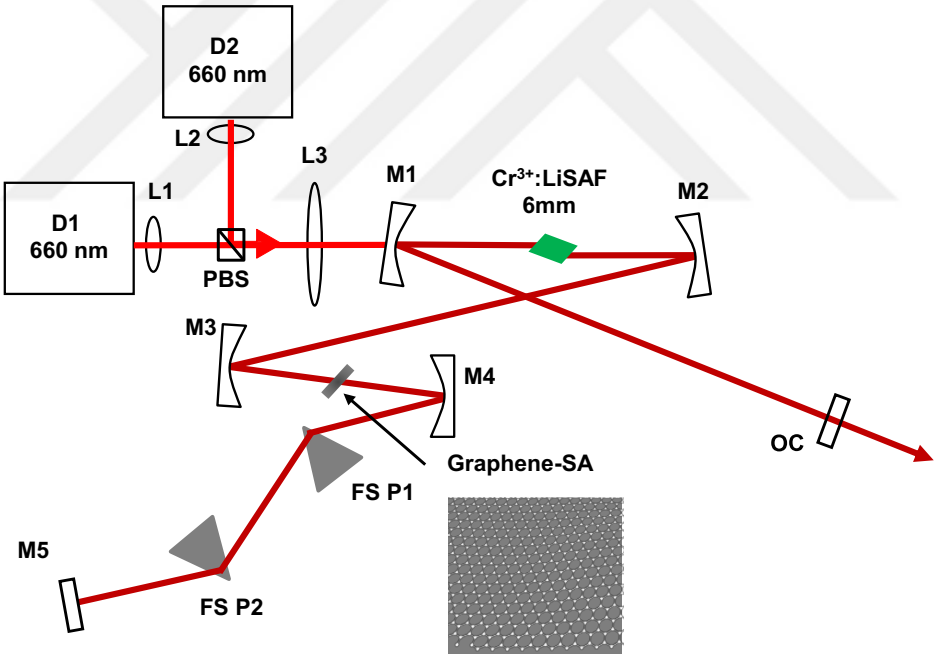

Figure 4-1: A schematic of the GSA mode-locked Cr^{3+}:LiSAF laser (Adapted with permission from [40], The Optical Society).

Figure 4-2 (a) shows the power efficiency curves for the continuous-wave (cw) Cr^{3+}:LiSAF laser (containing the prism pair and an infrasil substrate) with different output couplers. We used the 0.5% output coupler in the mode locking experiments, in order to maintain a high intracavity power and to remain near the optimum output coupling of the resonator. By using the 0.5% output coupler, as high as 75 mW of output power was obtained near 850 nm with 275 mW of incident pump power [Figure 4-2(a)]. After the insertion of the GSA, the output power of the laser decreased to 6.2 mW (0.5% output coupler). At each output coupling level, power performance of the Cr^{3+}:LiSAF laser was further measured with graphene as shown in Fig. 4-3. By using the power efficiency data [Figure 4-2(a)] as well as the pump threshold data [Figure 4-2(b)], we estimated the round-trip loss of the free-running laser and GSA to be 0.4% and 4.1%, respectively.

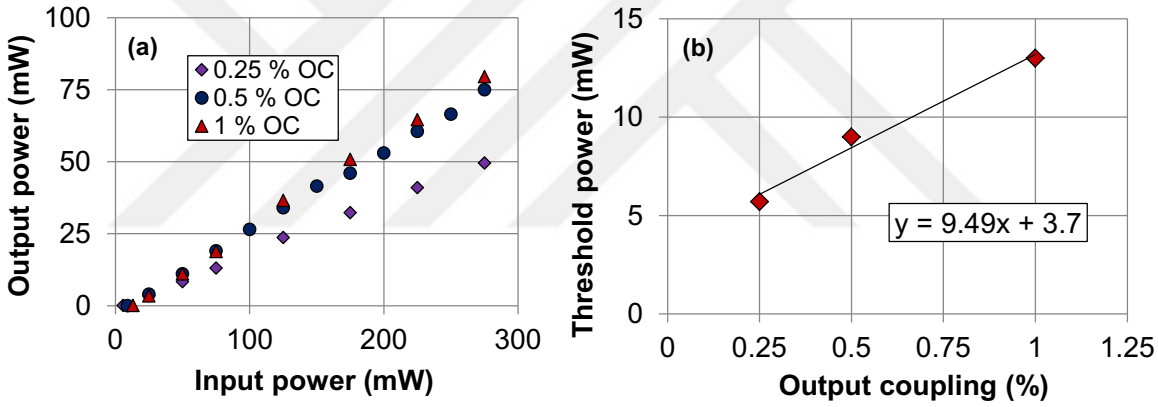

Figure 4-2: (a) Power efficiency and **(b)** measured threshold pump powers as a function of output coupling of the Cr^{3+}:LiSAF laser (containing the prism pair and an infrasil substrate) (Adapted with permission from [40], The Optical Society).

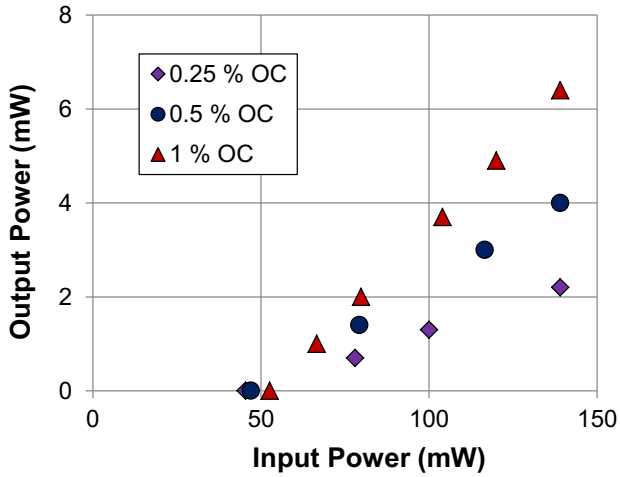

Figure 4-3: Measured output power variation of the graphene added Cr^{3+}:LiSAF laser as a function of incident power with different output couplers.

4.2 Mode Locking Results

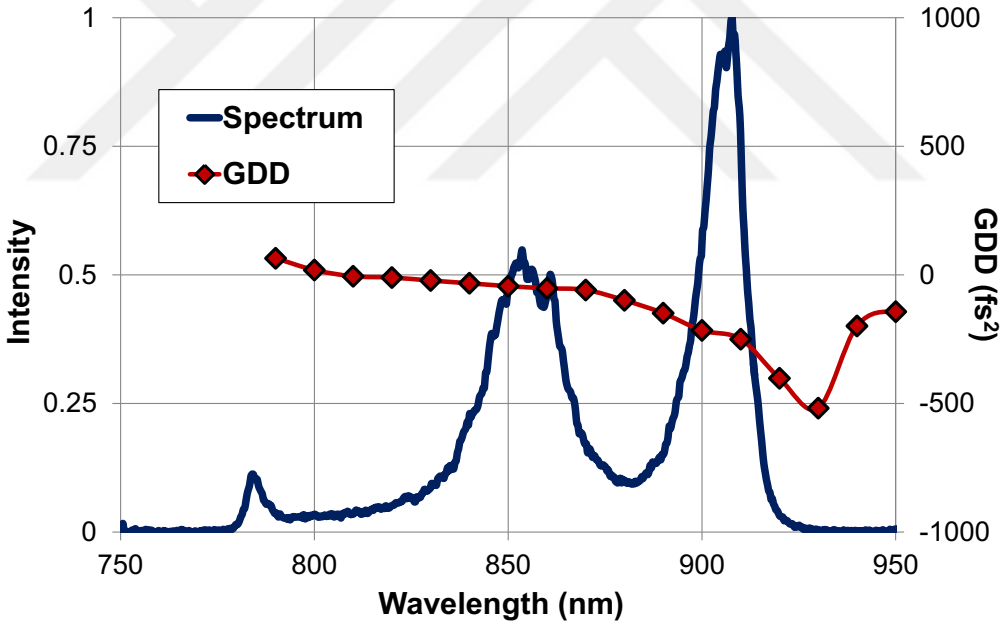

Figure 4-4: Optical spectrum of the GSA mode locked Cr^{3+}:LiSAF laser and the corresponding estimated group delay dispersion (GDD) variation as a function of wavelength (Adapted with permission from [40], The Optical Society).

After the insertion of the GSA into the resonator, femtosecond pulse generation could be readily initiated by translating the output coupler. Pulse characterization was also performed at the maximum pump power of 275 mW by using the 0.5% output coupler. Figure 4-4 shows the optical spectrum of the shortest pulses we generated and the corresponding estimated group delay dispersion (GDD) variation as a function of wavelength. Once mode locking was initiated, the output power increased from 6.2 mW to 8.5 mW due to the saturation of the GSA. Based on the measured optical spectrum, we estimated the shortest transform-limited pulse duration and the corresponding time-bandwidth product to be 17 fs and 0.41, respectively.

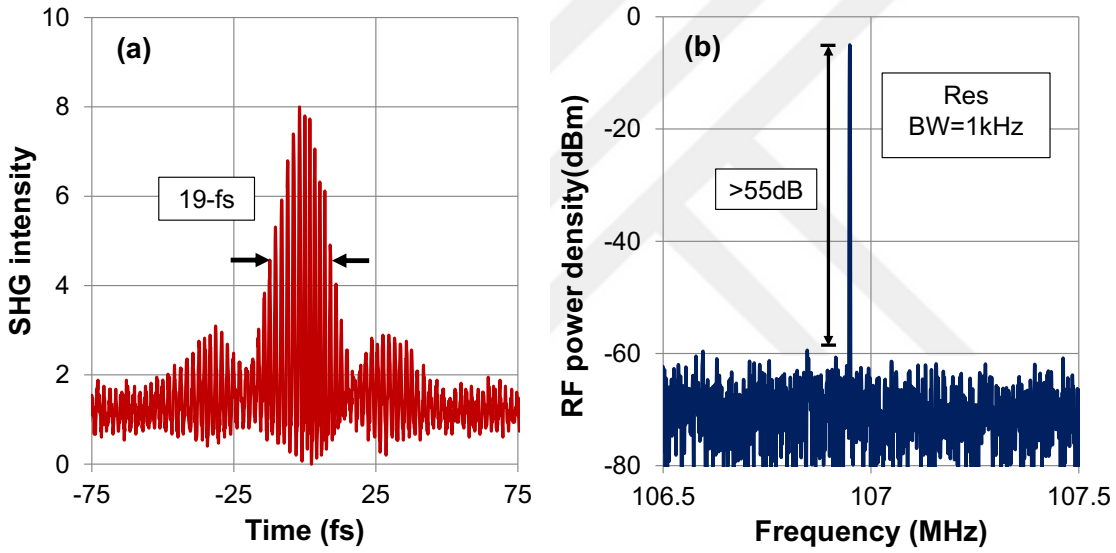

Figure 4-5: Measured **(a)** interferometric autocorrelation and **(b)** radio frequency spectrum of the generated pulses from the GSA mode-locked Cr^{3+}:LiSAF laser (Adapted with permission from [40], The Optical Society).

The experimentally measured interferometric autocorrelation trace [Figure 4-5(a)] yielded a pulse duration of 19 fs with a measured time-bandwidth product of 0.46, suggesting that the generated pulses were nearly transform limited. In the pulse measurements, dispersion compensation optics were placed in the optical path before autocorrelation setup to avoid pulse broadening effects while propagating and to

compensate broadening due to material of the output coupler mirror. Furthermore, in the RF spectrum measurements, the sidebands were at least 55 dB below the fundamental tone at the repetition rate of 107 MHz as can be seen from Fig. 4-5(b). In mode locking experiments, to balance the Kerr nonlinearities and to generate solitary pulses, dispersion management was employed by using dispersion control mirrors (DCM, M1 and M2, each with -80 ± 10 fs^2 of GDD per bounce and M5 with −40 ± 10 fs^2 of GDD per bounce) and a pair of fused silica prisms (round trip GDD~ -500 fs^2). The material GDD contributions of the gain crystal, fused silica prism material, and the infrasil substrate were +24, +40, and +40 fs^2, respectively. The net average round-trip GDD over the bandwidth was hence estimated as -50 fs^2. We further estimated the net round-trip GDD from the soliton area theorem [Eq. (2.3.2)], by using the pulse duration, intracavity pulse energy and the previously reported nonlinear refractive index of the Cr^{3+}:LiSAF gain medium (0.8×10^{-16} cm^2/W [177]). This gave a round-trip GDD of -20 fs^2. The discrepancy may be due to the fact that the actual GDD of the DCMs varies somewhat depending on the angle of incidence.

4.3 Femtosecond Tuning Results

Broad tunability of the mode-locked laser could be very useful in many applications such as multi-photon microscopy or pump-probe spectroscopy. In the experiments, we introduced an adjustable slit into the GSA-mode-locked laser between the second prism P2 and the end high reflector (M5) [Figure 4-6] to narrow the spectral bandwidth of the pulses and to investigate the tuning capability. The central wavelength of the mode-locked spectrum was adjusted by changing the position of the adjustable slit. As can be seen from the spectra displayed in Fig. 4-7, continuous femtosecond tuning could be achieved at wavelengths from 836 nm to 897 nm. Measured pulse width, spectral width, and corresponding time-bandwidth products were listed in Table 4-1. At a fixed slit width that was adjusted to give about 75-fs pulses near 875 nm, the pulse duration remained in the 75-

190 fs range between 836 and 892 nm with time-bandwidth products between 0.53 and 0.77. The pulses became broader near the long wavelength edge due to the steep GDD of the cavity optics [see Fig. 4-4]. The tuning data of Fig. 4-7 were recorded with 275 mW of input pump power.

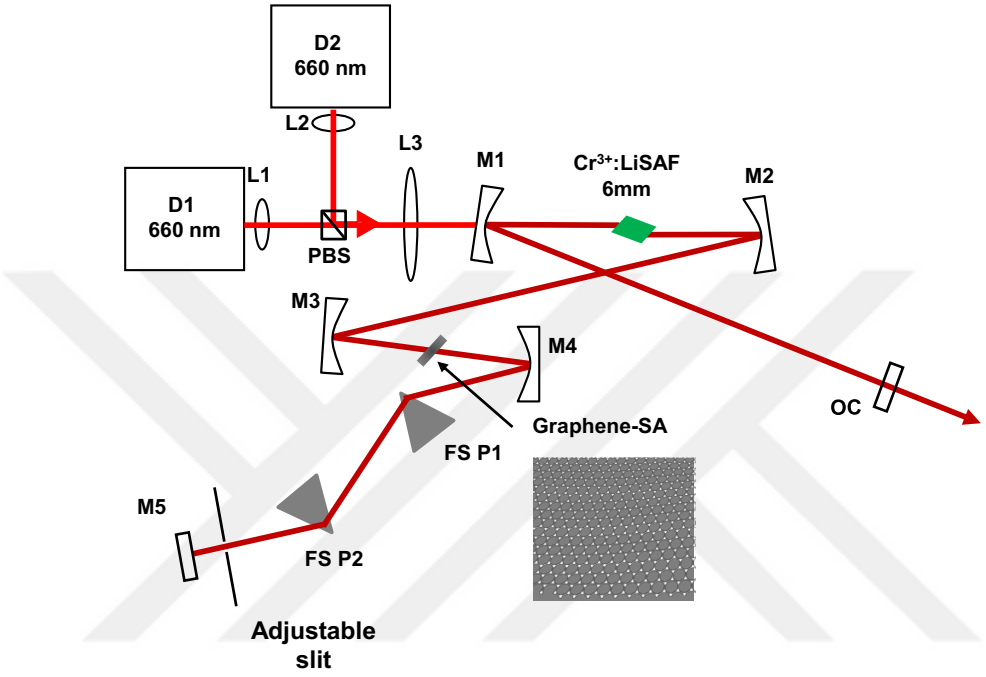

Figure 4-6: Schematic of the graphene mode-locked Cr^{3+}:LiSAF laser with an additional adjustable slit after the second prism. Femtosecond tuning experiments were performed by changing the position of the slit.

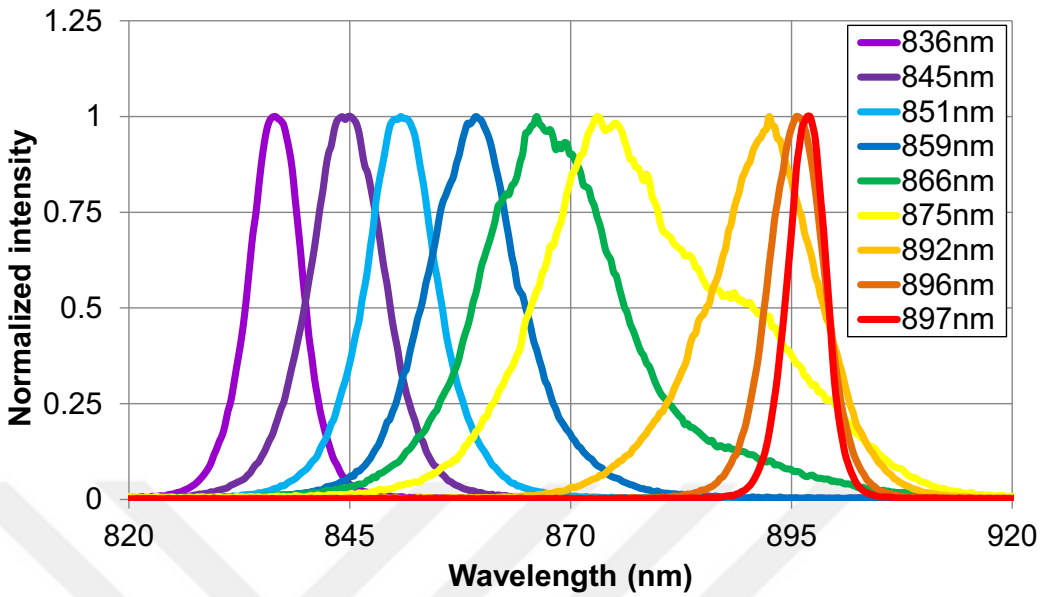

Figure 4-7: Femtosecond tuning data of the GSA mode-locked Cr^{3+}:LiSAF laser (Adapted with permission from [40], The Optical Society).

Table 4-1: Femtosecond tuning data were listed, including measured pulse width, spectral witdh, and the corresponding time-bandwdith products of the GSA mode locked Cr^{3+}:LiSAF laser

λ (nm)	836	845	851	859	866	875	892	896	897
$\Delta\lambda$(nm)	7	10	9	13	18	26	14	8	5
τ_p(fs)	186	152	141	111	80	76	116	224	338
$\Delta\lambda.\tau_p$	0.56	0.64	0.53	0.59	0.58	0.77	0.61	0.67	0.63

4.4 Pulsed Operation Initiation Test

To verify that mode locking was indeed initiated by the fast-saturable absorber action in graphene, we checked the initiation mechanism of mode locking across the full cavity stability range. In particular, we varied the position of the curved mirror M2 at 10-μm

intervals across the full stability range and at each point, we checked whether or not mode locking could be initiated by translating the output coupler. In the control experiment, the infrasil substrate was placed in between the focusing mirrors and the mode locking test was performed. Next, infrasil substrate with GSA was replaced with a bare infrasil substrate and the same test was repeated.

Figures 4-8(a) and (b) show the measured output power as a function of the M2 position for bare infrasil substrate and infrasil substrate with GSA. Figures 4-8(c) and (d) show at which points within the stability range mode locking could be initiated. The values of 1, 0.5 and 0 indicate M2 positions with stable mode locking, only flashing of mode-locked operation, and no mode locking, respectively. Note that with the bare infrasil substrate, mode locking could be initiated at far fewer points [see Fig. 4-8(c)]. In this case, the initiation mechanism was Kerr-lens mode locking (KLM) that requires critical cavity alignment. With the GSA on infrasil [Figure 4-8(d)], we were able to obtain stable mode-locked operation over the full stability range except at the edges, indicating that the initiation mechanism had no sensitivity to critical cavity alignment, and clearly verifying that mode locking was initiated by the fast saturable absorber action in the GSA.

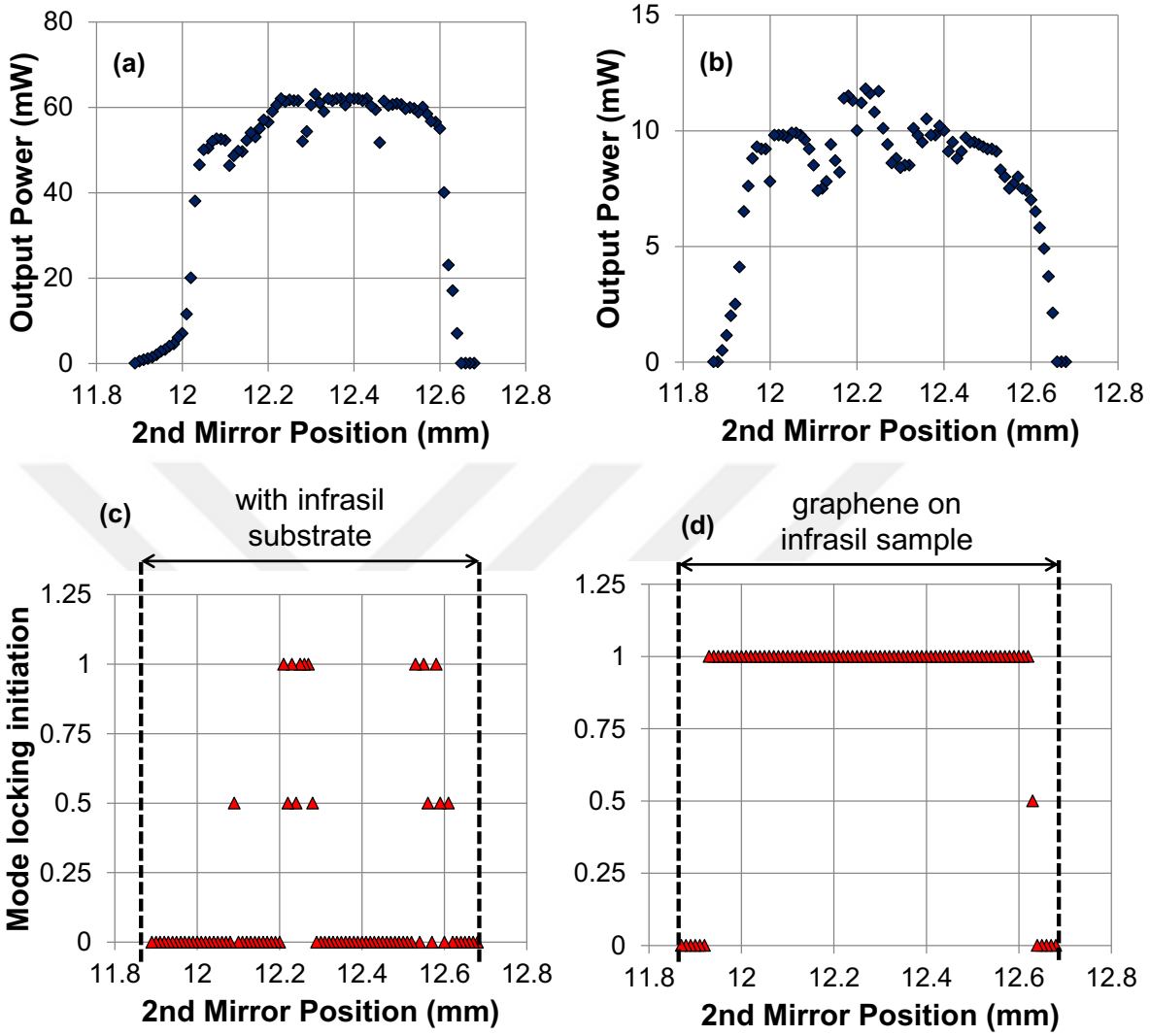

Figure 4-8: Measured output power of the Cr^{3+}:LiSAF laser as a function of the M2 position with **(a)** a bare infrasil substrate **(b)** an infrasil substrate with graphene. Mode locking initiation maps of the resonator with **(c)** a bare infrasil substrate and **(d)** an infrasil substrate with graphene (Adapted with permission from [40], The Optical Society).

Also note that, the shortest pulse data displayed in Figs. 4-4, 4-5(a), and 4-5(b) were recorded at the M2 location (12.48 mm) where only the GSA took part in the initiation of femtosecond pulse train without any KLM effect. Also note that as the output power data of Fig. 4-8(b) were measured, transients caused by the moving output coupler led to

damage on the GSA at several M2 positions. The position of the GSA was then slightly changed, leading to the power fluctuation seen in Fig. 4-8(b). However, at the M2 position where the shortest pulse data were recorded, no damage was observed on the GSA up to the maximum fluence level of 1264 μJ/cm^2, estimated by assuming a mode-locked output power of 8.5 mW and by using the other relevant parameters of the resonator.

In conclusion, we demonstrated, what is to our knowledge, the shortest pulses that ever generated, directly from a graphene mode-locked solid-state laser. The graphene mode-locked Cr^{3+}:LiSAF gain medium employed in the experiments, was operated in a low-threshold resonator configuration. Stable and uninterrupted 19-fs pulses were directly generated at 850 nm with only 275 mW of pump power. The repetition rate was around 107 MHz, corresponding to a pulse energy and peak power of 79 pJ and 4.2 kW, respectively. Once mode locking was initiated with the GSA, femtosecond pulses could be obtained for hours without any Q-switching instabilities. In addition, the femtosecond output of the laser could be tuned from 836 nm to 897 nm. Finally, we used a definitive experimental test to clearly identify the initiation mechanism for mode locking and experimentally demonstrated that the femtosecond pulse train was initiated solely by the fast saturable absorber action in graphene.

Chapter 5

5 KERR-LENS MODE-LOCKED 2.3 µm Tm^{3+}:YLF LASER AS A NEW SOURCE OF FEMTOSECOND PULSES

In this Chapter, Kerr-lens mode locking results that we obtained from a Tm^{3+}:YLF laser operating near 2.3 µm will be presented. Femtosecond pulses were generated from the Tm^{3+}:YLF laser for the first time to our knowledge. A brief introduction of cw Ti^{3+}:sapphire laser was presented in the first part of Chapter 4. In the second part cw Tm^{3+}:YLF laser was introduced. After the description of mode-locked Tm^{3+}:YLF laser setup in the next part, mode locking results are presented. In the final part, a detailed soliton area theorem analysis will be described.

5.1 Ti^{3+}:sapphire Laser

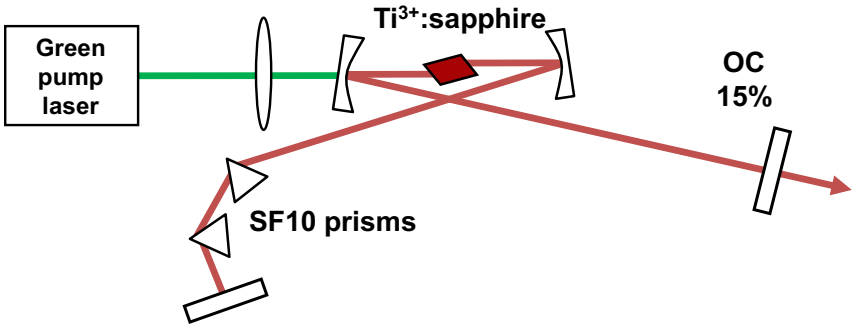

Figure 5-1: Schematic of the cw Ti^{3+}:sapphire laser that is used as a pump source. Two SF10 prisms were included to obtain tunability with narrow linewidth.

To obtain efficient excitation for Tm^{3+}:YLF, we first set up a tunable Ti^{3+}:sapphire laser, pumping with a commercial 5-W laser (OPUS, MPC6000, Laser Quantum) which operates at 532 nm. A standard x-fold laser was built with three high reflector and one output coupler mirror (OC 15%) as shown in Fig. 5-1. The Brewster-cut 10-mm-long Ti^{3+}:sapphire gain medium used in the experiments absorbed 92% of the pump beam at the pumping wavelength of 532 nm. A pair of SF10 prisms was placed in cascaded arrangement to adjust operation wavelength of the laser. Inclusion of the prism pair provided narrow spectral linewidth as well.

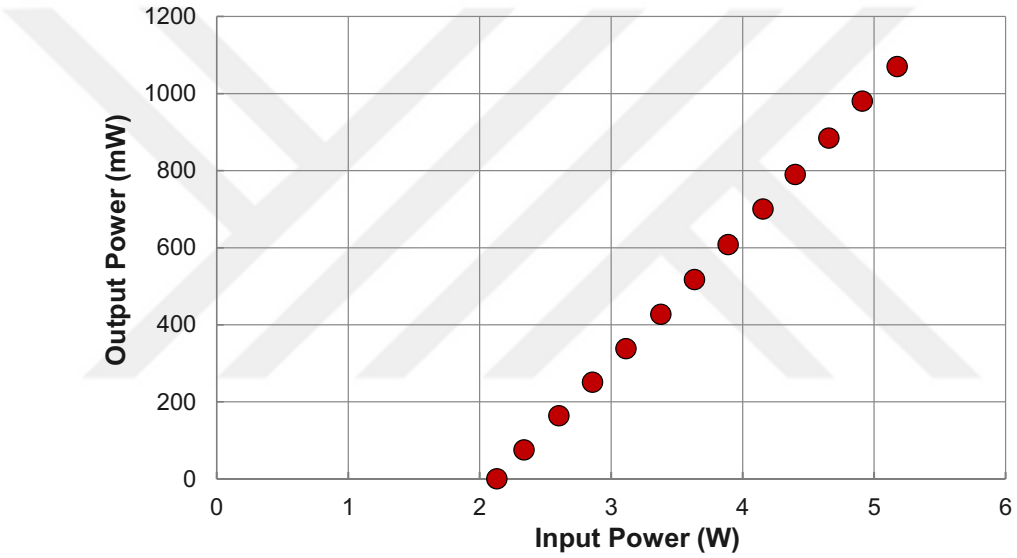

Figure 5-2: Power performance of the Ti^{3+}:sapphire laser by using 15% output coupler at 780 nm.

Continuous wave Ti^{3+}:sapphire laser was optimized to be a suitable pump source for the Tm^{3+}:YLF laser. Continuous wave power performance of the Ti^{3+}:sapphire laser is shown in Fig. 5-2. As high as 1050 mW of output power could be obtained from the Ti^{3+}:sapphire laser at 5.2 W of input power.

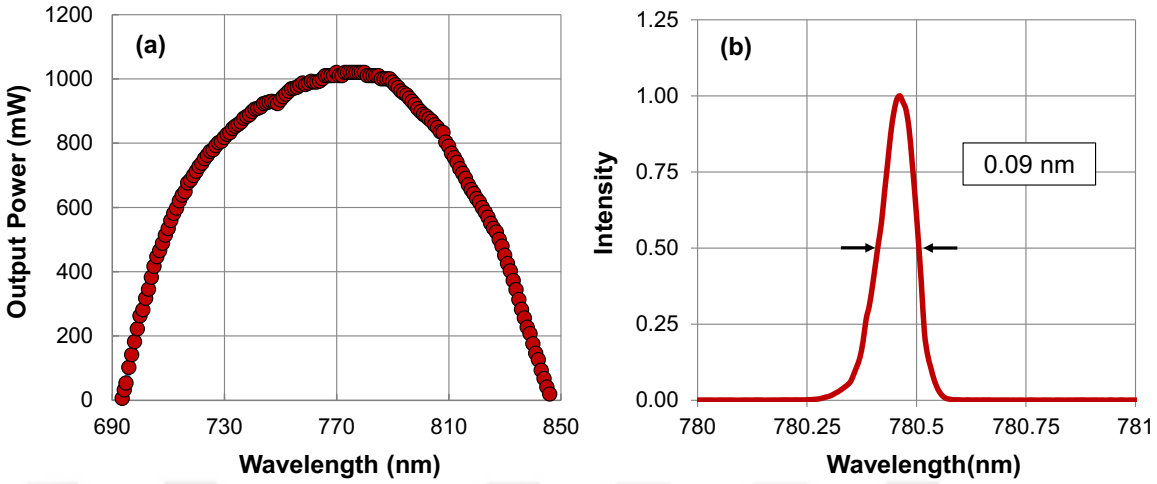

Figure 5-3: (a) Tuning data and **(b)** measured linewidth of the cw Ti^{3+}:sapphire laser.

After the addition of the prism pair, operation wavelength of the Ti^{3+}:sapphire laser can be tuned from near 690 nm to 850 nm as shown in Fig. 5-3(a). At the maximum absorption wavelength of the Tm^{3+}:YLF gain medium of 780 nm, the Ti^{3+}:sapphire laser produced as high as 912 mW of output power. The linewidth was measured to be 0.09 nm (Measured with Anritsu Spectrum Analyzer, Resolution=0.07 nm, Video Bandwidth=100 Hz, Span=2 nm). Over the tuning range the linewidth remains nearly constant [Figure 5-3(b)].

5.2 Continuous-wave Operation of the Tm^{3+}:YLF Laser

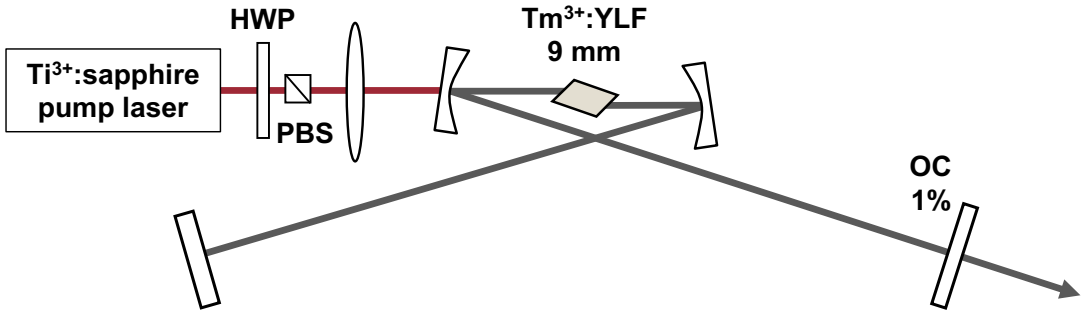

Figure 5-4: Schematic of the x-cavity Tm^{3+}:YLF laser setup pumped by the cw Ti^{3+}:sapphire laser operating at 780 nm.

A schematic representation of the Ti^{3+}:sapphire-pumped, cw Tm^{3+}:YLF laser is shown in Fig. 5-4. Before Tm^{3+}:YLF laser, a half-wave plate and a polarizing beam splitter were placed to adjust the input power of the laser, without causing any thermal effects in Ti^{3+}:sapphire laser. The Ti^{3+}:sapphire pump beam was focused with a convex lens (L2, f=75 mm) inside the Brewster-cut, 9-mm-long Tm^{3+}:YLF crystal, which had a Tm^{3+} ion concentration of 1.5 at. %, and which absorbed 78% of the pump beam at 780 nm. The x-cavity Tm^{3+}:YLF laser resonator was constructed with two curved mirrors, one high reflector and an output coupler (1% OC) as shown in Fig. 5-4. The high reflector and output coupler arm lengths were 62.5 cm and 67 cm, respectively. The reflectivity edge of all high reflectors was above 2.1 μm to avoid the lasing of the $^3F_4 \rightarrow {}^3H_6$ transition near 2 μm.

Power performance of the Tm^{3+}:YLF laser was shown in Fig. 5-5(a). The incident threshold pump power was measured to be 114 mW. At the full incident pump power of 912 mW, the Tm^{3+}:YLF cavity generated as high as 107 mW output power at 2.3 μm with a slope efficiency of 13% [see Fig. 5-5(a)]. Measured output spectrum was centered near 2.3μm and had a spectral width of 1 nm [Figure 5-5(b)].

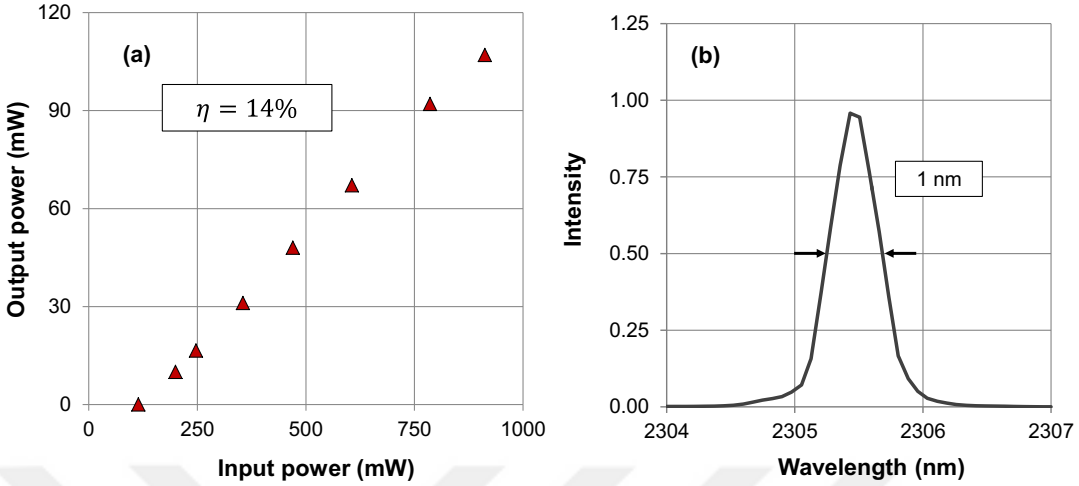

Figure 5-5: (a) Continuous wave output power variation of the Tm^{3+}:YLF laser as a function of input power. **(b)** Optical spectrum of the cw-Tm^{3+}:YLF laser.

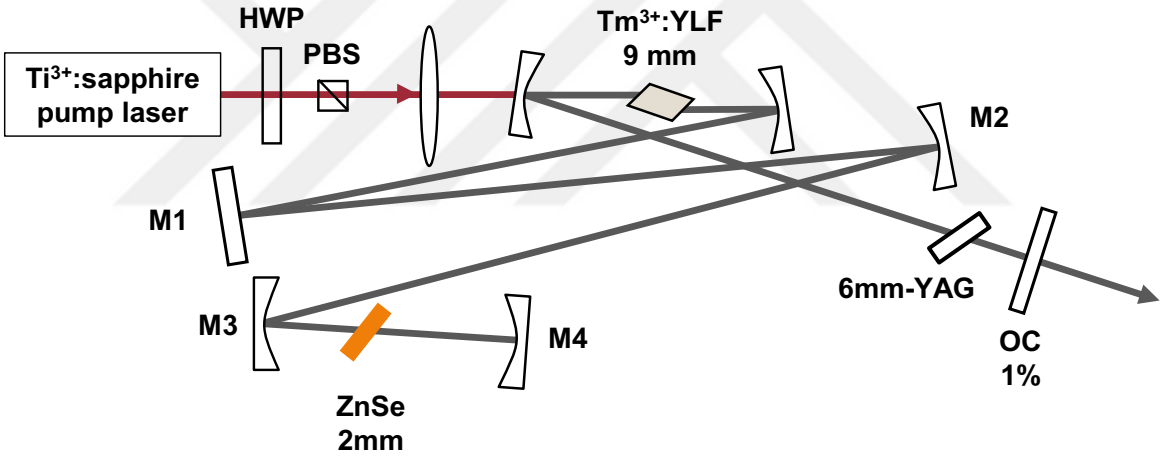

Figure 5-6: Schematic of the cw Ti^{3+}:sapphire pumped Tm^{3+}:YLF laser operating at 2.3 µm. Extended Tm^{3+}:YLF laser generated femtosecond pulses with the inclusion of ZnSe and YAG substrates (Adapted with permission from [45], The Optical Society).

In order to increase the available intracavity pulse energies during Kerr-lens mode locking, the cavity length was later extended [Figure 5-6]. In particular, the end high reflector mirror (M1) was tilted, and the curved mirror M2 (R=1000 mm) was placed at a

distance of 1 m from M1 so as to transform the waist from the location of M1 to the location of M3 (which was at a distance of 1 m from M2) in a q-preserving arrangement [178]. The cavity was completed by retroreflecting the beam from the curved-end high reflector M4. The total length of the cavity came to 3.61 m, corresponding to a pulse repetition frequency of 41.5 MHz. A photograph of the cw Ti^{3+}:sapphire pumped Tm^{3+}:YLF laser was shown in Fig. 5-7. An undoped polycrystalline ZnSe substrate with a length of 2 mm was further located at Brewster's incidence near the focus between M3 and M4 in order to provide enhanced nonlinear phase modulation. Based on standard ABCD analysis of the cavity, the beam waists inside the Tm^{3+}:YLF gain medium and on the ZnSe substrate were estimated to be 41 μm and 76 μm, respectively, during mode-locked operation. Furthermore, because the dispersion contributions from the YLF and ZnSe media are of opposite signs, an additional 6-mm-long YAG substrate was inserted in the output coupler arm to provide negative group delay dispersion (GDD) and to aid in the formation of solitary pulses. For the extended cavity configuration, the output power decreased from 107 mW to 35 mW at the pump power of 880 mW [Figure 5-8]. The corresponding slope efficiency was 5%. By using the threshold pump power data taken at different output coupling levels, the round-trip cavity loss of the short x-cavity was estimated to be 0.3%. Furthermore, the incident threshold pump power increased from 114 mW to 178 mW after the cavity extension, giving an estimated loss of 0.7% due to the additional components (M2, M3, M4, YAG substrate, and ZnSe substrate). The total round-trip loss of the composite cavity became approximately 1%.

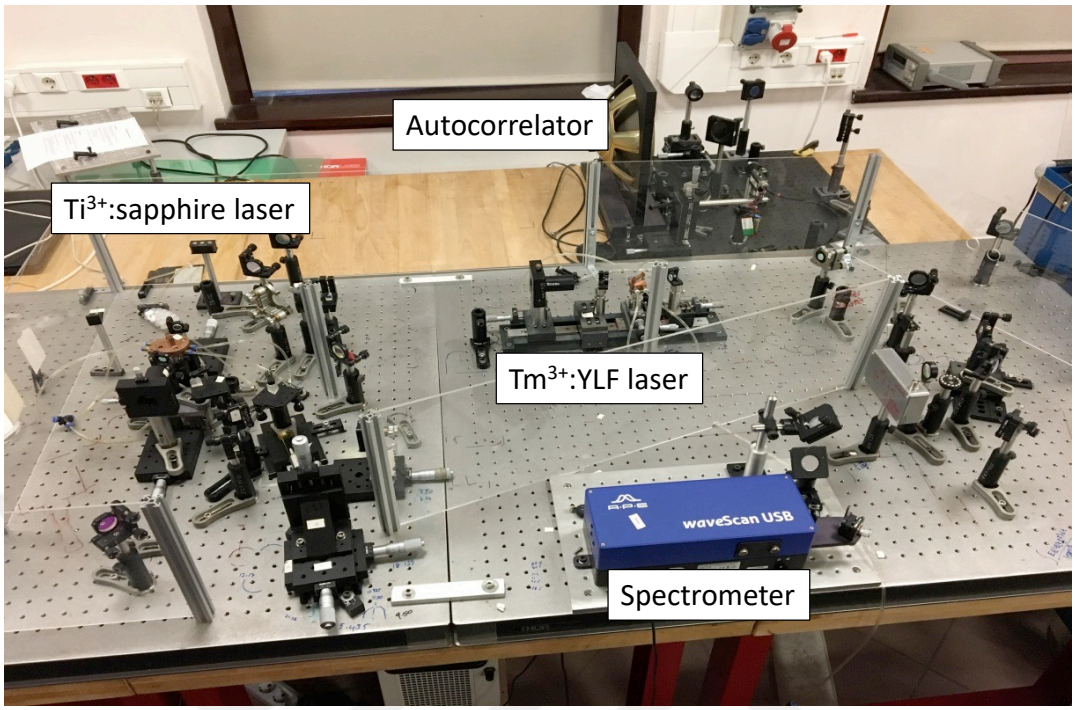

Figure 5-7: A Photograph of the cw Ti^{3+}:sapphire pumped Tm^{3+}:YLF laser. The Spectrometer and the autocorrelation setups are also shown.

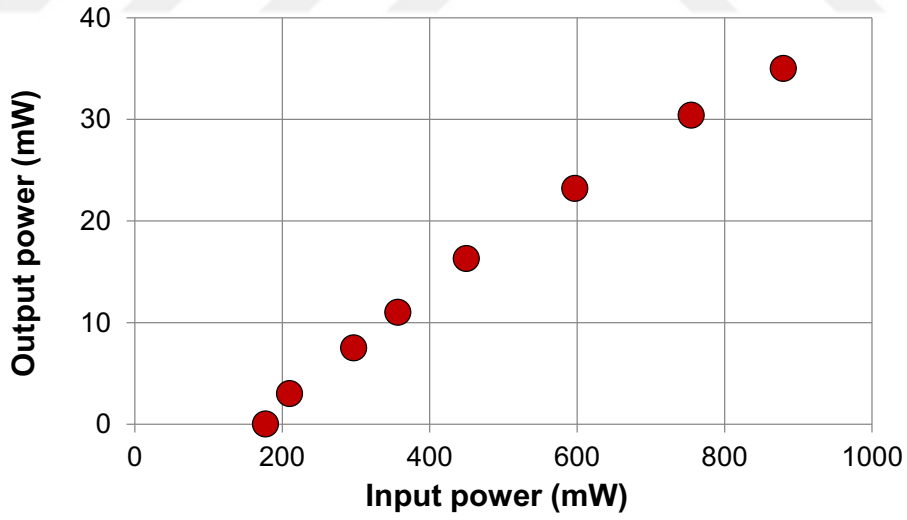

Figure 5-8: Measured variation of the output power as a function of input power for the extended cavity Tm^{3+}:YLF laser operating at 2.3 µm.

5.3 Mode-Locked Operation Results

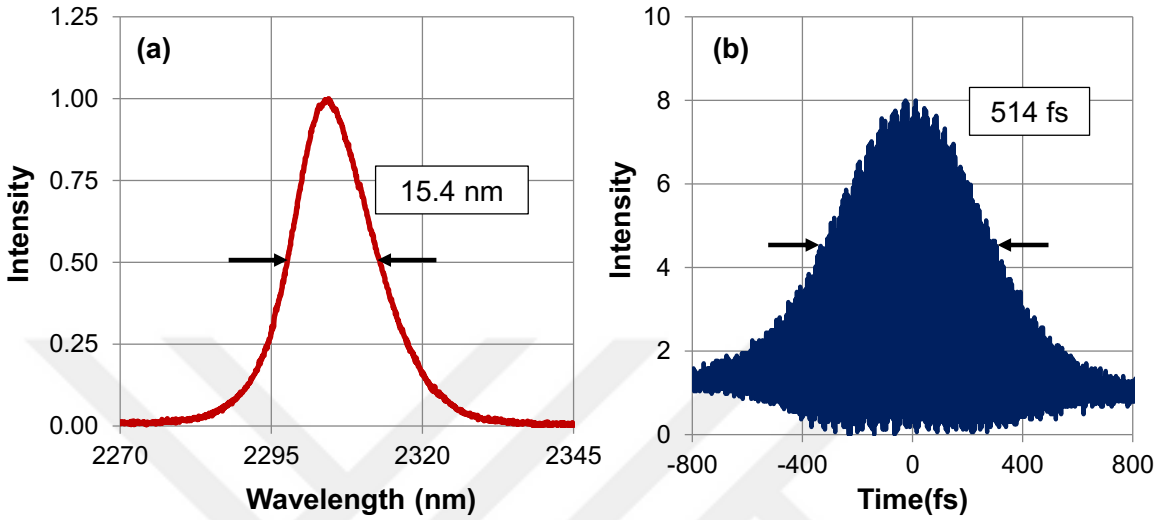

Figure 5-9: Measured **(a)** optical spectrum and **(b)** interferometric autocorrelation trace of the generated pulses from the KLM Tm^{3+}:YLF laser operating at 2.3 µm (Adapted with permission from [45], The Optical Society).

Once the focusing inside the Tm^{3+}:YLF and ZnSe media was carefully optimized, KLM operation of the Tm^{3+}:YLF laser could be achieved at 2303 nm by translating the output coupler. Figures 5-9(a) and (b) show the optical spectrum and interferometric autocorrelation trace of the mode-locked output. The measured spectral width of the pulses was 15.4 nm. Note that, it was possible to lock approximately half of the available tuning range [134]. We foresee that a wider lasing bandwidth will be available for mode locking if an output coupler with a lower transmission is used. Figure 5-9(b) shows the experimentally measured interferometric autocorrelation trace of the mode-locked pulses. The interferometric autocorrelation was experimentally measured by using two-photon absorption inside a germanium detector with a rise time of 3.5 ns. By assuming a $sech^2$ intensity profile, the duration (FWHM) of the pulses was measured to be 514 fs. The

corresponding time-bandwidth product came to 0.44, indicating that the generated pulses were slightly chirped.

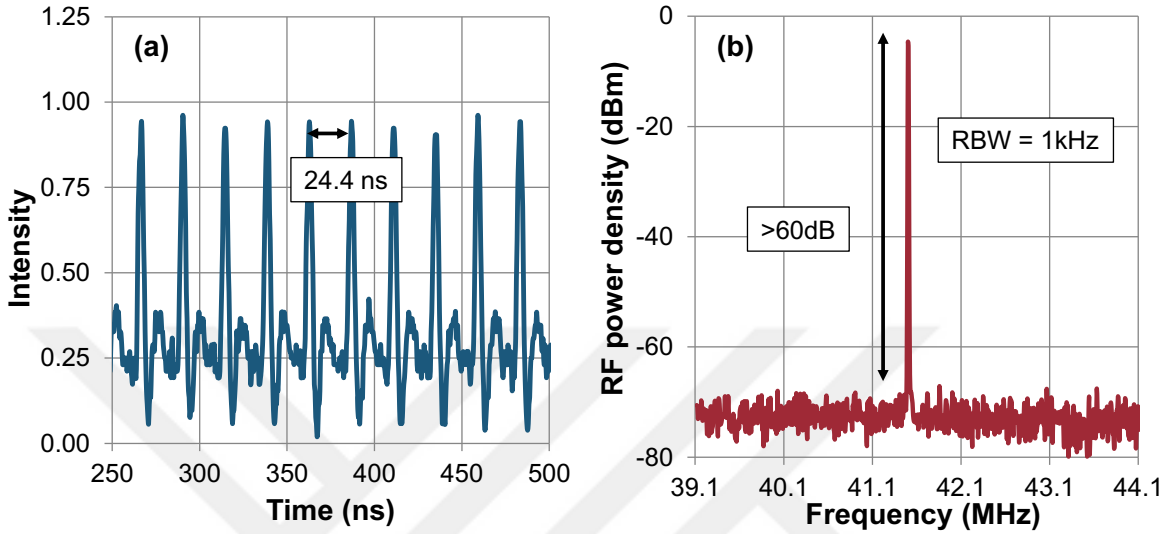

Figure 5-10: Measured **(a)** pulse train and **(b)** RF specturm of the generated pulses from the KLM Tm^{3+}:YLF laser operating near 2.3 µm (Adapted with permission from [45], The Optical Society).

Figure 5-10(a) further shows the pulse train of the mode-locked Tm^{3+}:YLF laser at the nanosecond scale. The pulse train was measured by using a high-speed InGaAs photodetector with responsivity up to 2.6 µm. In the mode-locking experiments, we did not observe any Q-switching or relaxation oscillations at longer time scales. This indicates that pure cw mode-locked operation was obtained in the experiments. As can be seen from the radio frequency (RF) spectrum displayed in Fig. 5-10(b), the fundamental tone at 41.5 MHz was more than 60 dB above the noise floor. The RF spectrum was recorded at a resolution bandwidth of 1 kHz.

5.4 Soliton Area Theorem Analysis

Achieving KLM operation in the Tm^{3+}:YLF gain medium at 2.3 µm is challenging due to several factors. First, because the Tm^{3+} ion concentration is kept at 1.5 at. % to prevent

nonradiative quenching, this requires relatively long samples to obtain sufficient pump absorption at 780 nm. In our case, a 9-mm-long sample was used to obtain 78% absorption. This leads to an excessive negative GDD (−1377 fs^2 per round trip at 2.3 μm), which is difficult to balance due to the relatively weak Kerr nonlinearity of the medium (n_2 =1.72×10^{-20} m^2/W for YLF [179]). Extension of the cavity and inclusion of the ZnSe substrate address this issue by providing higher intracavity pulse energies and enhanced Kerr nonlinearity. To analyze the operating point of our mode-locked Tm^{3+}:YLF laser, we used the soliton area theorem [171, 180], where the pulse duration (τ_p), intracavity energy (W), Kerr nonlinearity coefficient (δ), and round-trip GDD (D) are related through

$$W = 1.76\frac{4|D|}{\delta_{eff}\tau_p}. \tag{5.4.1}$$

In our case, the Kerr nonlinearity arises from both the ZnSe and Tm^{3+}:YLF media. Hence, we estimated the effective nonlinearity coefficient (δ_{eff}) by using

$$\delta_{eff} = \frac{2\pi}{\lambda}\left[\left(\frac{2n_2L}{A_{eff}}\right)_{ZnSe} + \left(\frac{2n_2L}{A_{eff}}\right)_{Tm:YLF}\right]. \tag{5.4.2}$$

In Eq. (5.4.2), n_2, L, and A_{eff} are the respective nonlinear refractive index, length, and effective beam cross-sectional area for each medium. In addition, A_{eff} is estimated from

$$A_{eff} = \pi w_{rms}^2 \tag{5.4.3}$$

where w_{rms} is the root-mean-squared spot size inside each medium. The nonlinearity of the YAG substrate was neglected since it was placed in the output arm of the resonator where the intracavity beam was not focused. Based on the ABCD analysis of the resonator, w_{rms} was estimated to be 52 μm and 76 μm for the Tm^{3+}:YLF crystal and ZnSe substrate, respectively. By using the known nonlinear refractive index of the YLF (n_2=1.72 × 10^{-20}

m^2/W [179]) and ZnSe (n_2=120 × 10^{-20} m^2/W [181]) media, the Kerr nonlinearity coefficients were estimated to be $\delta_{Tm:YLF}=9.98\times10^{-8}$ and $\delta_{ZnSe}=7.79\times10^{-7}$. Note that the nonlinearity contribution coming from the ZnSe substrate is more than 7.5 times larger than that from the YLF crystal. By using Eq. (5.4.1) and the operating parameters of the mode-locked laser (W=34.7 nJ, τ_p=514 fs), the round-trip net GDD at the soliton operating point was determined as −2225 fs^2. By using the known GDD values of the intracavity components (236.5 fs^2/mm for ZnSe [182], −76.5 fs^2/mm for YLF [183], −123 fs^2/mm for YAG [184], and −10.1 fs^2/mm for air [185] at 2.3 μm), the total round-trip GDD of the resonator came to −2135 fs^2, in good agreement with the value estimated from the soliton area theorem [Eq. (2.3.2)].

We report what is to our knowledge a new source of femtosecond pulses in the mid-infrared, based on a Kerr-lens mode-locked (KLM) Tm^{3+}:YLF laser at 2303 nm. An undoped ZnSe substrate was included in the resonator to provide enhanced nonlinear phase modulation during KLM operation. The Tm^{3+}:YLF laser was end-pumped with a continuous-wave Ti^{3+}:sapphire laser at 780 nm. With 880 mW of pump power, we generated 514-fs pulses at a pulse repetition rate of 41.5 MHz with an average power of 14.4 mW. The spectral width (full width at half-maximum) was measured as 15.4 nm, giving a time-bandwidth product of 0.44. We foresee that the wide availability of this gain medium, as well as the straightforward pumping scheme near 800 nm, will make 2.3-μm, mode-locked Tm^{3+}:YLF lasers versatile sources of ultrashort pulses in the mid-infrared.

Chapter 6

6 GRAPHENE MODE-LOCKED Tm^{3+}:YLF LASERS OPERATING NEAR 2.3 µm

Chapter 6 presents mode locking experiments in which we employed a monolayer graphene as a saturable absorber to generate ultrashort pulses from a Tm^{3+}:YLF laser operating near 2.3 µm for the first time to our knowledge. This study shows the mode-locking performance of graphene saturable absorbers in 2.3 µm Tm^{3+}:YLF lasers. In the first part of this chapter, experimental setup of the Tm^{3+}:YLF laser was introduced. This will be followed by mode locking results and soliton area theorem analysis.

6.1 Experimental setup

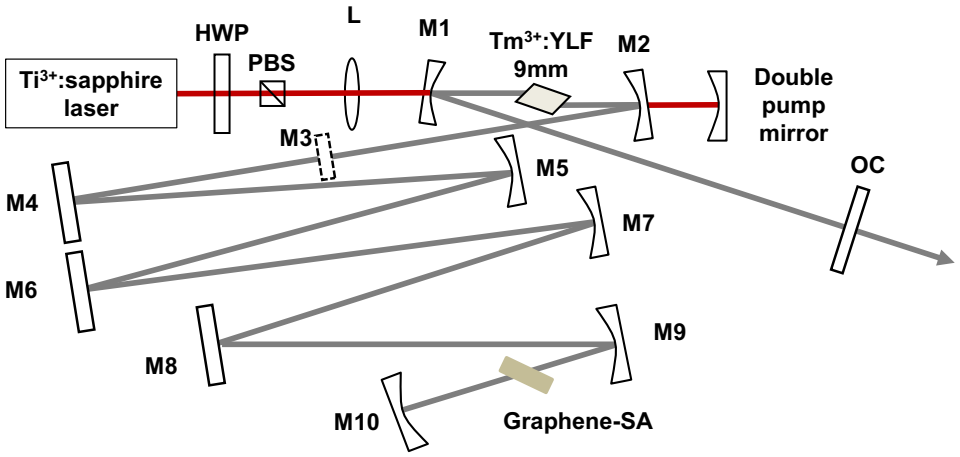

Figure 6-1: Schematic of the graphene mode-locked Tm^{3+}:YLF laser operating near 2.3 µm. The Tm^{3+}:YLF laser was double pumped to overcome unsaturable losses of the graphene saturable absorber.

A schematic representation of graphene mode-locked Tm^{3+}:YLF laser operating near 2.3 μm is shown in Fig. 6-1. A home-built, tunable, and narrow line Ti^{3+}:sapphire laser was used as pump source. A detailed description of the Ti^{3+}:sapphire laser was stated in Chapter 5. We first started with an x-cavity Tm^{3+}:YLF, as described in the second part of Chapter 5, consisting of two curved mirrors (M1-M2, R=100mm), a high reflector (M3), and an output coupler (OC). In the mode-locking experiments, we used 1% output coupler to remain near the optimum output coupling of the resonator.

After x-cavity characterization experiments, we extended the high reflector arm with two curved mirrors (M5, M7), having 2 m of radius of curvature (ROC). With the addition of these curved mirrors, the cavity length was extended up to 8 m by using extra high reflectors (M6, M8) as shown in Fig. 6-1. The total length of the high reflector arm became nearly 8 m. The position of the extension mirror positions was optimized by maximizing the output power of the Tm^{3+}:YLF laser. The optimum distance that provided the maximum output power was near 186 cm for the additional curved mirrors (ROC=2m). With the addition of these curved mirrors, the beam parameters inside the crystal remained nearly the same. After the addition of the extension mirrors (M4-M8), to obtain an additional waist on the graphene sample, two curved mirrors (R=75mm, M9 and M10) were placed. The distance between M9 and M10 mirrors was 10.5 cm (f-2f arrangement). The graphene sample was placed near the focus of M9 mirror at Brewster's incidence to reduce the reflection losses. The monolayer graphene sample was prepared on an infrasil substrate by our collaborators in Korea (the research group of Fabian Rotermund). Based on the ABCD matrix analysis, the beamwaists inside the Tm^{3+}:YLF gain medium and on the graphene sample were estimated to be 44 μm and 98 μm, respectively.

An additional double pumping mirror was added after the second curved mirror (M2) to utilize the unused power. Single and double pumped power performance of the x-cavity Tm^{3+}:YLF laser were investigated [Figures 6-2(a) and (b)]. In the case of single

pumping, as high as 82 mW of output power could be obtained with 872 mW of pump power. The pump threshold was measured to be 103 mW. With 872 mW of incident power, the double pumped Tm^{3+}:YLF resonator produced 142 mW of output power. In the case double pumping, measured threshold incident pump power was 83 mW.

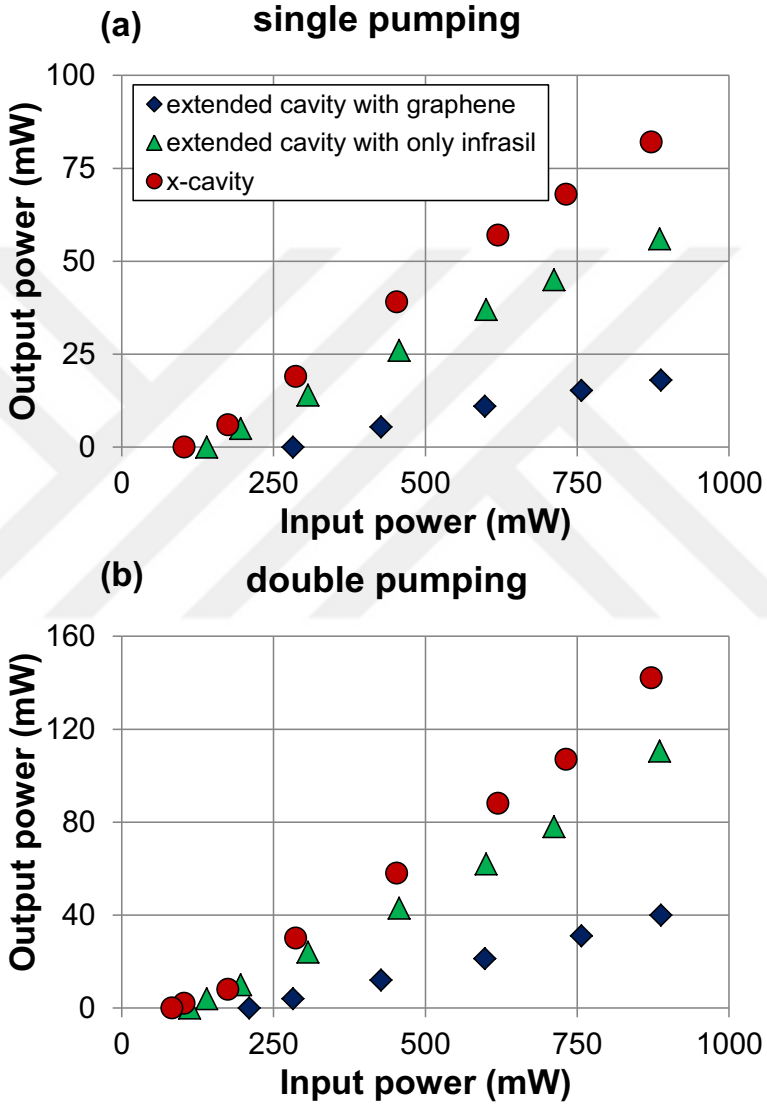

Figure 6-2: Measured output power variation of the cw Tm^{3+}:YLF laser for the cases of **(a)** single and **(b)** double pumping.

Power performance measurements were made to estimate the loss of the graphene sample. Note that, graphene was transferred in the shape of a square on to the infrasil substrate (see Fig. 1-7, note that outside the blue dots there is no graphene). In the double pumping configuration, as high as 110 mW of output power could be obtained from the extended cavity with infrasil only. Based on the Findlay-Clay analysis [175], the additional loss of the extension was estimated to be 0.3%. We then measured the power performance of the composite cavity (including all extensions and graphene sample) as shown in Fig. 6-2 (blue markers). As can be seen from Fig. 6-2, the slope efficiency decreased from 14% (8%) (extended cavity including infrasil) to 6% (3%), in the case of double (single) pumping. Based on the threshold analysis [175], the insertion loss of graphene and extension mirrors was estimated to be 4%. The estimated loss of the graphene on infrasil (Korean sample) was less than expected (>4.6%).

6.2 Mode locking results

After cw characterization experiments, we first added two additional curved mirrors (R=100 mm) to the x-cavity Tm^{3+}:YLF laser to obtain an additional waist to place the graphene sample. After the addition of the graphene sample in between the curved mirrors, mode-locked operation could be readily initiated by translating the output coupler.

Figure 6-3 shows the optical spectrum of the generated pulses with the short x-cavity Tm^{3+}:YLF laser. However, depending on the position of the graphene sample, Q-switching instabilities were also observed in the pulse train measurements at longer time scales. To increase the intracavity pulse energy with the available pump power, we then extended the laser resonator as mentioned in the previous section.

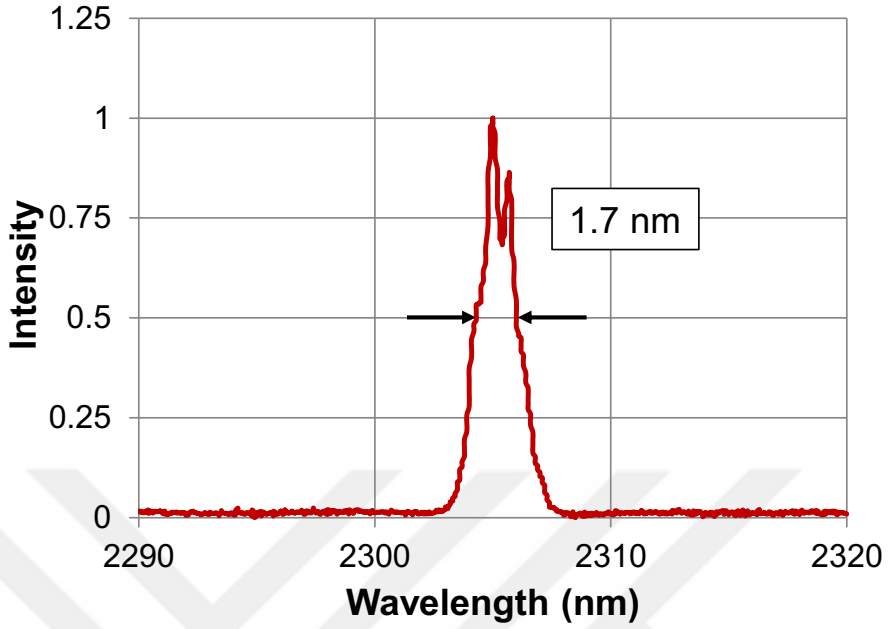

Figure 6-3: Measured optical spectrum of the graphene mode-locked short-cavity Tm^{3+}:YLF laser.

Once the graphene sample was placed inside the extended cavity, the double pumped Tm^{3+}:YLF laser operating near 2.3 µm could be mode locked by translating the output coupler. Above 665 mW of input power in the case of double pumping, mode locking could be initiated and sustained without any Q-switching instabilities. With 888 mW of pump power, 42 mW of mode locked output power was obtained. Figures 6-4(a) and (b) show the measured optical spectrum and interferometric autocorrelation trace of the graphene mode locked Tm^{+3}:YLF laser. The spectral width and pulse duration of the output pulses were measured to be 6.5 nm and 1 ps, respectively, with a corresponding time-bandwidth product of 0.389. This indicates that the pulses were nearly transform-limited with a $sech^2$ pulse shape. The optical spectrum was recorded with a scanning mid-infrared spectrometer (APE). The interferometric autocorrelation was measured by using two-photon absorption inside a germanium detector with a rise time of 3.5 ns.

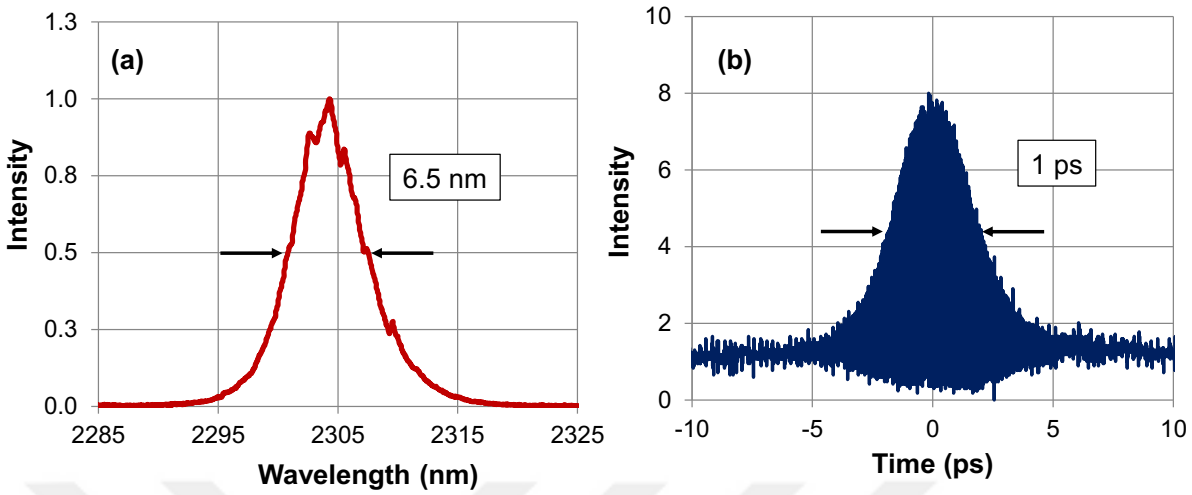

Figure 6-4: Measured **(a)** optical spectrum and **(b)** interferometric autocorrelation trace of the generated pulses from the graphene mode-locked Tm^{3+}:YLF laser at 2305 nm.

Figures 6-5(a) and (b) show the radio frequency (RF) spectrum and pulse train of the generated pulses from the graphene mode-locked Tm^{3+}:YLF laser. The RF spectrum showed that, the fundamental tone of the resonator at the repetition frequency of 17.2 MHz was at least 70 dB above the noise floor. The pulse train was measured with a fast InGaAs detector. At longer timescales, no Q-switching instabilities were observed. Data shown in Figs. 6-4(a), 6-4(b), 6-5(a) and 6-5(b) were recorded at the pump power of 888 mW. The corresponding pulse energy and peak power were 2.44 nJ and 2.44 kW, respectively. We further estimated the incident fluence on the graphene saturable absorber as 809 μJ/cm^2, indicating that the sample was fully saturated [148].

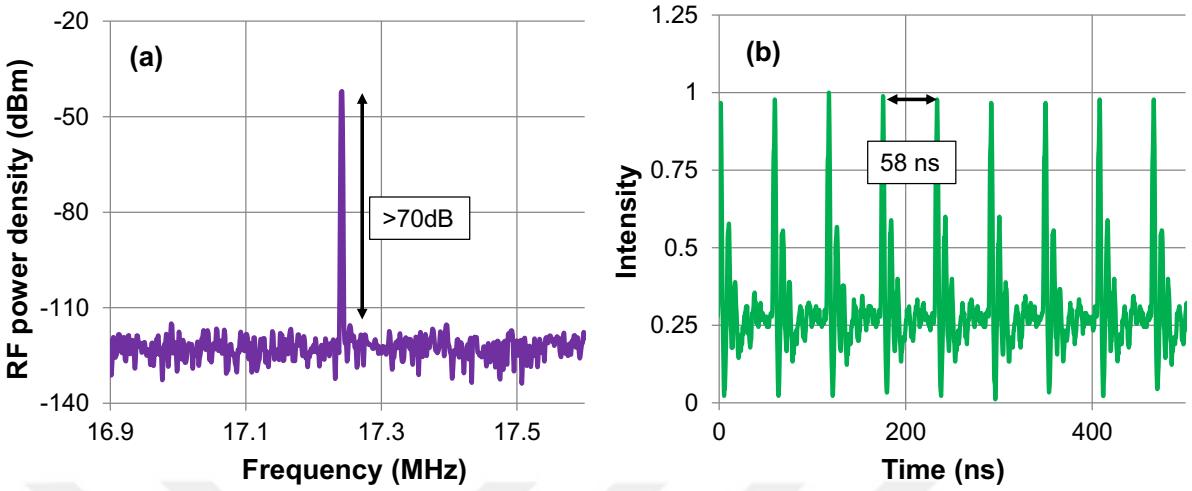

Figure 6-5: Measured **(a)** radio frequency and **(b)** pulse train of the generated pulses.

To estimate the net dispersion inside the resonator, we used both material dispersion data and the soliton area theorem [Eq. (2.3.2)]. As in the case of KLM Tm^{3+}:YLF laser, we estimated the effective nonlinearity (δ_{eff}) [Eq. (5.4.2)] by using nonlinear refractive indices of Tm^{3+}:YLF (n_2=1.72×10^{-20} m^2/W [179]) and infrasil substrate (n_2=2.74 × 10^{-20} m^2/W [186]) to be δ_{eff}=1.02×10^{-7} W^{-1}. Based on the soliton area theorem and using δ_{eff}, roundtrip group delay dispersion (GDD) was estimated as -3522 fs^2. We further estimated the roundtrip GDD from the material dispersion values (-76.5 fs^2/mm for YLF [183], -10.1 fs^2/mm for air [185], and -218 fs^2/mm for infrasil at 2.3 μm) to be –2085 fs^2. This discrepancy may be due to an additional dispersion contribution coming from the extension mirrors.

In conclusion, we described a graphene mode-locked Tm^{3+}:YLF laser at 2303 nm for the first time to our knowledge. The Tm^{3+}:YLF laser was end-pumped with a continuous-wave Ti^{3+}:sapphire laser at 780 nm. With 888 mW of pump power, we generated 1-ps pulses at a pulse repetition rate of 17.2 MHz. The resonator was double pumped with an additional retroreflecting mirror (HR near 800 nm) and average output

power of 42 mW could be obtained. The spectral width (full width at half-maximum) was measured as 6.5 nm, giving a time-bandwidth product of 0.389 and indicating that the measured pulses were nearly transform limited. Once mode locking was initiated with the graphene sample, it could be sustained for hours. Compared to KLM operation, graphene mode locking was more stable. We foresee that, since graphene has no bandwidth limitation during mode-locked operation, it is possible to obtain shorter pulse durations in the mid-infrared region with a careful dispersion optimization.

Chapter 7

7 CONCLUSIONS

In this thesis study, graphene was employed as a saturable absorber to generate femtosecond pulses from two different lasers operating in the near- and mid-infrared regions. Kerr-lens mode locked (KLM) operation in the Tm^{3+}:YLF laser was further demonstrated for the first time. Due to the gapless band structure of graphene, it in principle imposes no bandwidth limitation during mode locking. This leads to ultrashort pulse durations only limited by the amplification bandwidth of the gain medium and dispersion management inside the resonator. In the experiments conducted with Cr^{3+}:LiSAF laser in the near-infrared region, graphene was first used to initiate and sustain mode-locked operation. Later, the shortest pulses ever generated from a graphene mode-locked solid-state laser were demonstrated, showing that graphene has no bandwidth limitation during mode locking. The KLM Tm^{3+}:YLF laser was further demonstrated as a new femtosecond laser source operating near 2.3 μm. Later, for the first time to our knowledge, we reported graphene mode-locked Tm^{3+}:YLF laser operating near 2.3 μm with picosecond pulse durations.

In the first and second chapters of this thesis, a brief introduction, resonator design methods, and pulse measurement techniques were described. In the third chapter, graphene was introduced as a saturable absorber to generate femtosecond pulses from a diode-pumped, low-cost, and compact Cr^{3+}:LiSAF laser. Chapter 3 described the experimental results where we generated 68-fs pulses from the graphene mode locked Cr^{3+}:LiSAF laser.

Continuous-wave operation of the Cr^{3+}:LiSAF laser was first investigated by using different output couplers. After the inclusion of graphene, the power performance of the Cr^{3+}:LiSAF laser was also diagnosed. Since graphene introduces nearly 2.3% of loss per round trip, the output power of the laser decreased from 100 mW to 10 mW. Due to saturable absorption characteristics of graphene, output power slightly increased during mode locking to be 11.5 mW. Cavity length was 1.12 m and the corresponding repetition rate was 132 MHz. The optical spectrum and interferometric autocorrelation yielded 12 nm and 68 fs, respectively, and the corresponding time-bandwidth product was estimated to be 0.338, indicating that measured pulses were nearly transform limited. The corresponding peak power and pulse energy were estimated to be 1.26 kW and 86 pJ, respectively. The incident fluence on the graphene saturable absorber was further estimated to be 606 $\mu J/cm^2$. We reported the first demonstration of a mode-locked femtosecond Cr^{3+}:LiSAF laser, initiated with a monolayer graphene saturable absorber. In comparison with the single-walled carbon-nanotube (SWCNT) (another widely used carbon based saturable absorber) mode-locked Cr^{3+}:LiSAF lasers described in Ref. [187], the operation of the graphene mode-locked Cr^{3+}:LiSAF laser described here was more stable, possibly due to the larger modulation depth of the graphene sample. This study demonstrated a low-cost, stable, portable femtosecond Cr^{3+}:LiSAF laser near 850 nm as a source for applications.

To demonstrate that graphene imposes no bandwidth limitation during mode locking, we inserted the graphene sample in a dispersion optimized Cr^{3+}:LiSAF laser. To fine tune the group delay dispersion inside the resonator, a pair of prisms were employed. We have generated, what is to our knowledge, the shortest pulses, directly from a graphene mode-locked solid-state laser. The graphene mode-locked Cr^{3+}:LiSAF gain medium employed in the experiments, was operated in a low-threshold resonator configuration and generated stable, 19-fs pulses near 850 nm with only 275 mW of pump power. Based on the actual recorded spectrum, we estimated the shortest transform limited pulse duration

and time bandwidth product to be 17 fs and 0.41, respectively. The time-bandwidth product of the generated pulses was 0.46, indicating that the measured pulses were slightly chirped. We further investigated the tuning capability of the femtosecond Cr^{3+}:LiSAF laser in Chapter 4. The femtosecond output of the laser could be tuned from 836 nm to 897 nm. We used a definitive experimental test to clearly identify the initiation mechanism for mode locking and experimentally demonstrated that the femtosecond pulse train was initiated solely by the saturable absorber action in graphene.

The second part of the thesis focused on pulse generation experiments from a Tm^{3+} doped YLF laser operating near 2.3 μm. In the initial experiments, we first used a Cr^{2+}:ZnSe saturable absorber to demonstrate passively-Q-switched operation of a Tm^{3+}:YLF laser at 2.3 μm for the first time. After the cw characterization, we placed a Cr^{2+}:ZnSe saturable absorber to obtain Q-switched operation from the Tm^{3+}:YLF laser [132]. The Cr^{2+}:ZnSe saturable absorber had an absorption of 70% at the center wavelength of 1.8 μm and a residual absorption (~3.6% single pass small-signal absorption) around 2.3 μm. Since 2.3 μm transition of the Tm^{3+}:YLF gain medium has lower gain than 2 μm oscillation, it is possible to modulate the intracavity losses even with the residual absorption of the Cr^{2+}:ZnSe saturable absorber. At all pump power levels above lasing threshold, passively-Q-switched operation of the Tm^{3+}:YLF laser could be obtained at 2309 nm with pulse durations and repetition frequencies in the ranges of 1.2–1.4 μs and 0.3–2.1 kHz, respectively. We further determined the round-trip saturable loss of the Cr^{2+}:ZnSe saturable absorber as 3.1% from power dependent repetition rate data. In this study, we introduced a new pulsed source operating near 2.3 μm for the first time. Passively-Q-switched Tm^{3+}:YLF laser near 2.3 μm could be used as a pump source for ZGP optical parametric oscillators to reach longer wavelengths. Since ZGP optical parametric oscillators have an intrinsic loss below 2.1 μm, pulsed 2.3 μm Tm^{3+}:YLF lasers have the potential to become more favorable pump sources.

Chapter 5 presented Kerr-lens mode locked operation of a Tm^{3+}:YLF laser operating at 2.3 μm for the first time to our knowledge. We used a home-built, tunable, and narrow-line Ti^{3+}:sapphire laser as a pump source. With 5-W of green power, the Ti^{3+}:sapphire produced 1W of output power. We first started with the characterization of the x-cavity cw-Tm^{3+}:YLF laser. With nearly 1-W of pump power, we could obtain 100 mW of cw output power at the center wavelength of 2.3 μm. To increase the intracavity energy, we extended the cavity in a q-preserving arrangement, which does not affect the beam parameters inside the resonator. It is challenging to obtain Kerr-lens mode-locking in Tm^{3+}:YLF gain media due to following factors. To overcome the challenge of obtaining KerrLM from tmylf gain medium which has a relatively weak kerr nonlinearity, we included an undoped Znse substrate to provide additional nonlinearity for solitary pulse generation. With 880 mW of pump power at 780 nm, we generated 514-fs pulses at a pulse repetition rate of 41.5 MHz with an average power of 14.4 mW. Based on the measured tuning bandwidth (FWHM=35 nm) of the Tm^{3+}:YLF gain medium in our experiments, it is possible to generate sub-200-fs pulses. We believe that, because of the wide availability of this gain medium as well as the straightforward direct pumping scheme near 800 nm, 2.3-μm mode-locked Tm^{3+}:YLF lasers have the potential to become versatile sources of ultrashort pulses in the mid-IR region.

Finally, in Chapter 6, a monolayer graphene was employed to initiate and sustain mode locked operation in a Tm^{3+}:YLF laser operating near 2.3 μm. To the best of our knowledge, this was the first demonstration of a mode-locked 2.3 μm Tm^{3+}:YLF laser by using graphene as a saturable absorber. Since the inclusion of graphene introduces ~2.3% loss per transit, the Tm^{3+}:YLF gain medium was double pumped by a retroreflecting mirror to utilize the unused pump power. We first started with mode-locking trials in a short x-cavity Tm^{3+}:YLF laser, where mode-locked operation gave pulses with a spectral bandwidth of 2 nm. Since the gain medium introduces an excessive amount of group delay

dispersion (GDD), it was not possible to obtain wider spectrum with the available pump power. To further shorten the pulses, we extended the cavity with a q-preserving configuration up to 8.7 m, leading to an increase in the intracavity energy. At a repetition rate of 17.2 MHz, 1-ps pulses were generated from the graphene mode-locked Tm^{3+}:YLF laser at 2304 nm. The spectral width was measured to be 6.5 nm, resulting in a time-bandwidth product of 0.389. This indicates that the generated pulses were nearly transform limited. The average output power of the generated pulses was 42 mW, giving a pulse energy and peak power of 2.44 nJ and 2.44 kW. A novel approach to lock the number of modes oscillating under the available bandwidth with the graphene saturable absorber would involve the inclusion of a material, providing positive group delay dispersion at 2.3 μm. Another approach is the use of a high-power pump source to obtain femtosecond pulses from the graphene mode-locked Tm^{3+}:YLF gain medium. We foresee that it is possible to obtain shorter pulse widths from the 2.3 μm Tm^{3+}:YLF laser with a careful dispersion management of the resonator.

The primary contributions of this thesis may be listed as follows. We demonstrated graphene mode-locking of a Cr^{3+}:LiSAF laser operating near 850 nm. By using graphene as a saturable absorber, we further generated the shortest pulse durations width from a solid-state laser and performed femtosecond tuning experiments. This study demonstrated that, graphene does not impose any bandwidth limitation during mode locking. We further proposed and experimentally demonstrated a new method to clearly identify the initiation mechanism of mode locking. We demonstrated, for the first time to our knowledge, passively-Q-switched operation from a 2.3 μm Tm^{3+}:YLF laser by using a Cr^{2+}:ZnSe crystal as a saturable absorber. Femtosecond pulses were later generated from a 2.3-μm Tm^{3+}:YLF laser for the first time based on Kerr-lens mode locking. Finally, we achieved graphene mode-locked operation of a Tm^{3+}:YLF laser operating near 2.3 μm for the first

time. The pulsed sources demonstrated in this thesis study have the potential to be used in numerous biomedical sensing and spectroscopy aplications.

BIBLIOGRAPHY

[1] J. C. Diels and W. Rudolph, *Ultrashort Laser Pulse Phenomena: Fundamentals, Techniques, and Applications on a Femtosecond Time Scale*: Academic Press, 2006.

[2] F. K. Tittel, D. Richter, and A. Fried, "Mid-Infrared Laser Applications in Spectroscopy," in *Solid-State Mid-Infrared Laser Sources*, vol. 89, *Springer Topics in Applied Physics*, I. T. Sorokina and K. L. Vodopyanov, Eds. Berlin Heidelberg: Springer, 2003, pp. 445-516.

[3] R. W. Waynant, I. K. Ilev, and I. Gannot, "Mid-infrared laser applications in medicine and biology," *Phil. Trans. R. Soc. Lond. A* **359**, 635-644, (2001).

[4] K. Jain and W. Gorisch, "Repair of small blood vessels with the neodymium-YAG laser: a preliminary report.," *Surgery* **85**, 684-688., (1979).

[5] A. Javan, W. R. Bennett Jr, and D. R. Herriott, "Population inversion and continuous optical maser oscillation in a gas discharge containing a He-Ne mixture," *Physical Review Letters* **6**, 106, (1961).

[6] T. H. Maiman, "Stimulated optical radiation in ruby," *Nature* **187**, 493-494, (1960).

[7] A. Heller, "A High-gain room-temperature liquid laser: Trivalent Neodymium in Selenium Oxychloride," *Applied Physics Letters* **9**, 106-108, (1966).

[8] K. M. Beck, A. G. Joly, and W. P. Hess, "Time-resolved femtosecond laser-induced desorption from magnesium oxide and lithium fluoride single crystals," *Surface Science* **451**, 166-173, (2000).

[9] Y. Shimony, Z. Burshtein, A. B.-A. Baranga, Y. Kalisky, and M. Strauss, "Repetitive q-switching of a CW Nd:YAG laser using Cr^{4+}:YAG saturable absorbers," *IEEE Journal of Quantum Electronics* **32**, 305-310, (1996).

[10] I. Freund, "Self-Q-Switching in Ruby Lasers," *Applied Physics Letters* **12**, 388-&, (1968).

[11] D. Kuizenga and A. Siegman, "FM and AM mode locking of the homogeneous laser - Part II: Experimental results in a Nd:YAG laser with internal FM modulation," *IEEE Journal of Quantum Electronics* **6**, 709-715, (1970).

[12] Z. G. Zhang, K. Torizuka, T. Itatani, K. Kobayashi, T. Sugaya, and T. Nakagawa, "Femtosecond Cr:forsterite laser with mode locking initiated by a quantum-well saturable absorber," *IEEE Journal of Quantum Electronics* **33**, 1975-1981, (1997).

[13] G. Cerullo, S. D. Silvestri, and V. Magni, "Self-starting Kerr-lens mode locking of a Ti:sapphire laser," *Optics Letters* **19**, 1040-1042, (1994).

[14] V. Torres-Company, G. Minguez-Vegal, V. Climent, J. Lancis, and P. Andres, "New photonic devices for ultrafast pulse processing operating on the basis of the

diffraction-dispersion analogy," *Seventh International Workshop on Information Optics* **139**, (2008).

[15] R. H. V. J. Srinivasan, I. Gorczynska, and J. G. Fujimoto, J. Y. Jtang, P. Retsen, and A. E. Cable, "High-speed, high-resolution optical coherence tomographyretinal imaging with a frequency-swept laser at 850 nm," *Optics Letters* **32**, 361-363, (2007).

[16] M. D. Young, S. Backus, C. Durfee, and J. Squier, "Multiphoton imaging with a direct-diode pumped femtosecond Ti:sapphire laser," *Journal of Microscopy* **249**, 83-86, (2013).

[17] R. Huber, M. Wojtkowski, K. Taira, J. G. Fujimoto, and K. Hsu, "Amplified, frequency swept lasers for frequency domain reflectometry and OCT imaging: design and scaling principles," *Optics Express* **13**, 3513-3528, (2005).

[18] T. Udem, R. Holzwarth, and T. W. Hansch, "Optical frequency metrology," *Nature* **416**, 233-237, (2002).

[19] M. Hentschel, R. Kienberger, S. Ch, G. A. Reider, N. Milosevic, T. Brabec, P. Corkum, U. Heinzmann, M. Drescher, and F. Krausz, "Attosecond metrology," *Nature* **414**, 509-513, (2001).

[20] N. Ushakov and M. Georgiyev, "Military Applications of Lasers," FOREIGN TECHNOLOGY DIV WRIGHT-PATTERSON AFB OHIO 1977.

[21] T. Bilici, O. Tabakoglu, H. Kalaycioglu, A. Kurt, A. Sennaroglu, and M. Gulsoy, "Laser Tissue Welding at 1980-nm," presented at 13. National Conference on Biomedical Engineering, (Biomut 2008), Ankara, Turkey, 2008,

[22] B. Ott, B. J. Zuger, D. Erni, A. Banic, T. Schaffner, H. P. Weber, and M. Frenz, "Comparative in vitro study of tissue welding using a 808 nm diode laser and a Ho : YAG laser," *Lasers in Medical Science* **16**, 260-266, (2001).

[23] D. P. Poppas and D. S. Scherr, "Laser tissue welding: a urological surgeon's perspective," *Hemophilia* **4**, 456-462, (1998).

[24] D. E. Spence, Kean, P. N., Sibbett, W., "60-fsec pulse generation from a self-mode-locked Ti:sapphire laser," *Optics Letters* **16**, (1991).

[25] U. Keller, K. J. Weingarten, F. X. Kartner, D. Kopf, B. Braun, I. D. Jung, R. Fluck, C. Hönninger, N. Matuschek, and J. A. d. Au, "Semiconductor saturable absorber mirrors (SESAM's) for femtosecond to nanosecond pulse generation in solid-state lasers," *IEEE Journal of Selected Topics in Quantum Electronics* **2**, 435-453, (1996).

[26] W. B. Cho, J. H. Yim, S. Y. Choi, S. Lee, U. Griebner, V. Petrov, and F. Rotermund, "Mode-locked self-starting Cr:forsterite laser using a single-walled carbon nanotube saturable absorber," *Optics Letters* **33**, 2449-2451, (2008).

[27] W. D. Tan, C. Y. Su, R. J. Knize, G. Q. Xie, L. J. Li, and D. Y. Tang, "Mode locking of ceramic Nd:yttrium aluminum garnet with graphene as a saturable absorber," *Applied Physics Letters* **96**, 031106-3, (2010).

[28] C.-C. Lee, T. R. Schibli, G. Acosta, and J. S. Bunch, "Ultra-short optical pulse generation with single-layer graphene," *Journal of Nonlinear Science* **19**, 767-771, (2010).

[29] Q. Bao, H. Zhang, Y. Wang, Z. Ni, Y. Yan, Z. X. Shen, K. P. Loh, and D. Y. Tang, "Atomic-Layer Graphene as a Saturable Absorber for Ultrafast Pulsed Lasers," *Advanced Functional Materials* **19**, 3077-3083, (2009).

[30] K. S. Novoselov, V. I. Falko, L. Colombo, P. R. Gellert, M. G. Schwab, and K. Kim, "A roadmap for graphene," *Nature* **490**, 192-200, (2012).

[31] A. K. Geim and K. S. Novoselov, "The rise of graphene," *Nature Materials* **6**, 183-191, (2007).

[32] A. Reina, X. T. Jia, J. Ho, D. Nezich, H. B. Son, V. Bulovic, M. S. Dresselhaus, and J. Kong, "Layer Area, Few-Layer Graphene Films on Arbitrary Substrates by Chemical Vapor Deposition," *Nano Letters* **9**, 3087-3087, (2009).

[33] X. Li, W. Cai, J. An, S. Kim, J. Nah, D. Yang, R. Piner, A. Velamakanni, I. Jung, E. Tutuc, S. K. Banerjee, L. Colombo, and R. S. Ruoff, "Large-Area Synthesis of High-Quality and Uniform Graphene Films on Copper Foils," *Science* **324**, 1312-1314, (2009).

[34] F. Canbaz, N. Kakenov, C. Kocabas, U. Demirbas, and A. Sennaroglu, "Graphene mode-locked Cr:LiSAF laser at 850 nm," *Optics Letters* **40**, 4110-4113, (2015).

[35] N. Tolstik, E. Sorokin, and I. T. Sorokina, "Graphene mode-locked Cr:ZnS laser with 41 fs pulse duration," *Optics Express* **22**, 5564-5571, (2014).

[36] I. Baylam, M. N. Cizmeciyan, S. Ozharar, E. O. Polat, C. Kocabas, and A. Sennaroglu, "Femtosecond pulse generation with voltage-controlled graphene saturable absorber," *Optics Letters* **39**, 5180-5183, (2014).

[37] J. Liu, Y. G. Wang, Z. S. Qu, L. H. Zheng, L. B. Su, and J. Xu, "Graphene oxide absorber for 2 μm passive mode-locking Tm:YAlO3 laser," *Laser Physics Letters* **9**, 15-19, (2012).

[38] Y. W. Zhu, S. Murali, M. D. Stoller, K. J. Ganesh, W. W. Cai, P. J. Ferreira, A. Pirkle, R. M. Wallace, K. A. Cychosz, M. Thommes, D. Su, E. A. Stach, and R. S. Ruoff, "Carbon-Based Supercapacitors Produced by Activation of Graphene," *Science* **332**, 1537-1541, (2011).

[39] R. Scheps, J. F. Myers, H. B. Serreze, A. Rosenberg, R. C. Morris, and M. Long, "Diode-pumped Cr:LiSrAlF6 laser," *Optics Letters* **16**, 820-822, (1991).

[40] F. Canbaz, N. Kakenov, C. Kocabas, U. Demirbas, and A. Sennaroglu, "Generation of sub-20-fs pulses from a graphene mode-locked laser," *Optics Express* **25**, 2834-2839, (2017).

[41] D. Sanchez, M. Hemmer, M. Baudisch, S. L. Cousin, K. Zawilski, P. Schunemann, O. Chalus, C. Simon-Boisson, and J. Biegert, "7 μm, ultrafast, sub-millijoule-level mid-infrared optical parametric chirped pulse amplifier pumped at 2 μm," *Optica* **3**, 147-150, (2016).

[42] Z. Chang, A. Rundquist, H. Wang, M. M. Murnane, and H. C. Kapteyn, "Generation of coherent soft X rays at 2.7 nm using high harmonics," *Physical Review Letters* **79**, 2967, (1997).

[43] A. A. Lanin, A. A. Voronin, A. B. Fedotov, and A. M. Zheltikov, "Time-domain spectroscopy in the mid-infrared," *Nature* **4**, 6670, (2014).

[44] J. F. Pinto and L. Esterowitz, "Tm^{3+}:YLF laser continuously tunable between 2.20 and 2.46 mm," *Optics Letters* **19**, 883-885, (1994).

[45] F. Canbaz, I. Yorulmaz, and A. Sennaroglu, "Kerr-lens mode-locked 2.3-μm Tm^{3+}:YLF laser as a source of femtosecond pulses in the mid-infrared," *Optics Letters* **42**, 3964-3967, (2017).

[46] S. T. Lai, "Highly Efficient Emerald Laser," *J Opt Soc Am B* **4**, 1286-1290, (1987).

[47] S. A. Payne, L. L. Chase, H. W. Newkirk, L. K. Smith, and W. F. Krupke, "$LiCaAlF_6:Cr^{3+}$: A Promising New Solid-State Laser Material," *IEEE Journal of Quantum Electronics* **24**, 2243-2252, (1988).

[48] S. A. Payne, L. L. Chase, L. K. Smith, W. L. Kway, and H. W. Newkirk, "Laser performance of $LiSAIF_6:Cr^{3+}$," *Journal of Applied Physics* **66**, 1051-1056, (1989).

[49] L. K. Smith, S. A. Payne, W. L. Kway, L. L. Chase, and B. H. T. Chai, "Investigation of the Laser Properties of Cr3+:LiSrGaF6," *IEEE Journal of Quantum Electronics* **28**, 2612-2618, (1992).

[50] S. T. Lai and M. L. Shand, "High-Efficiency Cw Laser-Pumped Tunable Alexandrite Laser," *Journal of Applied Physics* **54**, 5642-5644, (1983).

[51] L. L. Chase and S. A. Payne, "New tunable solid-state lasers Cr 3+: LiCaAIF 6 and Cr 3+: LiSrAIF 6," *Optics and Photonics News* **1**, 16-19, (1990).

[52] U. Demirbas, M. Schmalz, B. Sumpf, G. Erbert, G. S. Petrich, L. A. Kolodziejski, J. G. Fujimoto, F. X. Kärtner, and A. Leitenstorfer, "Femtosecond Cr:LiSAF and Cr:LiCAF lasers pumped by tapered diode lasers," *Optics Express* **19**, 20444-20461, (2011).

[53] S. Uemura and K. Torizuka, "Generation of 10 fs pulses from a diode-pumped Kerr-lens mode-locked Cr:LiSAF laser," *Japanese Journal of Applied Physisc Part 1-Regular Papers Short Notes & Review Papers* **39**, 3472-3473, (2000).

[54] D. Kopf, K. J. Weingarten, G. Zhang, M. Moser, M. A. Emanuel, R. J. Beach, J. A. Skidmore, and U. Keller, "High-average-power diode-pumped femtosecond Cr:LiSAF lasers," *Applied Physics B-Lasers O* **65**, 235-243, (1997).

[55] B. C. Weber and A. Hirth, "Efficient single-pulse emission with submicrosecond duration from a Cr:LiSAF laser," *Optics Communications* **128**, 158-165, (1996).

[56] J. F. Pinto, L. Esterowitz, and G. H. Rosenblatt, "Frequency tripling of a Q-switched Cr:LiSAF laser to the UV region," *IEEE Journal of Selected Topics in Quantum Electronics* **1**, 58-61, (1995).
[57] P. Beaud, M. Richardson, E. Miesak, and B. Chai, "A Multi-Terawatt Femtosecond Cr-Lisaf Laser," *OSA Proc.* **20**, 242-244, (1994).
[58] P. M. W. French, R. Mellish, J. R. Taylor, P. J. Delfyett, and L. T. Florez, "Mode-locked all-solid-state diode-pumped Cr:LiSAF laser," *Optics Letters* **18**, 1934-1936, (1993).
[59] S. A. Payne, W. F. Krupke, L. K. Smith, W. L. Kway, L. D. Deloach, and J. B. Tassano, "752 Nm Wing-Pumped Cr-Lisaf Laser," *IEEE Journal of Quantum Electronics* **28**, 1188-1196, (1992).
[60] P. F. Moulton, "Spectroscopic and laser characteristics of Ti:Al_2O_3," *Journal of the Optical Society of America B* **3**, 125-133, (1986).
[61] R. J. Jones, K. D. Moll, M. J. Thorpe, and J. Ye, "Phase-Coherent Frequency Combs in the Vacuum Ultraviolet via High-Harmonic Generation inside a Femtosecond Enhancement Cavity," *Physical Review Letters* **94**, 193201, (2005).
[62] X. Zhang, Z. Wang, G. Wang, Y. Zhu, Z. Xu, and C. Chen, "Widely tunable and high-average-power fourth-harmonic generation of a Ti:sapphire laser with a KBe2BO3F2 prism-coupled device," *Optics Letters* **34**, 1342-1344, (2009).
[63] Z. Chang, A. Rundquist, H. Wang, M. M. Murnane, and H. C. Kapteyn, "Generation of Coherent Soft X Rays at 2.7 nm Using High Harmonics," *Physical Review Letters* **79**, 2967-2970, (1997).
[64] J. Zhou, J. Peatross, M. M. Murnane, H. C. Kapteyn, and I. P. Christov, "Enhanced High-Harmonic Generation Using 25 fs Laser Pulses," *Physical Review Letters* **76**, 752-755, (1996).
[65] S. Sawai, A. Hosaka, H. Kawauchi, K. Hirosawa, and F. Kannari, "Demonstration of a Ti:sapphire mode-locked laser pumped directly with a green diode laser," *Applied Physics Express* **7**, (2014).
[66] S. Sawai, A. Hosaka, K. Hirosawa, and F. Kannari, "A Mode-Locked Ti: sapphire Laser Pumped Directly with a Green Diode Laser," *Conf Laser Electr*, (2014).
[67] P. F. Moulton, "An Investigation of the Co:MgF_2 Laser System," *IEEE Journal of Quantum Electronics* **21**, 1582-1595, (1985).
[68] L. J. Atherton, S. A. Payne, and C. D. Brandle, "Oxide and Fluoride Laser Crystals," *Annual Review of Materials Science* **23**, 453-502, (1993).
[69] L. H. Wei, P. K. Kuo, R. L. Thomas, T. R. Anthony, and W. F. Banholzer, "Thermal-Conductivity of Isotopically Modified Single-Crystal Diamond," *Physical Review Letters* **70**, 3764-3767, (1993).

[70] U. Demirbas, D. Li, J. R. Birge, A. Sennaroglu, G. S. Petrich, L. A. Kolodziejski, F. X. Kartner, and J. G. Fujimoto, "Low-cost, single-mode diode-pumped Cr:Colquiriite lasers," *Optics Express* **17**, 14374-14388, (2009).

[71] R. Ell, U. Morgner, F. X. Kärtner, J. G. Fujimoto, E. P. Ippen, V. Scheuer, G. Angelow, and T. Tschudi, "Generation of 5 fs pulses and octave-spanning spectra directly from a Ti:sapphire laser," *Optics Letters* **26**, 373-375, (2001).

[72] M. Stalder, B. H. T. Chai, and M. Bass, "Flashlamp Pumped Cr-LiSrAlF$_6$ Laser," *Applied Physics Letters* **58**, 216-218, (1991).

[73] R. Scheps, J. F. Myers, H. B. Serreze, A. Rosenberg, R. C. Morris, and M. Long, "Diode-Pumped Cr-Lisralf6 Laser," *Optics Letters* **16**, 820-822, (1991).

[74] U. Demirbas, D. Li, J. R. Birge, A. Sennaroglu, G. S. Petrich, L. A. Kolodziejski, F. X. Kärtner, and J. G. Fujimoto, "Low-cost, single-mode diode-pumped Cr:Colquiriite lasers " *Optics Express* **17**, 14374-14388, (2009).

[75] L. DeShazer and K. Kangas, "Extended infrared operation of a titanium sapphire laser," presented at Conference on Lasers and Electro-Optics, 1987, pp. THQ4.

[76] P. C. Wagenblast, U. Morgner, F. Grawert, T. R. Schibli, F. X. Kartner, V. Scheuer, G. Angelow, and M. J. Lederer, "Generation of sub-10-fs pulses from a Kerr-lens mode-locked Cr^{3+}:LiCAF laser oscillator by use of third-order dispersion-compensating double-chirped mirrors," *Optics Letters* **27**, 1726-1728, (2002).

[77] I. T. Sorokina, E. Sorokin, E. Wintner, A. Cassanho, H. P. Jenssen, and R. Szipocs, "14-fs pulse generation in Kerr-lens mode-locked prismless Cr:LiSGaF and Cr:LiSAF lasers: observation of pulse self-frequency shift," *Optics Letters* **22**, 1716-1718, (1997).

[78] E. Sorokin, "Solid-state materials for few-cycle pulse generation and amplification," in *Few-cycle laser pulse generation and its applications*, vol. 95, *Topics in Applied Physics*, F. X. Kartner, Ed. Berlin: Springer-Verlag, 2004, pp. 3-71.

[79] F. Druon, F. Balembois, and P. Georges, "New laser crystals for the generation of ultrashort pulses," *Comptes Rendus Physique* **8**, 153-164, (2007).

[80] L. K. Smith, S. A. Payne, W. L. Kway, L. L. Chase, and B. H. T. Chai, "Investigation of the Laser Properties of Cr^{3+}:LiSrGaF$_6$," *IEEE Journal of Quantum Electronics* **28**, 2612-2618, (1992).

[81] A. Sanchez, R. E. Fahey, A. J. Strauss, and R. L. Aggarwal, "Room-temperature continuous-wave operation of a Ti:Al_2O_3 laser," *Optics Letters* **11**, 363-364, (1986).

[82] M. Stalder, M. Bass, and B. H. T. Chai, "Thermal quenching of fluoresence in chromium-doped fluoride laser crystals," *Journal of Optical Society of America B* **9**, 2271-2273, (1992).

[83] J. M. Eichenholz and M. Richardson, "Measurement of thermal lensing in Cr^{3+}-doped colquiriites," *IEEE Journal of Quantum Electronics* **34**, 910-919, (1998).

[84] F. Balembois, F. Falcoz, F. Kerboull, F. Druon, P. Georges, and A. Brun, "Theoretical and experimental investigations of small-signal gain for a diode-pumped Q-Switched Cr:LiSAF laser," *IEEE Journal of Quantum Electronics* **33**, 269-278, (1997).

[85] F. Balembois, F. Druon, F. Falcoz, P. Georges, and A. Brun, "Performances of Cr:$LiSrAlF_6$ and Cr:$LiSrGaF_6$ for continuous-wave diode-pumped Q-switched operation," *Optics Letters* **22**, 387-389, (1997).

[86] S. Uemura and K. Miyazaki, "Thermal characteristics of a continuous-wave Cr:LiSAF laser," *Japanese Journal of Applied Physisc Part 1-Regular Papers Short Notes & Review Papers* **36**, 4312-4315, (1997).

[87] J. K. Jabczynski, W. Zendzian, Z. Mierczyk, and Z. Frukacz, "Chromium-Doped LiCAF Laser Passively Q Switched with a V^{3+}:YAG Crystal," *Applied Optics* **40**, 6638-6645, (2001).

[88] S. A. Payne, L. K. Smith, R. J. Beach, B. H. T. Chai, J. H. Taasano, L. D. DeLoach, W. L. Kway, R. W. Solarz, and W. F. Krupke, "Properties of Cr:$LiSrAlF_6$ Crystals for laser operation," *Applied Optics* **33**, 5526-5536, (1994).

[89] P. Li-Kam-Wa, B. Chai, and A. Miller, "150-fs Mode-Locked Pulses from Cr^{3+}:$LiSrAlF_6$ and Cr^{3+}:$LiSr_{0.8}Ca_{0.2}AlF_6$," presented at Advanced Solid State Lasers, 1992, pp. SL2.

[90] P. M. W. French, R. Mellish, J. R. Taylor, P. J. Delfyett, and L. T. Florez, "All-Solid-State Diode-Pumped Modelocked Cr-Lisaf Laser," *Electronics Letters* **29**, 1262-1263, (1993).

[91] P. M. W. French, R. Mellish, J. R. Taylor, P. J. Delfyett, and L. T. Florez, "Mode-Locked All-Solid-State Diode-Pumped Cr:LiSAF Laser," *Optics Letters* **18**, 1934-1936, (1993).

[92] F. Balembois, P. Georges, and A. Brun, "Quasi-Continuous-Wave and Actively Mode-Locked Diode-Pumped Cr^{3+}:$LiSrAlF_6$ Laser," *Optics Letters* **18**, 1730-1732, (1993).

[93] G. J. Valentine, J. M. Hopkins, P. Loza-Alvarez, G. T. Kennedy, W. Sibbett, D. Burns, and A. Valster, "Ultralow-pump-threshold, femtosecond Cr^{3+}:$LiSrAlF_6$ laser pumped by a single narrow-stripe AlGaInP laser diode," *Optics Letters* **22**, 1639-41, (1997).

[94] B. Agate, B. Stormont, A. J. Kemp, C. T. A. Brown, U. Keller, and W. Sibbett, "Simplified cavity designs for efficient and compact femtosecond Cr:LiSAF lasers2002.," *Optics Communications* **205**, 207-213, (2002).

[95] S. Tsuda, W. H. Knox, and S. T. Cundiff, "High efficiency diode pumping of a saturable Bragg reflector-mode-locked Cr:LiSAF femtosecond laser," *Applied Physics Letters* **69**, 1538-1540, (1996).

[96] J. M. Hopkins, G. J. Valentine, B. Agate, A. J. Kemp, U. Keller, and W. Sibbett, "Highly compact and efficient femtosecond Cr : LiSAF lasers," *IEEE Journal of Quantum Electronics* **38**, 360-368, (2002).

[97] J. M. Hopkins, G. J. Valentine, W. Sibbett, J. A. der Au, F. Morier-Genoud, U. Keller, and A. Valster, "Efficient, low-noise, SESAM-based femtosecond Cr^{3+}: $LiSrAlF_6$ laser," *Optics Communications* **154**, 54-58, (1998).

[98] R. P. Prasankumar, Y. Hirakawa, A. M. J. Kowalevicz, F. X. Kærtner, J. G. Fujitimo, and W. H. Knox, "An extended cavity femtosecond Cr:LiSAF laser pumped by low cost diode lasers," *Optics Express* **11**, 1265-1269, (2003).

[99] D. Li, U. Demirbas, J. R. Birge, G. S. Petrich, L. A. Kolodziejski, A. Sennaroglu, F. X. Kartner, and J. G. Fujimoto, "Diode-pumped passively mode-locked GHz femtosecond Cr:LiSAF laser with kW peak power," *Optics Letters* **35**, 1446-8, (2010).

[100] S. Uemura and K. Torizuka, "Generation of 12-fs pulses from a diode-pumped Kerr-lens mode-locked Cr : LiSAF laser," *Optics Letters* **24**, 780-782, (1999).

[101] A. J. Kemp, B. Stormont, B. Agate, C. T. A. Brown, U. Keller, and W. Sibbett, "Gigahertz repetition-rate from directly diode-pumped femtosecond Cr:LiSAF laser," *Electronics Letters* **37**, 1457-1458, (2001).

[102] U. Demirbas, J. Wang, G. S. Petrich, S. Nabanja, J. R. Birge, L. A. Kolodziejski, F. X. Kartner, and J. G. Fujimoto, "100-nm tunable femtosecond Cr:LiSAF laser mode locked with a broadband saturable Bragg reflector," *Applied Optics* **56**, 3812-3816, (2017).

[103] U. Demirbas, K. H. Hong, J. G. Fujimoto, A. Sennaroglu, and F. X. Kartner, "Low-cost cavity-dumped femtosecond Cr:LiSAF laser producing > 100 nJ pulses," *Optics Letters* **35**, 607-609, (2010).

[104] U. Demirbas, K. H. Hong, J. G. Fujimoto, A. Sennaroglu, and F. X. Kartner, "Generation of Sub-150-fs, 100 nJ Pulses from a Low-cost Cavity-dumped Cr:LiSAF Laser," *2010 Conference on Lasers and Electro-Optics (Cleo) and Quantum Electronics and Laser Science Conference (Qels)*, (2010).

[105] C. Cihan, E. Beyatli, F. Canbaz, L. J. Chen, B. Sumpf, G. Erbert, A. Leitenstorfer, F. X. Kartner, A. Sennaroglu, and U. Demirbas, "Gain-Matched Output Couplers for Efficient Kerr-Lens Mode-Locking of Low-Cost and High-Peak Power Cr:LiSAF Lasers," *IEEE Journal of Selected Topics in Quantum Electronics* **21**, (2015).

[106] F. Canbaz, E. Beyatli, L. J. Chen, A. Sennaroglu, F. X. Kartner, and U. Demirbas, "Highly efficient and robust operation of Kerr-lens mode-locked Cr:LiSAF lasers using gain-matched output couplers," *Optics Letters* **39**, 327-330, (2014).

[107] R. C. Stoneman and L. Esterowitz, "Efficient, broadly tunable, laser-pumped Tm:YAG and Tm:YSGG cw lasers," *Optics Letters* **15**, 486-488, (1990).

[108] V. Sudesh and J. A. Piper, "Spectroscopy, Modeling, and Laser Operation of Thulium Crystals at 2.3 μm," *IEEE Journal of Quantum Electronics* **QE-36**, 879-884, (2000).
[109] R. C. Stoneman and L. Esterowitz, "Efficient 1.94-μm Tm:YALO Laser," *IEEE Journal of Selected Topics in Quantum Electronics* **1**, 78-81, (1995).
[110] A. Dergachev, K. Wall, and P. F. Moulton, "A CW Side-Pumped Tm:YLF Laser," presented at OSA TOPS Advanced Solid State Lasers, 2002, pp. 343-346.
[111] J. F. Pinto, G. H. Rosenblatt, and L. Esterowitz, "Tm^{3+}: YLF laser continuously tunable between 2.20 and 2.46 μm," *Optics Letters* **19**, 883-885, (1994).
[112] M. G. Jani, N. P. Barnes, C. B. Murray, D. W. Hart, G. J. Quarles, and V. K. Castillo, "Diode-pumped Ho:Tm:$LuLiF_4$ laser at room temperature," *IEEE Journal of Quantum Electronics* **33**, 112-115, (1997).
[113] L. Fornasiero, N. Berner, B. M. Dicks, E. Mix, V. Peters, K. Petermann, and G. Huber, "Broadly tunable laser emission from Tm:Y_2O_3 and Tm:Sc_2O_3 at 2 μm," *Advanced Solid-State Lasers* **26**, 450-453, (1999).
[114] N. Coluccelli, D. Gatti, G. Galzerano, F. Cornacchia, D. Parisi, A. Toncelli, M. Tonelli, and P. Laporta, "Tunability range of 245 nm in a diode-pumped Tm : BaY2F8 laser at 1.9 mu m: a theoretical and experimental investigation," *Applied Physics B-Lasers O* **85**, 553-555, (2006).
[115] O. L. Antipov, A. A. Novikov, N. G. Zakharov, A. P. Zinoviev, H. Yagi, N. V. Sakharov, M. V. Kruglova, M. O. Marychev, O. N. Gorshkov, and A. A. Lagatskii, "Efficient 2.1-mu m lasers based on Tm^{3+}:Lu_2O_3 ceramics pumped by 800-nm laser diodes," *Physica Status Solidi C: Current Topics in Solid State Physics, Vol 10, No 6* **10**, 969-973, (2013).
[116] F. Fusari, A. A. Lagatsky, G. Jose, S. Calvez, A. Jha, M. D. Dawson, J. A. Gupta, W. Sibbett, and C. T. A. Brown, "Femtosecond mode-locked Tm^{3+} and Tm^{3+}-Ho^{3+} doped 2 μm glass lasers," *Optics Express* **18**, 22090-22098, (2010).
[117] C. E. Aleshire, X. Y. Charles, P. A. Reed, and T. Y. Fan, "Efficient cryogenic near-infrared Tm: YLF laser," *Optics Express* **25**, 13408-13413, (2017).
[118] A. A. Lagatsky, P. Koopmann, P. Fuhrberg, G. Huber, C. T. A. Brown, and W. Sibbett, "Passively mode locked femtosecond Tm:Sc_2O_3 laser at 2.1 μm," *Optics Letters* **37**, 437-439, (2012).
[119] A. A. Lagatsky, O. L. Antipov, and W. Sibbett, "Broadly tunable femtosecond Tm:Lu_2O_3 ceramic laser operating around 2070 nm," *Optics Express* **20**, 19349-19354, (2012).
[120] A. Schmidt, P. Koopmann, G. Huber, P. Fuhrberg, S. Y. Choi, D.-I. Yeom, F. Rotermund, V. Petrov, and U. Griebner, "175 fs Tm:Lu_2O_3 laser at 2.07 μm mode-locked using single-walled carbon nanotubes," *Optics Express* **20**, 5313-5318, (2012).

[121] E. Passacantilli, G. Anichini, G. Lapadula, M. Salvati, J. Lenzi, and A. Santoro, "Assessment of the utility of the 2-micro thulium laser in surgical removal of intracranial meningiomas," *Lasers Surg Med* **45**, 148-54, (2013).

[122] T. Bilici, H. O. Tabakoglu, N. Topaloglu, H. Kalaycioglu, A. Kurt, A. Sennaroglu, and M. Gulsoy, "Modulated and continuous-wave operations of low-power thulium (Tm:YAP) laser in tissue welding," *Journal of Biomedical Optics* **15**, 038001, (2010).

[123] R. Rasier, M. Ozeren, O. Artunay, H. Bahcecioglu, I. Seckin, H. Kalaycioglu, A. Kurt, A. Sennaroglu, and M. Gulsoy, "Corneal Tissue Welding With Infrared Laser Irradiation After Clear Corneal Incision," *Cornea* **29**, 985-990, (2010).

[124] T. M. Taczak and D. K. Killinger, "Development of a tunable, narrow-linewidth, cw 2.066-mu m Ho:YLF laser for remote sensing of atmospheric CO_2 and H_2O," *Applied Optics* **37**, 8460-8476, (1998).

[125] R. Targ, B. C. Steakley, J. G. Hawley, L. L. Ames, P. Forney, D. Swanson, R. Stone, R. G. Otto, V. Zarifis, P. Brockman, R. S. Calloway, S. H. Klein, and P. A. Robinson, "Coherent lidar airborne wind sensor II: flight-test results at 2 and 10 vm," *Applied Optics* **35**, 7117-7127, (1996).

[126] F. Fusari, S. Vetter, A. A. Lagatsky, B. Richards, S. Calvez, A. Jha, M. D. Dawson, W. Sibbett, and C. T. A. Brown, "Tunable laser operation of a Tm^{3+}-doped tellurite glass laser near 2 μm pumped by a 1211 nm semiconductor disk laser," *Optical Materials* **32**, 1007-1010, (2010).

[127] L. Hobrock, L. DeShazer, W. Krupke, G. Keig, and D. Witter, "Four-level operation of Tm: Cr:$YAlO_3$ laser at 2.35 μm," *IEEE Journal of Quantum Electronics* **8**, 533-534, (1972).

[128] J. Caird, L. DeShazer, and J. Nella, "Characteristics of room-temperature 2.3-μm laser emission from Tm^{3+} in YAG and $YAlO_3$," *IEEE Journal of Quantum Electronics* **11**, 874-881, (1975).

[129] L. Esterowitz, R. Allen, and I. Aggarwal, "Pulsed laser emission at 2.3 mu m in a thulium-doped fluorozirconate fibre," *Electronics Letters* **24**, 1104, (1988).

[130] A. Diening, P.-A. Möbert, and G. Huber, "Diode-pumped continuous-wave, quasi-continuous-wave, and Q-switched laser operation of Yb^{3+}, Tm^{3+}: $YLiF_4$ at 1.5 and 2.3 μm," *Journal of Applied Physics* **84**, 5900-5904, (1998).

[131] P. S. F. De Matos, N. U. Wetter, L. Gomes, I. M. Ranieri, and S. L. Baldochi, "A high power 2.3 μm Yb:Tm:YLF laser diode-pumped simultaneously at 685 and 960 nm," *Journal of Optics A-Pure Applied Optics* **10**, (2008).

[132] F. Canbaz, I. Yorulmaz, and A. Sennaroglu, "2.3-μm Tm^{3+}:YLF laser passively Q-switched with a Cr^{2+}:ZnSe saturable absorber," *Optics Letters* **42**, 1656-1659, (2017).

[133] R. Soulard, A. Tyazhev, J.-L. Doualan, A. Braud, A. Hideur, M. Laroche, B. Xu, and P. Camy, "2.3 μm Tm^{3+}:YLF mode-locked laser," *Optics Letters* **42**, 3534-3536, (2017).
[134] I. Yorulmaz and A. Sennaroglu, "Low-Threshold Diode-Pumped 2.3-μm Tm^{3+}: YLF Lasers," *IEEE Journal of Selected Topics in Quantum Electronics* **24**, (2018).
[135] K. S. Novoselov, A. K. Geim, S. V. Morozov, D. Jiang, Y. Zhang, S. V. Dubonos, I. V. Grigorieva, and A. A. Firsov, "Electric Field Effect in Atomically Thin Carbon Films," *Science* **306**, 666-669, (2004).
[136] I. Baylam, S. Ozharar, N. Kakenov, C. Kocabas, and A. Sennaroglu, "Femtosecond pulse generation from a Ti^{3+}:sapphire laser near 800 nm with voltage reconfigurable graphene saturable absorbers," *Optics Letters* **42**, 1404-1407, (2017).
[137] G. Le Lay, E. Salomon, P. De Padova, J. M. Layet, and T. Angot, "The Rise of Elemental Two-Dimensional Materials Beyond Graphene," *Australian Journal of Chemistry* **67**, 1370-1372, (2014).
[138] J. J. Yoo, K. Balakrishnan, J. S. Huang, V. Meunier, B. G. Sumpter, A. Srivastava, M. Conway, A. L. M. Reddy, J. Yu, R. Vajtai, and P. M. Ajayan, "Ultrathin Planar Graphene Supercapacitors," *Nano Letters* **11**, 1423-1427, (2011).
[139] H. T. Liu, Y. Q. Liu, and D. B. Zhu, "Chemical doping of graphene," *Journal of Materials Chemistry* **21**, 3335-3345, (2011).
[140] J. Yan, Y. B. Zhang, P. Kim, and A. Pinczuk, "Electric field effect tuning of electron-phonon coupling in graphene," *Physical Review Letters* **98**, (2007).
[141] A. H. Castro Neto, F. Guinea, N. M. R. Peres, K. S. Novoselov, and A. K. Geim, "The electronic properties of graphene," *Reviews of Modern Physics* **81**, 109-162, (2009).
[142] A. B. Kuzmenko, E. van Heumen, F. Carbone, and D. van der Marel, "Universal Optical Conductance of Graphite," *Physical Review Letters* **100**, 117401, (2008).
[143] C. Lee, X. D. Wei, J. W. Kysar, and J. Hone, "Measurement of the elastic properties and intrinsic strength of monolayer graphene," *Science* **321**, 385-388, (2008).
[144] J. Ma, H. T. Huang, K. J. Ning, X. D. Xu, G. Q. Xie, L. J. Qian, K. P. Loh, and D. Y. Tang, "Generation of 30 fs pulses from a diode-pumped graphene mode-locked Yb:CaYAlO4 laser," *Optics Letters* **41**, 890-893, (2016).
[145] I. Baylam, O. Balci, N. Kakenov, C. Kocabas, and A. Sennaroglu, "Graphene-gold supercapacitor as a voltage controlled saturable absorber for femtosecond pulse generation," *Optics Letters* **41**, 910-913, (2016).
[146] I. Baylam, M. N. Cizmeciyan, S. Ozharar, E. O. Polat, C. Kocabas, and A. Sennaroglu, "Graphene Supercapacitor as a Voltage Controlled Saturable Absorber for Femtosecond Pulse Generation," *2014 Conference on Lasers and Electro-Optics (Cleo)*, (2014).

[147] S. Ozharar, I. Baylam, M. N. Cizmeciyan, O. Balci, E. Pince, C. Kocabas, and A. Sennaroglu, "Graphene mode-locked multipass-cavity femtosecond Cr^{4+}: forsterite laser," *Journal of Optical Society of America B* **30**, 1270-1275, (2013).
[148] M. N. Cizmeciyan, J. W. Kim, S. Bae, B. H. Hong, F. Rotermund, and A. Sennaroglu, "Graphene mode-locked femtosecond Cr:ZnSe laser at 2500 nm," *Optics Letters* **38**, 341-343, (2013).
[149] R. R. Nair, P. Blake, A. N. Grigorenko, K. S. Novoselov, T. J. Booth, T. Stauber, N. M. R. Peres, and A. K. Geim, "Fine structure constant defines visual transparency of graphene," *Science* **320**, 1308-1308, (2008).
[150] A. C. Ferrari and D. M. Basko, "Raman spectroscopy as a versatile tool for studying the properties of graphene," *Nature Nanotechnology* **8**, 235-246, (2013).
[151] A. C. Ferrari, J. C. Meyer, V. Scardaci, C. Casiraghi, M. Lazzeri, F. Mauri, S. Piscanec, D. Jiang, K. S. Novoselov, S. Roth, and A. K. Geim, "Raman Spectrum of Graphene and Graphene Layers," *Physical Review Letters* **97**, 187401, (2006).
[152] A. Reina, X. Jia, J. Ho, D. Nezich, H. Son, V. Bulovic, M. S. Dresselhaus, and J. Kong, "Large Area, Few-Layer Graphene Films on Arbitrary Substrates by Chemical Vapor Deposition," *Nano Letters* **9**, 30-35, (2008).
[153] A. Reina, X. T. Jia, J. Ho, D. Nezich, H. B. Son, V. Bulovic, M. S. Dresselhaus, and J. Kong, "Large Area, Few-Layer Graphene Films on Arbitrary Substrates by Chemical Vapor Deposition," *Nano Letters* **9**, 30-35, (2009).
[154] J. Maultzsch, S. Reich, and C. Thomsen, "Double-resonant Raman scattering in graphite: Interference effects, selection rules, and phonon dispersion," *Physical Review B* **70**, (2004).
[155] S. Kumar, M. Anija, N. Kamaraju, K. S. Vasu, K. S. Subrahmanyam, A. K. Sood, and C. N. R. Rao, "Femtosecond carrier dynamics and saturable absorption in graphene suspensions," *Applied Physics Letters* **95**, (2009).
[156] J. M. Dawlaty, S. Shivaraman, M. Chandrashekhar, F. Rana, and M. G. Spencer, "Measurement of ultrafast carrier dynamics in epitaxial graphene," *Applied Physics Letters* **92**, 042116, (2008).
[157] A. Sennaroglu, U. Demirbas, S. Ozharar, and F. Yaman, "Accurate determination of saturation parameters for Cr^{4+}-doped solid-state saturable absorbers," *Journal of Optical Society of America B* **23**, 241-249, (2006).
[158] A. K. Geim and A. H. MacDonald, "Graphene: Exploring carbon flatland," *Physics Today* **60**, 35-41, (2007).
[159] B. Jayasena and S. Subbiah, "A novel mechanical cleavage method for synthesizing few-layer graphenes," *Nanoscale Research Letters* **6**, (2011).
[160] B. Jayasena, C. D. Reddy, and S. Subbiah, "Separation, folding and shearing of graphene layers during wedge-based mechanical exfoliation," *Nanotechnology* **24**, (2013).

[161] P. Sutter, "EPITAXIAL GRAPHENE How silicon leaves the scene," *Nature Materials* **8**, 171-172, (2009).
[162] S. Bae, H. Kim, Y. Lee, X. F. Xu, J. S. Park, Y. Zheng, J. Balakrishnan, T. Lei, H. R. Kim, Y. I. Song, Y. J. Kim, K. S. Kim, B. Ozyilmaz, J. H. Ahn, B. H. Hong, and S. Iijima, "Roll-to-roll production of 30-inch graphene films for transparent electrodes," *Nature Nanotechnology* **5**, 574-578, (2010).
[163] X. S. Li, W. W. Cai, J. H. An, S. Kim, J. Nah, D. X. Yang, R. Piner, A. Velamakanni, I. Jung, E. Tutuc, S. K. Banerjee, L. Colombo, and R. S. Ruoff, "Large-Area Synthesis of High-Quality and Uniform Graphene Films on Copper Foils," *Science* **324**, 1312-1314, (2009).
[164] E. O. Polat, O. Balci, N. Kakenov, H. B. Uzlu, C. Kocabas, and R. Dahiya, "Synthesis of Large Area Graphene for High Performance in Flexible Optoelectronic Devices," *Sci Rep-Uk* **5**, (2015).
[165] T. Oznuluer, E. Pince, E. O. Polat, O. Balci, O. Salihoglu, and C. Kocabas, "Synthesis of graphene on gold," *Applied Physics Letters* **98**, (2011).
[166] Q. B. Zheng, W. H. Ip, X. Y. Lin, N. Yousefi, K. K. Yeung, Z. G. Li, and J. K. Kim, "Transparent Conductive Films Consisting of Ultra large Graphene Sheets Produced by Langmuir-Blodgett Assembly," *Acs Nano* **5**, 6039-6051, (2011).
[167] A. Chakrabarti, J. Lu, J. C. Skrabutenas, T. Xu, Z. L. Xiao, J. A. Maguire, and N. S. Hosmane, "Conversion of carbon dioxide to few-layer graphene," *Journal of Material Chemistry* **21**, 9491-9493, (2011).
[168] N. I. Kovtyukhova, Y. X. Wang, A. Berkdemir, R. Cruz-Silva, M. Terrones, V. H. Crespi, and T. E. Mallouk, "Non-oxidative intercalation and exfoliation of graphite by Bronsted acids," *Nature Chemistry* **6**, 957-963, (2014).
[169] A. Sennaroglu, *Photonics and laser engineering : principles, devices, and applications*. New York: McGraw-Hill, 2010.
[170] L. E. Hargrove, R. L. Fork, and M. A. Pollack, "Locking of HeXe5F8;Ne laser modes induced by syncronous intracavity modulation," *Applied Physics Letters* **5**, 4-5, (1964).
[171] H. A. Haus, "Mode-locking of lasers," *IEEE Journal of Selected Topics in Quantum Electronis* **6**, 1173-1185, (2000).
[172] M. Maier, W. Kaiser, and J. A. Giordmaine, "Intense Light Bursts in the Stimulated Raman Effect," *Physical Review Letters* **17**, 1275-1277, (1966).
[173] J. Armstrong, "Measurement of picosecond laser pulse widths," *Applied Physics Letters* **10**, 16-18, (1967).
[174] J. C. M. Diels, J. J. Fontaine, I. C. Mcmichael, and F. Simoni, "Control and Measurement of Ultrashort Pulse Shapes (in Amplitude and Phase) with Femtosecond Accuracy," *Applied Optics* **24**, 1270-1282, (1985).

[175] D. Findlay and R. A. Clay, "The measurement of internal losses in 4-level lasers," *Physics Letters* **20**, 277-278, (1966).
[176] A. Muti, A. Kocabas, and A. Sennaroglu, "Generation of 4-nJ Pulses from a Diode-Pumped Femtosecond Ti3+:sapphire Laser," presented at Laser Congress 2017 (ASSL, LAC), Nagoya, Aichi, 2017, pp. ATu1A.5.
[177] C. Bondoux and C. Cornaggia, "Few-cycle laser pulses tested with double ionization of H-2," *Journal of Physics B-Atomic Molecular and Optical Physics* **40**, 4463-4470, (2007).
[178] A. Sennaroglu and J. G. Fujimoto, "Design criteria for Herriott-type multi-pass cavities for ultrashort pulse lasers," *Optics Express* **11**, 1106-1113, (2003).
[179] D. Milam, M. J. Weber, and A. Glass, "Nonlinear refractive index of fluoride crystals," *Applied Physics Letters* **31**, 822-825, (1977).
[180] M. N. Cizmeciyan, H. Cankaya, A. Kurt, and A. Sennaroglu, "Kerr-lens mode-locked femtosecond Cr^{2+}:ZnSe laser at 2420 nm," *Optics Letters* **34**, 3056-3058, (2009).
[181] M. N. Cizmeciyan, H. Cankaya, A. Kurt, and A. Sennaroglu, "Operation of femtosecond Kerr-lens mode-locked Cr:ZnSe lasers with different dispersion compensation methods," *Applied Physics B-Lasers O* **106**, 887-892, (2012).
[182] B. Tatian, "Fitting refractive-index data with the Sellmeier dispersion formula," *Appl. Opt.* **23**, 4477-4485, (1984).
[183] N. P. Barnes and D. J. Gettemy, "Temperature variation of the refractive indices of yttrium lithium fluoride," *Journal of Optical Society of America* **70**, 1244-1247, (1980).
[184] D. E. Zelmon, D. L. Small, and R. Page, "Refractive-index measurements of undoped yttrium aluminum garnet from 0.4 to 5.0 μm," *Applied Optics* **37**, 4933-4935, (1998).
[185] P. E. Ciddor, "Refractive index of air: New equations for the visible and near infrared," *Applied Optics* **35**, 1566-1573, (1996).
[186] D. Milam, "Review and assessment of measured values of the nonlinear refractive-index coefficient of fused silica," *Applied Optics* **37**, 546-550, (1998).
[187] A. Agnesi, F. Pirzio, E. Ugolotti, S. Y. Choi, D. I. Yeom, and F. Rotermund, "Femtosecond single-mode diode-pumped Cr:LiSAF laser mode-locked with single-walled carbon nanotubes," *Optics Communications* **285**, 742-745, (2012).

VITA

Ferda Canbaz was born in Kırklareli on June 2, 1988. She received her BS degree in Engineering Physics from Istanbul Technical University in 2011 and Master of Science degree program in Optoelectronics and Photonics Engineering Program from Koc University in 2013. Since Fall 2013 she has been pursuing her doctoral studies in the Physics department at Koç University. Her research interests include femtosecond lasers, solid-state lasers in the near- and mid-infrared region, biomedical applications of lasers, laser processing, and nonlinear optics.

Publications:

- I. Baylam, F. Canbaz, and A. Sennaroglu, "Dual-Wavelength Temporal Dynamics of a Gain-Switched 2-µm Tm^{3+}:Lu_2O_3 Ceramic Laser," IEEE J. Sel. Top. Quant. 24, (2018).
- F. Canbaz, I. Yorulmaz, and A. Sennaroglu, "Kerr-lens mode-locked 2.3 µm Tm^{3+}:YLF laser as a source of femtosecond pulses," Opt. Lett., 42 (19), 3964-3967 (2017).
- F. Canbaz, I. Yorulmaz, and A. Sennaroglu, "2.3-µm Tm^{3+}:YLF laser passively Q-switched with a Cr^{2+}:ZnSe saturable absorber," Opt. Lett., 42 (9), 3964-3967 (2017).
- F. Canbaz, N. Kakenov, C. Kocabas, U. Demirbas, and A. Sennaroglu, "Generation of sub-20-fs pulses from a graphene mode-locked laser," Opt. Express, 25 (3), 4110-4113 (2015).
- F. Canbaz, N. Kakenov, C. Kocabas, U. Demirbas, and A. Sennaroglu, "Graphene mode-locked Cr:LiSAF laser at 850 nm," Opt. Lett., 40 (17), 4110-4113 (2015).
- C. Cihan, E. Beyatli, F. Canbaz, L-J. Chen, B. Sumpf, G. Erbert, A. Leitenstorfer, F. X. Kärtner, A. Sennaroglu, and U. Demirbas, "Gain-Matched output couplers for efficient Kerr-lens mode-locking of low-cost and high peak-power Cr:LiSAF Lasers," IEEE J. Selected Topics in Quantum Electron., 21, 1100712 (2015).

- F. Canbaz, E. Beyatli, L-J. Chen, A. Sennaroğlu, F. X. Kärtner, and U. Demirbas, "Highly efficient and robust operation of Kerr-lens mode-locked Cr:LiSAF lasers using gain-matched output couplers," Opt. Lett., 39 (2), 327-330 (2014).
- A. K. Turkoglu, T. Ersoy, F. Canbaz, and S. Akturk, "Effects of waveguide behavior during femtosecond-laser drilling of metals," Appl. Phys. A, 108 (4), 935-941 (2012).

Proceedings:

- F. Canbaz, I. Yorulmaz, J. E. Bae, S. Y. Choi, F. Rotermund, and A. Sennaroglu, "Kerr-lens mode-locked and graphene mode-locked operations of a 2.3-μm Tm^{3+}:YLF laser," 2018 Advanced Solid-State Lasers Congress, Boston, Massachusetts, United States, November 4-8, 2018, (Optical Society of America, Washington, D.C., 2018), oral presentation (to be presented).
- F. Canbaz, I. Yorulmaz, and A. Sennaroglu, "Passive Q-switching of a Tm^{3+}:YLF laser at 2.3 μm with a Cr^{2+}:ZnSe saturable absorber," 2017 Advanced Solid-State Lasers Congress, Nagoya, Japan, October 1-5, 2017, (Optical Society of America, Washington, D.C., 2017), paper JM5A.18, poster presentation.
- F. Canbaz, N. Kakenov, C. Kocabas, U. Demirbas, and A. Sennaroglu, "Sub-20 femtosecond pulse generation with a graphene mode-locked solid-state laser," 2016 Advanced Solid-State Lasers Congress, Boston, Massachusetts, United States, October 30-November 3, 2016, (Optical Society of America, Washington, D.C., 2016), paper ATu1A.2, oral presentation.
- F. Canbaz, N. Kakenov, C. Kocabas, U. Demirbas, and A. Sennaroglu, "Graphene mode-locked femtosecond Cr:LiSAF laser," 2015 Advanced Solid-State Lasers Congress, Berlin, Germany, October 4-9, 2015, (Optical Society of America, Washington, D.C., 2015), paper AM5A.24, poster presentation.
- F. Canbaz, N. Kakenov, C. Kocabas, U. Demirbas, and A. Sennaroglu, "Graphene mode-locked diode-pumped Cr:LiSAF laser at 857 nm," CLEO/Europe-EQEC Conference, June 21-25, 2015, International Congress Center, Munich, Germany, paper CA-12.4 THU, oral presentation.
- C. Cihan, E. Beyatli, F. Canbaz, L-J Chen, B. Sumpf, G. Erbert, A. Leitenstorfer, F. Kärtner, A. Sennaroglu, and U. Demirbas, "Gain-Matched

Output Couplers (GMOCs) for Efficient and Robust Kerr-Lens Mode-Locking of Cr:LiSAF lasers," CLEO 2014 Conference on Lasers and Electro-Optics, June 8-13, 2014, San Jose, CA, USA, paper STu2E.8, oral presentation.

- F. Canbaz, E. Beyatli, L-J Chen, A. Sennaroglu, F. X. Kärtner, and U. Demirbas, "Efficient and Robust Kerr-Lens Mode-Locking of Cr:LiSAF Lasers Using Gain-Matched Output Couplers," 2013 Advanced Solid-State Lasers Congress, Paris, France, October 27-November 1, 2013 (Optical Society of America, Washington, D.C., 2013), paper ATh3A.4, oral presentation.
- N. Mustafaoglu, G. Acar, B. Ozen, F. Canbaz, and G. A. Evingur, "Diffusion modelling of photo-curing depth for collagen cross-linking on Cornea," 8th International Conference on Nanosciences & Nanotechnologies, July 12-15, 2011, Thessaloniki, Greece, poster presentation.

Awards:

2017:	Fotonik 2017 Best Poster Competition (2nd place)
2016:	Fotonik 2016 Best Poster Competition (2nd place)
2011:	3rd Ranking student in Engineering Physics Graduating Class of 2011, Istanbul Technical University